ON THE GEOGRAPHIC VARIABILITY OF OCEANIC MESOSCALE MOTIONS

by

KEITH ALEC THOMSON
B.Sc., Royal Roads Military College, 1977

A THESIS SUBMITTED IN PARTIAL FULFILMENT OF
THE REQUIREMENTS FOR THE DEGREE OF
DOCTOR OF PHILOSOPHY

in

THE FACULTY OF GRADUATE STUDIES

Oceanography Department

We accept this thesis as conforming
to the required standard

THE UNIVERSITY OF BRITISH COLUMBIA
June 1986

In presenting this thesis in partial fulfilment of the requirements for an advanced degree at the University of British Columbia, I agree that the Library shall make it freely available for reference and study. I further agree that permission for extensive copying of this thesis for scholarly purposes may be granted by the Head of my Department or by his or her representatives. It is understood that copying or publication of this thesis for financial gain shall not be allowed without my written permission.

Department of Oceanography

The University of British Columbia
6270 University Boulevard
Vancouver, B.C. Canada
V6T 1W5

Date: June 26, 1986

ABSTRACT

Quasi-synoptic expendable bathythermograph data were acquired, from the Canadian Armed Forces, the United States Navy and the United States National Oceanographic Data Center, for the Pacific and Atlantic Oceans. On the basis of these data and the results of previous studies using climatological data, six geographic regions were defined: the high-energy regions of the Northwest Atlantic and Northwest Pacific, and the low-energy regions of the Northeast Atlantic, Northeast Pacific, South Atlantic and South Pacific. Spatial series of two variables, representative of the upper layer (400 m) mesoscale variability, were obtained for each section - the mid- thermocline temperature and the geopotential anomaly (0 - 4000 kPa).

The central moments and the wavenumber spectra of each variable were estimated for the six geographic regions, the combined high-energy areas and the combined low-energy areas. In the high-energy regions and the Northeast Atlantic, it was found that the temperature between 350 and 400 m is representative of the temperature variability due to the baroclinic eddy field, whereas, the temperature between 150 and 200 m is more representative of the eddy variability in most of the low-energy regions. The standard deviations of temperature, in the high- and low-energy regions, are 1.40 and 0.54°C, respectively. The standard deviations of the geopotential anomaly are 0.67 and 0.26 m^2/s^2, respectively. The high-energy regions have dominant spectral wavelengths in the geopotential anomaly fields of 300 and 155 km, with corresponding baroclinic surface velocity scales of 9.6 and 17.5 cm/s. The low-energy regions have dominant wavelengths of 300 and 170 km with velocity scales of 4.5 and 5.5 cm/s, respectively. In general, the high-energy regions have a greater portion of their spectral variance concentrated in the higher wavenumbers (i.e. 280 to 100 km wavelengths), than the low-energy regions. The eddy kinetic energies per unit mass for the high- and low-energy regions were estimated at 250 and 36 cm^2/s^2, respectively.

The geographic variability of the governing dynamics was inferred by evaluating the quasigeostrophic scaling parameters (i.e. the Rossby number (Ro), the Burger number (B) and the sphericity parameter (β^*)) and the Rossby wave steepness parameter (M). Also, the properties of free linear dispersive Rossby waves were calculated with the observed wavelengths and the spectral power-laws of the temperature spectra were compared with several models of

nonlinear geophysical turbulence. It was found that $Ro<<1$, $B = 0(1)$ and $\beta^*<<1$, which is consistent with the scaling for quasigeostrophy. The dynamics inferred from these analyses exhibit a distinct geographic variability. Motions with wavelengths greater than 200 km in all regions are consistent with linear/nonlinear Rossby wave theory. Mesoscale perturbations in the high-energy regions are, of course, more nonlinear than the corresponding length scales in the low-energy regions. Motions, with wavelengths less than 200 km in the high-energy regions, are consistent with quasigeostrophic turbulence theory, more specifically, with Charney's (1971) model of three-dimensional quasigeostrophic turbulence. Motions with wavelengths less than 200 km in the low-energy regions have dynamics that are intermediate between linear/nonlinear Rossby wave theory, and quasigeostrophic turbulence theory.

TABLE OF CONTENTS

LIST OF SYMBOLS

A_s	anisotropy factor
B	Burger number
C_g	group velocity
C_p	phase velocity
D	geopotential anomaly perturbation, 0 - 4000 kPa
E	wavenumber spectrum
f_o	Coriolis parameter at a given latitude
g	gravitational acceleration
k	zonal wavenumber, positive to the east
k_H	horizontal wavenumber, $k_H^2 = k^2+l^2$
K	kurtosis
l	meridional wavenumber, positive to the north
L	length scale, $\lambda = 2\pi L$
M	Rossby wave steepness parameter obtained with U
M*	Rossby wave steepness parameter obtained with U*
N	Brunt-Vaisala frequency
n	number of observations
n_i	number of independent observations
p	spectral power-law exponent
Q	intermittency factor
R	radius of the earth, R = 6371 km
Ro	Rossby number
r_i	internal Rossby deformation radius
S	standard deviation
T	mid-thermocline temperature perturbation, vertically-averaged from 150 to 200 m or from 350 to 400 m
U	baroclinic (0-400m) velocity scale
U*	upper bound of the true velocity scale
W	skewness
β_o	meridional gradient of the Coriolis parameter at a given latitude
β^*	sphericity parameter
Θ	latitude
λ	wavelength, $\lambda = 2\pi L$

LIST OF ABBREVIATIONS

Geographic Regions

NWA	Northwest Atlantic, a high-energy region
NWP	Northwest Pacific, a high-energy region
NEA	Northeast Atlantic, a low-energy region
SA	South Atlantic, a low-energy region
NEP	Northeast Pacific, a low-energy region
SP	South Pacific, a low-energy region
HIGH	composite high-energy region consisting of the NWA and NWP regions
LOW	composite low-energy region consisting of the NEA, SA, NEP and SP regions
NPSF	North Pacific Subtropical Front, a subregion of the NEP in the vicinity of the subtropical front
NPEC	North Pacific Equatorial Current, a subregion of the NEP in the vicinity of the equatorial current

Data Sources and Instruments

CAF	Canadian Armed Forces
USN	United States Navy
NODC	National Oceanographic Data Center (United States)
XBT	expendable bathythermograph
SXBT	ship-launched expendable bathythermograph
AXBT	air-launched expendable bathythermograph

Oceanographic Parameters

T-S	temperature-salinity
S-Z	salinity-depth

T-Z	temperature-depth
SSS	sea surface salinity
EKE	eddy kinetic energy
EPE	eddy potential energy

Quasigeostrophic Dynamics

LRW	linear Rossby wave
NRW	nonlinear Rossby wave
QGT	quasigeostrophic turbulence

Miscellaneous

UBC	University of British Columbia
RRMC	Royal Roads Military College
RMS	root-mean-square
ACF	autocorrelation function

LIST OF TABLES

LIST OF FIGURES

ACKNOWLEDGEMENTS

Financial support was received from a number of sources and is gratefully acknowledged. These include: a research assistantship (1981-85) from a contract with the Defence Research Establishment-Pacific held by W.J. Emery (UBC) and D.P. Krauel (RRMC), several teaching assistantships (1981-85) from the Department of Oceanography, UBC, a research assistantship (1985-86) from a Natural Science and Engineering Research Council Strategic Grant held by L.A. Mysak (UBC), K. Groot (PBS) and K. Hamilton (McGill), and part-time employment and typing services for the production of this thesis (1985-86) from Dobrocky Seatech Ltd., Sidney, B.C..

The ship-of-opportunity program could not have been successfully completed without the cooperation and assistance of the Defence Research Establishment-Pacific, the officers and crews of the nineteen Canadian Armed Forces vessels that participated, P. Nowlan (UBC) and N. Sutherland (RRMC). R. Thomson kindly provided access to the UBC computing system from Sidney, B.C.

The guidance from my research supervisor, W. J. Emery, and my supervisory committee, consisting of D.P. Krauel, P.H. LeBlond and S. Pond, is gratefully acknowledged. A special acknowledgement is extended to L.A. Mysak for his encouragement and support over the last two years. I am grateful to M. Bowman for his review of the thesis and short tenure on the supervisory committee. Beneficial discussions were held with A. Bennett, A. Blaskovich, D. Dunbar, J. Harper, G. Louttit, P. Greisman and G. Swaters. The courier and hostelry services of A. Weaver, the heroic typing exploits of D. Duncan and the substantial contributions of time and effort by my Mom and Dad to proofreading this thesis were very much appreciated.

A very special thanks is due to Joanne, Keith and Elizabeth for their inspiration and support during my studies at UBC and for living in poverty with a tyrant for the last year (or so).

I. INTRODUCTION

The purpose of this investigation is to determine the geographic variability of the synoptic statistics and dynamics of the oceanic mesoscale (i.e. 100 to 1000 km wavelengths) from quasi-synoptic expendable bathythermograph (XBT) surveys. A data set was compiled of quasi-synoptic single-ship trans-oceanic XBT sections and multiship/AXBT surveys, obtained from the Canadian Armed Forces, the United States Navy and the National Oceanographic Data Center. These data were sorted into six geographic regions in the Pacific and Atlantic Oceans. The geographic variability of the descriptive fields and wavenumber statistics will be discussed and the governing dynamics will be inferred from several dynamical models. It is hypothesized that the dominant length and velocity scales of the baroclinic motions exhibit a geographic variability similar to that which has been demonstrated for the intensity of the mesoscale perturbations using climatological data sets, and that these scales reflect a geographic variability of the governing mesoscale dynamics.

The existence of dynamic features of mesoscale dimensions, in the form of disturbances or discrete eddies in the mean flow, has been known since at least 1936 when Iselin noted a strong isolated eddy north of the Gulf Stream. The beginnings of concentrated investigations into transient ocean currents came in the 1950s with a series of cruises led by Fuglister, to map the instantaneous form of the Gulf Stream and the rings of current thrown off to the north and south. Swallow's floats in the same decade clearly showed deep discrete eddies with depths of up to 4000 m and currents exceeding 10 cm/s (Rhines, 1977).

Extensive work has since been done to investigate this mesoscale variability using a wide variety of data bases. Classical hydrographic surveys in the North Pacific (Roden, 1977) have shown wavelike disturbances with wavelengths between 400 and 600 km in the region of 20° to 50°N, which were shown to be consistent with several idealized models of free linear Rossby waves. Historical hydrographic and XBT data have been used to determine the distribution, number and movement of the Gulf Stream Rings in the Sargasso Sea with respect to the general circulation (Parker, 1971; Lai and Richardson, 1977; Ebbesmeyer and Taft, 1979). Satellite-tracked buoys have been able to trace the evolution of several Gulf Stream Rings quite successfully

(Richardson, 1979). Several investigators have analysed long time series of hydrographic and XBT data at Ocean Weather stations (White and Walker, 1974; Emery and Magaard, 1976). Remote-sensing techniques have been employed to study the variability of the sea surface temperature field (Saunders, 1972b; Holloday and O'Brien, 1975; Deschamps et al., 1981; Van Woert, 1982). Valuable descriptions of the geographic inhomogeneity of the mesoscale variability have been provided by utilizing the historical ship drift data file (Wyrtki et al., 1976), the historical hydrographic data file (Lutjeharms and Baker, 1980), the historical XBT data file (Dantzler, 1977; Emery, 1983a) and satellite altimetry from SEASAT (Cheney et al., 1983; Fu, 1983) and GOES-3 (Robinson et al., 1983).

In the last decade, the capability of XBTs to obtain quasi-synoptic coverage of large regions of the ocean has been demonstrated. Saunders (1971) observed the evolution of an isolated eddy north of the Gulf Stream with AXBTs. Bernstein and White (1974) determined a dominant wavelength of 600 km with several sets of XBTs in the North Pacific subtropical gyre. The same investigators (1977), with a different set of XBT data in the mid-latitude North Pacific, observed an order of magnitude decrease in the energy distribution at 500 to 1000 km wavelengths east of 170°W. Similar investigations were conducted in the Newfoundland Basin (Schmitz, 1981) and adjacent to South Africa (Lutjeharms, 1981). Ship-of-opportunity programs using XBTs have been, and are continuing to, yield substantial amounts of data over space and time (White and Bernstein, 1979).

POLYGON (Koshlyakov and Grachev, 1973), MODE (MODE Group, 1975 and 1978) and POLYMODE (Robinson, 1982) have contributed significantly to the knowledge of mesoscale dynamics, with intense surveys of specific regions of the ocean. A picture of the diversity of the quasigeostrophic dynamics has emerged. At one extreme, the motions can be represented as linear wave processes. At the other extreme, the motions can be completely nonlinear and turbulent.

The potential of quasi-synoptic XBT data for examining mesoscale statistics and dynamics has not as yet been exploited. Similarly, their use for determining the geographic variability has only been touched on. It is the intent of this investigation to use quasi-synoptic XBT surveys to make a statement about the geographic variability of the statistics and the dynamics of the oceanic mesoscale motions. The thesis comprises six chapters. Chapter

II describes the collection and processing of the quasi-synoptic XBT data set. The descriptive analyses are in Chapter III. Geographic regions with different length scales and amplitudes of the mesoscale structure are delineated and the descriptive characteristics of the eddy variability in each region are examined with typical temperature sections and maps. Chapter IV contains the statistical analyses. Two variables are used to represent the mesoscale variability - the mid-thermocline temperature and the geopotential anomaly (0 - 400 m). The central moments and the wavenumber spectra of these variables are used to discuss the geographic variability of the mesoscale eddy field. The seasonal variability of the mesoscale fields are examined for the Northeast Pacific, the region with the most even distribution of surveys over the four quarters of the year. The geostrophic velocity spectra are obtained from the geopotential anomaly spectra and the eddy kinetic energies are estimated. The dominant length and velocity scales for each region are determined from the wavenumber spectra. In Chapter V, the applicability of quasigeostrophic dynamics is inferred by evaluating the quasigeostrophic scaling parameters and the Rossby wave steepness parameter. The properties of free linear baroclinic Rossby waves are examined and the wavenumber spectra are compared with several models of nonlinear geophysical turbulence. The conclusions, in Chapter VI, summarize the geographic variability of the statistics and the inferred dynamics.

It is important to define several key terms used throughout the thesis. The oceanic mesoscale is a high-wavenumber band (i.e. 100 to 1000 km wavelengths) of variability compared to the large-scale mean flow of the ocean currents, which is comparable to the internal Rossby deformation radius. Due to the statistical methods employed in this study, a convenient representation of length scales is the wavelength (Bernstein and White, 1977). The wavelength (λ) of a feature is related to its length scale (L) by the relation (Emery et al. 1982), $\lambda = 2\pi L$. The term "eddy" applies to the description of all mesoscale perturbations. It includes individual closed circulation cells and space/time velocity or property fluctuations caused by a wide variety of circulation features (Emery, 1983b). The term "eddy" has no connotations of origin, dynamical behavior or rotational motion. A "discrete eddy" or "isolated eddy" is used to signify individual closed circulation features with a rotational motion. The term expendable bathythermograph (XBT) includes both air-launched (AXBT) and ship-launched (SXBT) probes. This term does not include mechanical bathythermographs (MBT). A list of the symbols and

a list of the abbreviations used regularly throughout the thesis can be found immediately after the Table of Contents.

II. THE DATA SET

The collection and processing of the quasi-synoptic XBT data set is described in this chapter. In order to examine the mesoscale structure over a large portion of the Pacific and Atlantic Oceans, 83 sets of XBT data were obtained. These data comprise over 10,000 individual XBTs acquired from the Canadian Armed Forces (CAF), the United States Navy (USN), and the United States National Oceanographic Data Center (NODC). These temperature-depth (T-Z) profiles were filtered subjectively to delete questionable data; salinity was inferred using historical temperature-salinity (T-S) and salinity-depth (S-Z) curves; and several oceanographic variables were calculated for the analyses of the mesoscale eddy variability.

A. DATA COLLECTION

The XBT data set, obtained from the CAF, USN and NODC, provides a reasonable coverage of the Pacific and Atlantic. Figure II-1 shows the locations of these data on a Mercator projection of the oceans. The CAF data were procured by managing and implementing a ship-of-opportunity program with the Canadian Navy, while the USN and NODC data were acquired from archived files.

The Canadian Armed Forces Data

CAF destroyer squadrons were used in a ship-of-opportunity program from February 1980 to June 1983 to collect quasi-synoptic SXBT data. These data were obtained on a contract from the Defence Research Establishment - Pacific to W.J. Emery and D.P. Krauel. Eleven cruises were conducted, resulting in ten trans-oceanic single-ship sections and nine multiship surveys in the Pacific and North Atlantic Oceans.

Data were collected on the return passage of CAF destroyer squadrons from overseas deployments when the course was, for the most part, directly to Canada. On each cruise, SXBTs and sea surface salinities (SSSs) were taken hourly from one of the ships for the entire voyage. The squadrons generally cruised at speeds of 13 knots, resulting in a high sampling density of one SXBT and SSS per 25 km over ranges of about 4000 km. Depending on operational and

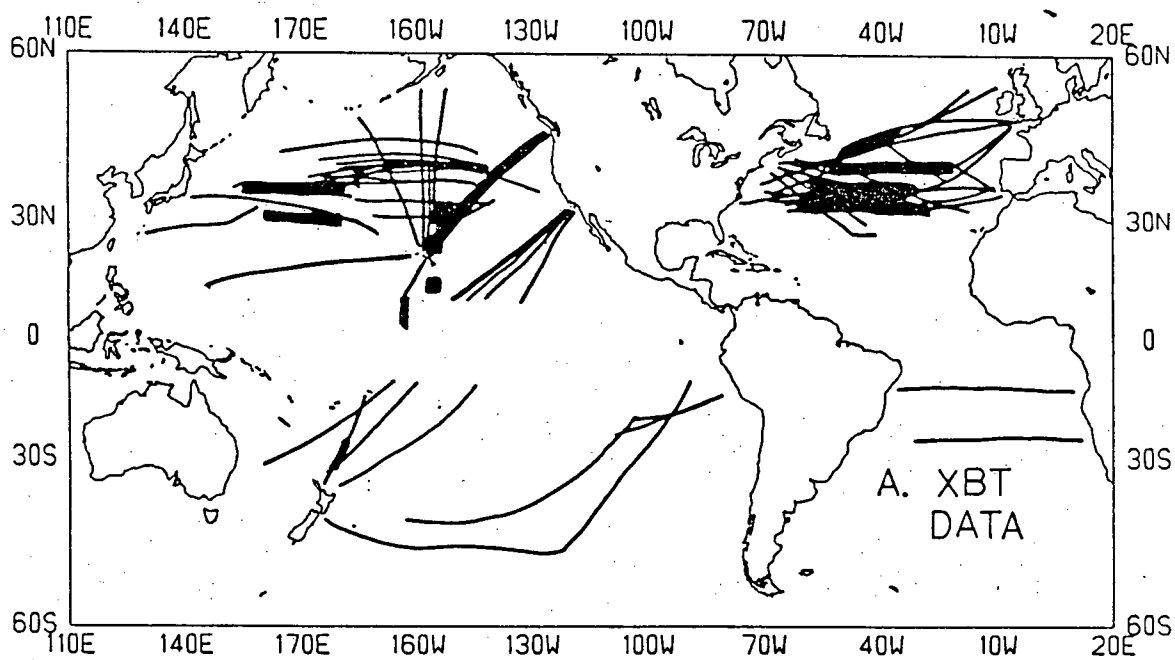

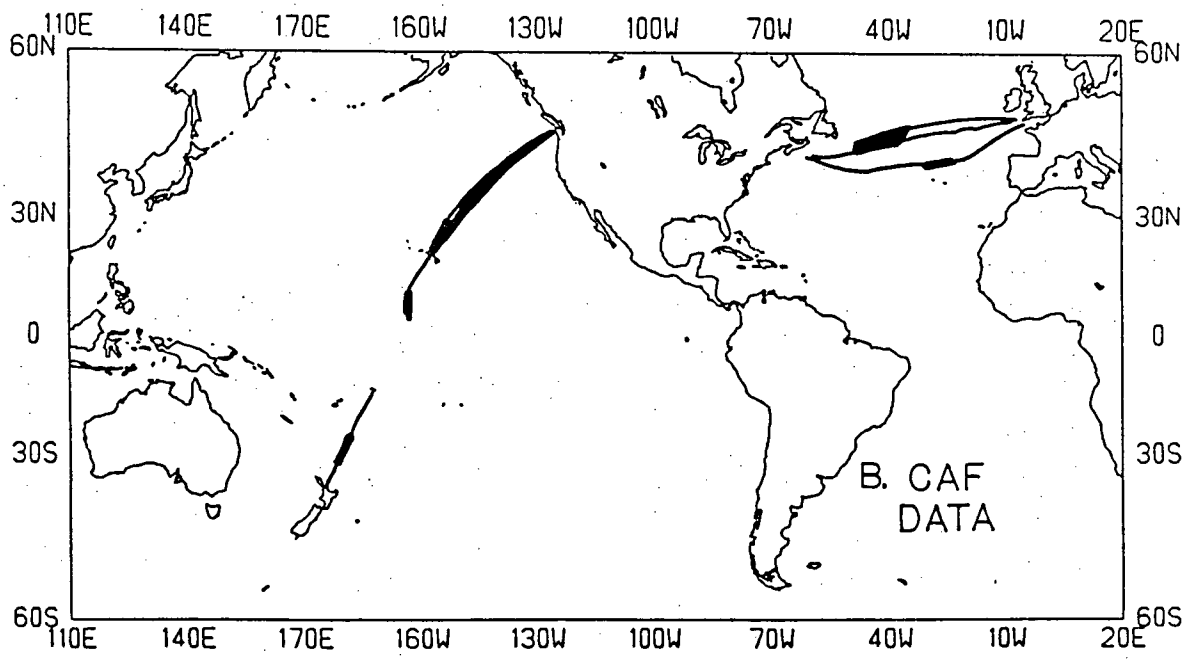

Figure II-1 Locations of the XBT data used in this investigation.
a. All of the XBT data.
b. CAF data.

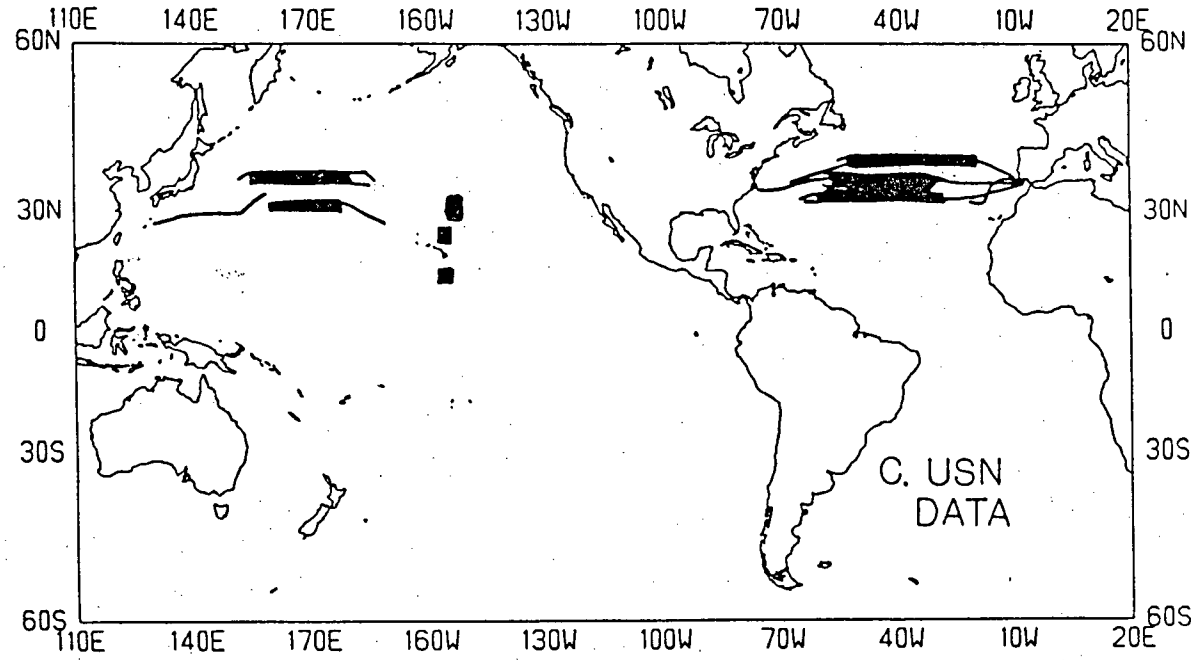

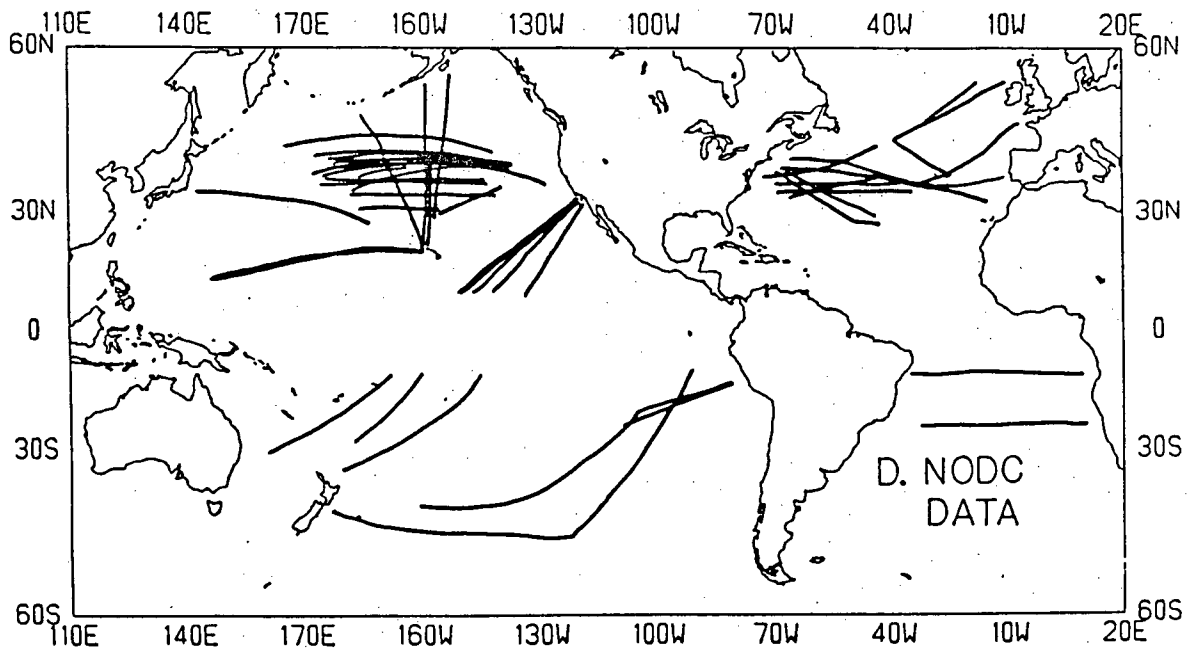

Figure II-1 Continued.
c. USN data.
d. NODC data.

training requirements, multiship surveys were conducted. The coverage of these surveys varied from 40 to 180 km in width and 600 to 1300 km in length with three or four ships. Each of Canada's four destroyer squadrons participated in this observational program - a total of 19 different destroyers and supply ships. An on-board scientist, technician or student from the University of British Columbia (UBC) or Royal Roads Military College monitored and assisted with the collection of the data on each cruise. They were responsible for on-site quality control and coordination of the multiship surveys.

The Sippican XBT system is widely used, so the details will not be discussed here. Most of the CAF ships had SXBT systems consisting of Sippican MK2A-1 strip-chart recorders and deck-mounted launchers. A MK2A-1 strip-chart recorder and hand-held launcher were used on the ships without systems. The T-4 probes (460 m) were provided by the CAF's supply system. The reported accuracy of the T-4 probe is $\pm$0.2°C and 5 m or $\pm$2% whichever is greater (Anderson, 1979; Sippican, 1975). The SXBTs were taken every hour and faulty or suspect SXBTs were immediately repeated. As a rule of thumb, no more than two probes were used on each station. The XBT systems were tested prior to each cruise using the XBTester Model A-4 for temperature calibration, servo-amplifier gain, launcher installation resistance and servo response. The calibration was subsequently checked every six hours.

The temperature profiles were visually inspected for failures and suspect traces (Department of the Navy, 1978) upon returning from each cruise. The good T-Z traces were digitized at the inflection points, such that linear interpolation would provide reasonable temperatures for all depths. The digitized values were corrected for the nonlinearity of the trace due to the fall rate (depth) and the servo-amplifier response (temperature) according to Sippican's XBT system linearity equations (Sippican, 1970). These operations were performed on a Datatizer DTR-3036 (GTO Corporation) and LSI-11/23 minicomputer. The data were transferred to UBC's Amdahl V8 mainframe computer.

SSS was obtained from bucket samples taken immediately after each SXBT. The samples were retained in 4 oz glass sample bottles and returned to UBC for analysis. The conductivity ratios were measured using a Guildline Autosal

Model 8400 salinometer. The salinities were estimated using the Practical Salinity Scale, 1978 (Pond and Pickard, 1983). The Guildline Autosal salinometer has a manufacturer's reported accuracy of $\pm.003 \times 10^{-3}$ equivalent salinity. The salinities of the first two cruises, in the Northeast Pacific, were originally estimated using the 1966 UNESCO tables. Although the differences between these two methods of estimating salinity is less than $.003 \times 10^{-3}$, over the observed range of salinity (32 to 36 $\times 10^{-3}$), the corrections were made. Thus, SSSs used in this investigation have been estimated from, or corrected to, the Practical Salinity Scale, 1978.

The navigational methods employed varied depending on the vessel and the location, in order to obtain the best possible absolute and relative fix. Radar fixes on points of land, satellite navigation, Loran-C and Omega were used. When possible, during multiship surveys, radar fixes were taken on adjacent ships. Overall, the absolute navigation was considered to be much better than $\pm$ 5 km.

The CAF data were formatted and archived for further processing along with the USN and NODC data. A detailed data report of the CAF data was prepared (Thomson et al., 1984b).

The United States Navy Data

The USN data used in this investigation were collected in three separate programs and obtained from archived data files. Data from six trans-oceanic multiship SXBT surveys, conducted in the North Pacific and North Atlantic by Wilson and Dugan (1978), were acquired. These data were previously used to investigate various aspects of the mesoscale eddy variability (Emery et al., 1979; Emery et al., 1980; Harrison et al., 1983). Also, two data sets from AXBT surveys conducted by the USN, were procured. The first set is from eight surveys northeast of Hawaii in the region of the subtropical front, collected by Miyaki (Miyaki, 1981). The second set is from a series of five surveys obtained from the United States Naval Research Laboratory in Washington, D.C. (Emery, personnal communication) - one survey on the subtropical front northeast of Hawaii and four surveys in the North Pacific Equatorial Current south of Hawaii. These two data sets of AXBT surveys have not been published, nor have they been used to study the eddy variability of these regions.

Model 8400 salinometer. The salinities were estimated using the Practical Salinity Scale, 1978 (Pond and Pickard, 1983). The Guildline Autosal salinometer has a manufacturer's reported accuracy of $\pm.003 \times 10^{-3}$ equivalent salinity. The salinities of the first two cruises, in the Northeast Pacific, were originally estimated using the 1966 UNESCO tables. Although the differences between these two methods of estimating salinity is less than $.003 \times 10^{-3}$, over the observed range of salinity (32 to 36 $\times 10^{-3}$), the corrections were made. Thus, SSSs used in this investigation have been estimated from, or corrected to, the Practical Salinity Scale, 1978.

The navigational methods employed varied depending on the vessel and the location, in order to obtain the best possible absolute and relative fix. Radar fixes on points of land, satellite navigation, Loran-C and Omega were used. When possible, during multiship surveys, radar fixes were taken on adjacent ships. Overall, the absolute navigation was considered to be much better than $\pm$ 5 km.

The CAF data were formatted and archived for further processing along with the USN and NODC data. A detailed data report of the CAF data was prepared (Thomson et al., 1984b).

The United States Navy Data

The USN data used in this investigation were collected in three separate programs and obtained from archived data files. Data from six trans-oceanic multiship SXBT surveys, conducted in the North Pacific and North Atlantic by Wilson and Dugan (1978), were acquired. These data were previously used to investigate various aspects of the mesoscale eddy variability (Emery et al., 1979; Emery et al., 1980; Harrison et al., 1983). Also, two data sets from AXBT surveys conducted by the USN, were procured. The first set is from eight surveys northeast of Hawaii in the region of the subtropical front, collected by Miyaki (Miyaki, 1981). The second set is from a series of five surveys obtained from the United States National Research Laboratory in Washington, D.C. (Emery, personnal communication) - one survey on the subtropical front northeast of Hawaii and four surveys in the North Pacific Equatorial Current south of Hawaii. These two data sets of AXBT surveys have not been published, nor have they been used to study the eddy variability of these regions.

The National Oceanographic Data Center Data

The NODC XBT (1984) geographic file (NODC, 1984) was searched for quasi-synoptic sections. Initially the file was sorted by cruise designation number and consecutive XBT number. All cruises with more than 25 XBTs, in water deeper than 500 m, were removed for further examination. This yielded 486 cruises. The following criteria were used to identify 53 single-ship cruises with a quasi-synoptic quality comparable to the CAF and USN data:

a. cruise paths must be reasonably straight transects across oceanic regions of interest;

b. the XBT spacing must be less than 200 km (Although this does not provide the same high-wavenumber resolution as the CAF and USN data, it provides a more efficient ratio of number of samples to independent observations);

c. the time between XBT casts must be less than 6 hours; and

d. the cruise tracks must be at least 1000 km in length.

B. DATA PROCESSING

The data set was processed to obtain several oceanographic variables for the subsequent descriptive and statistical analyses. This processing included a visual examination of the digitized T-Z data, the inference of salinity from T-S and S-Z curves and the calculation of several oceanographic variables.

XBT Traces

Spatial series of XBTs were produced for each cruise and visually inspected to check for faulty or suspect XBTs and digitization errors. Figure II-2, as an example, is the SXBT spatial series of the HMCS Provider, from Hawaii to Vancouver Island in March 1980. Temperature was linearly interpolated to 10 m increments of depth for each trace and the data from the three sources were converted to a common format.

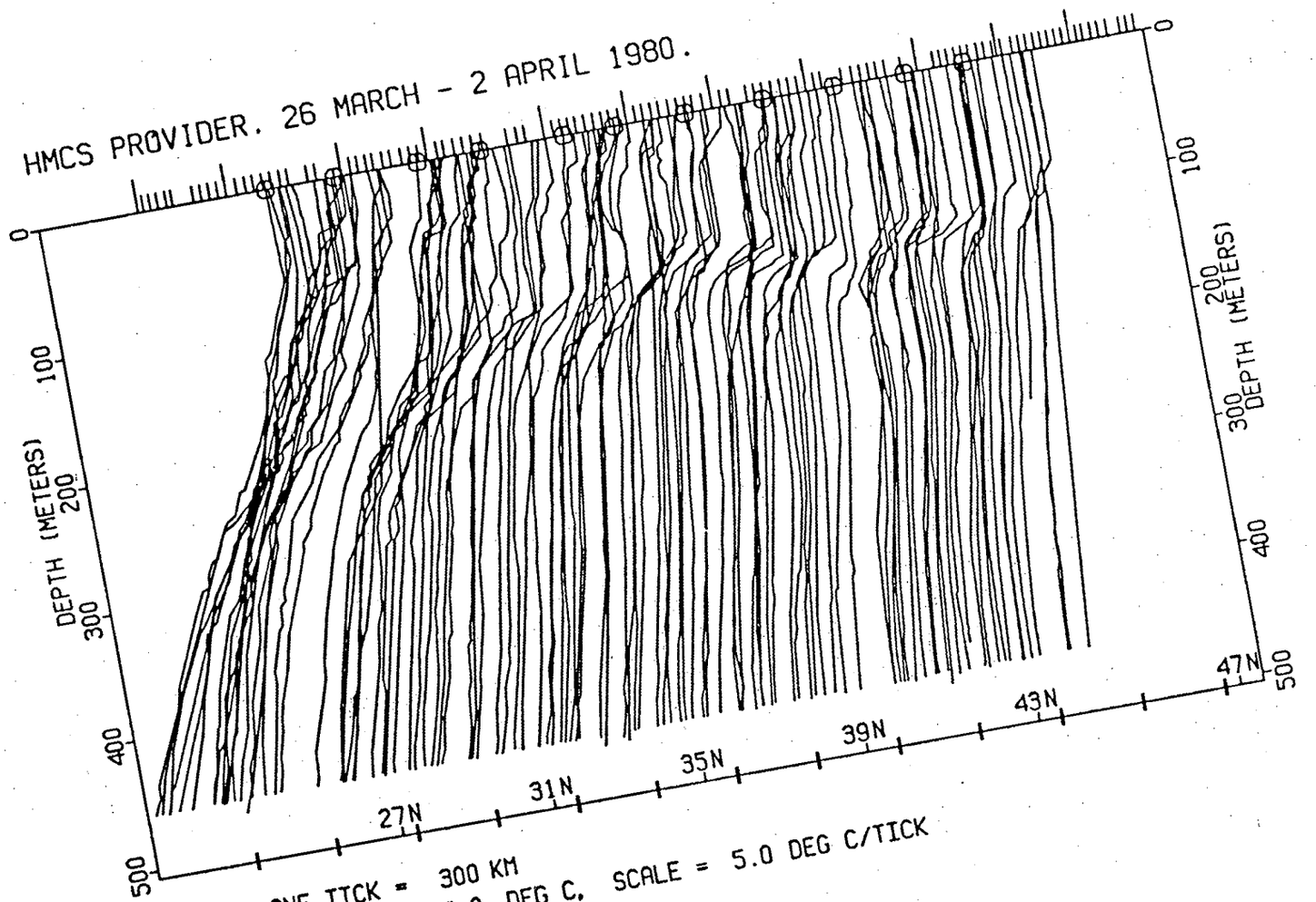

Figure II-2 An example of the XBT spatial series produced for each cruise to check for digitization errors. The above cruise was conducted by the HMCS Provider from Hawaii to Victoria.

Salinity Inference

Salinity was inferred for each XBT to estimate density fields and calculate geopotential anomalies. Mean T-S and S-Z curves from Emery and Dewar (1982) and Pickard and Emery (1982) were used to infer salinity. The accuracy of inferring salinity fields by this method was examined by comparing the bucket SSS from the CAF data and the inferred SSS.

Emery and Dewar computed mean T-S and S-Z curves for all 5° squares in the Pacific and Atlantic, north of 10°S, using NODC's hydrographic (1978) file. Hydrocasts made in water shallower than 500 m were not used, so these curves represent the oceanic waters beyond the continental shelf-break. Following the method proposed by these investigators, salinity was inferred using the T-S curves, except in the regions north of 40°N in the Pacific and northwest of 50°N, 45°W in the Atlantic. In these two areas, Emery and Dewar found that the root-mean-square (RMS) error, between the dynamic height using the inferred salinity and the dynamic height using the measured salinity, was less with the S-Z curves than with the T-S curves. S-Z curves were, therefore, used to infer salinity in these two regions. Mean T-S curves for the Southwest Pacific, the Southeast Pacific, the Pacific Sub-Antarctic and the South Atlantic were obtained from Pickard and Emery (1982), for use south of 10°S. The mean T-S curves from Pickard and Emery (1982) are heuristic and therefore not precise. Their use is considered to be substantially better than using a mean salinity and is consistent with the method used to infer salinity north of 10°S. Figure II-3 presents a map of the Pacific and Atlantic showing specifically in which regions the above T-S and S-Z curves were used to infer salinity.

Salinity was inferred for each T-Z profile using a weighted average of the appropriate curves of the four closest 5° squares. The T-S or S-Z curves were weighted by the inverse of the square of the distance from the center of each square to the XBT. It was found that inferring salinity solely on the basis of the curve of the 5° square containing the XBT created false salinity and density features in the regions of oceanic fronts. The use of a weighted average of the four closest squares solved this problem.

As a check on the accuracy of employing mean curves for inferring salinity, plots of the inferred SSS and the bucket SSS for each of the CAF cruises (where water samples were collected) were created (Figure II-4). These plots show

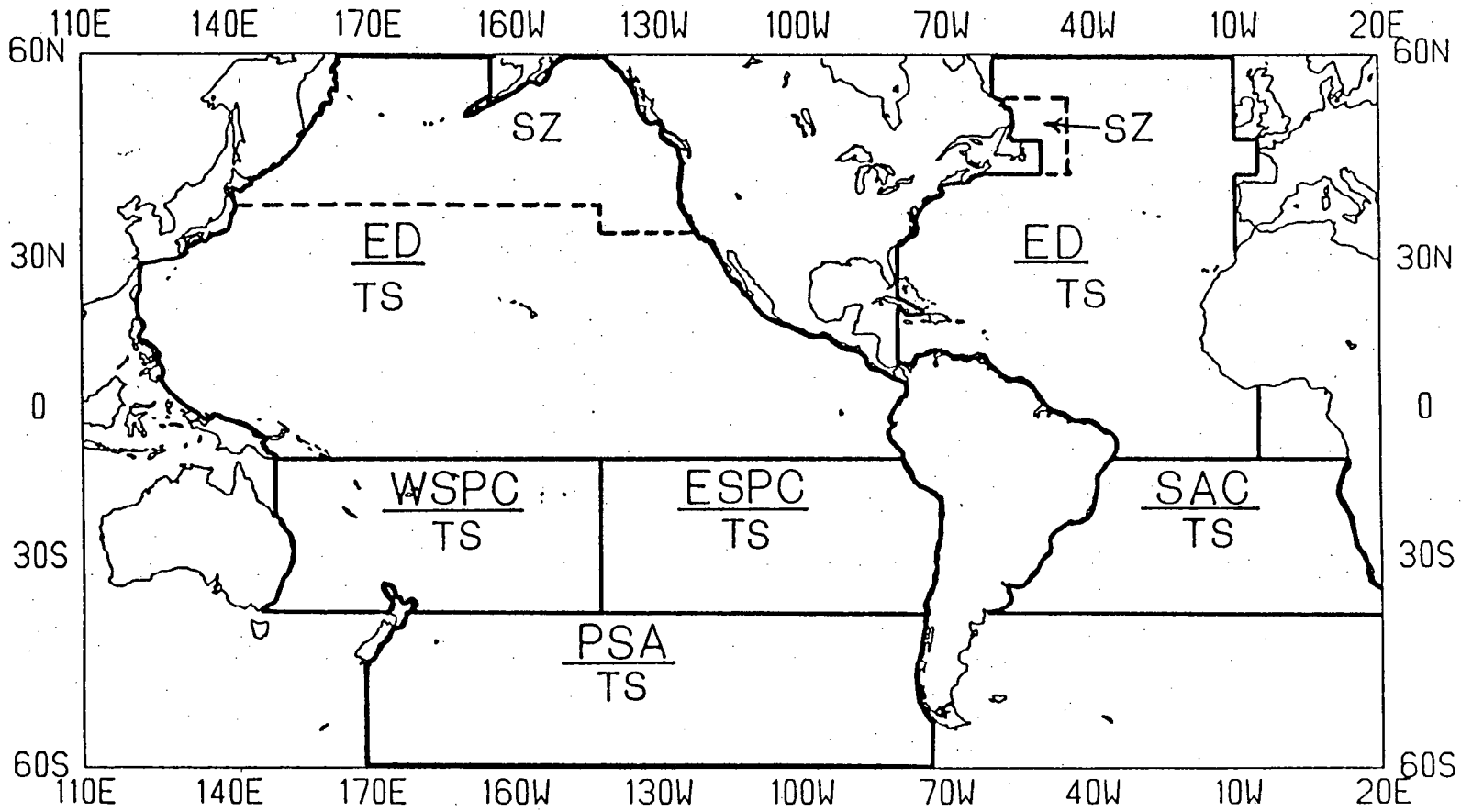

Figure II-3 Map of the Pacific and Atlantic Oceans showing the T-S and S-Z curves used to infer salinity. In the regions denoted ED, the mean curves from Emery and Dewar (1982) for each 5° square were used. The temperature-salinity and the salinity-depth curves were used in the areas labelled TS and SZ, respectively. South of 10°S, the temperature-salinity curves obtained from Pickard and Emery (1982) were: West South Pacific Central (WSPC), East South Pacific Central (ESPC), Pacific Sub-Antarctic (PSA) and South Atlantic Central (SAC).

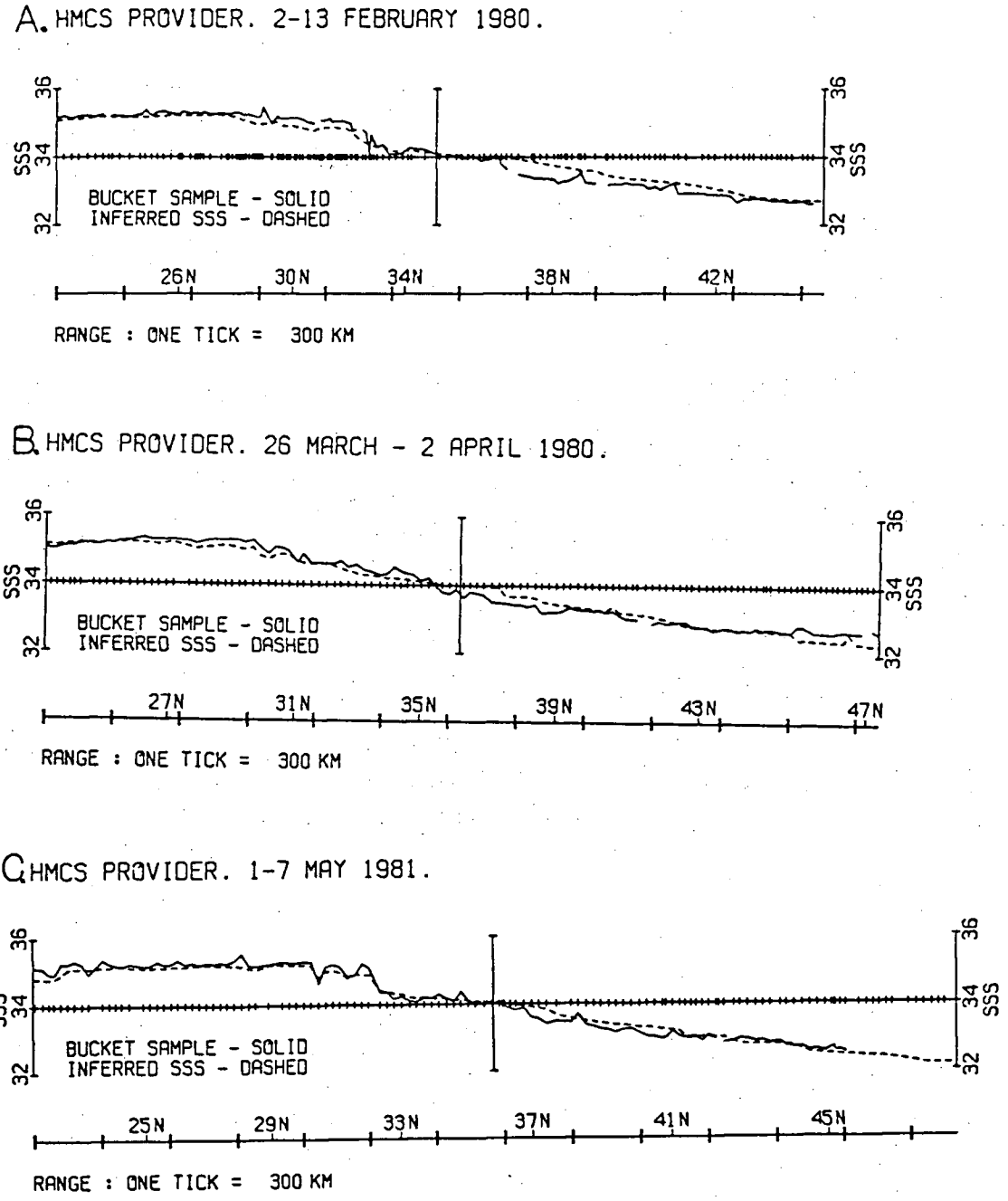

Figure II-4 **Plots of the inferred SSS and the bucket SSS for each of the CAF single-ship sections, where water samples were collected. For each cruise the two SSSs are plotted as a function of along-track range. The small ticks on the central axis are the SXBT positions where SSS has been inferred.**

D. HMCS SASKATCHEWAN. 17-24 NOVEMBER 1981.

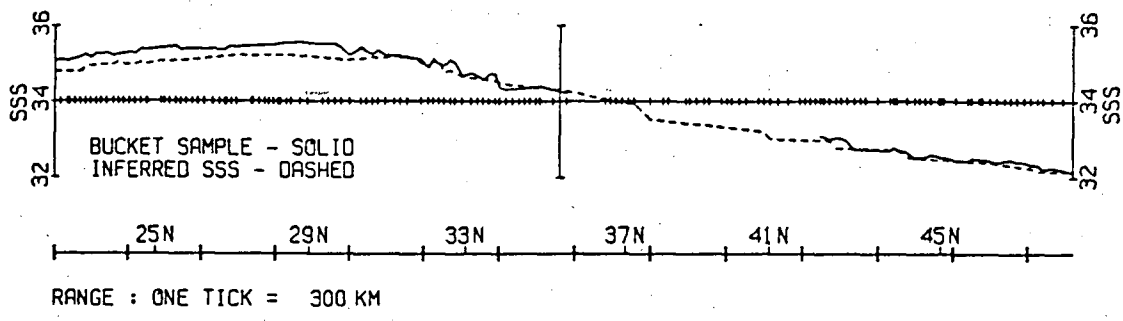

E. HMCS TERRA NOVA. 11-12 MAY 1982.

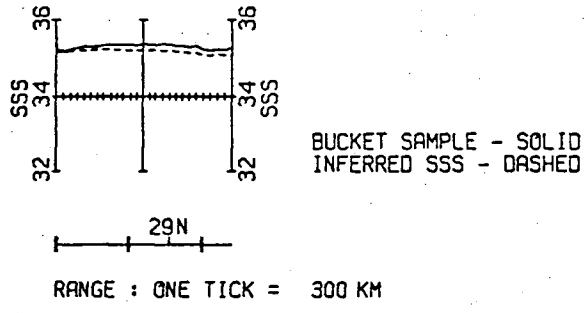

F. HMCS QU'APPELLE. 2-7 NOVEMBER 1982.

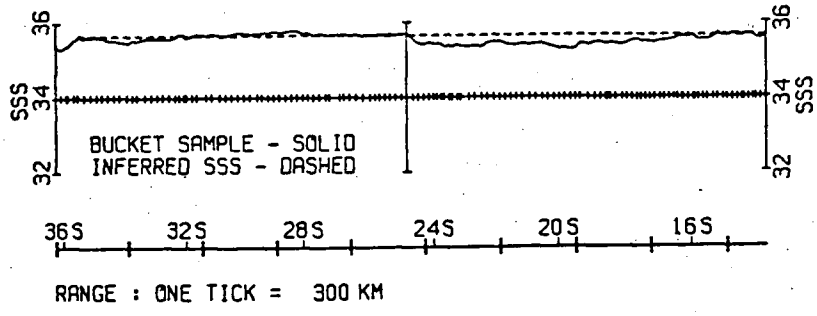

Figure II-4 Continued.

G. HMCS QU'APPELLE. 9-18 NOVEMBER 1982.

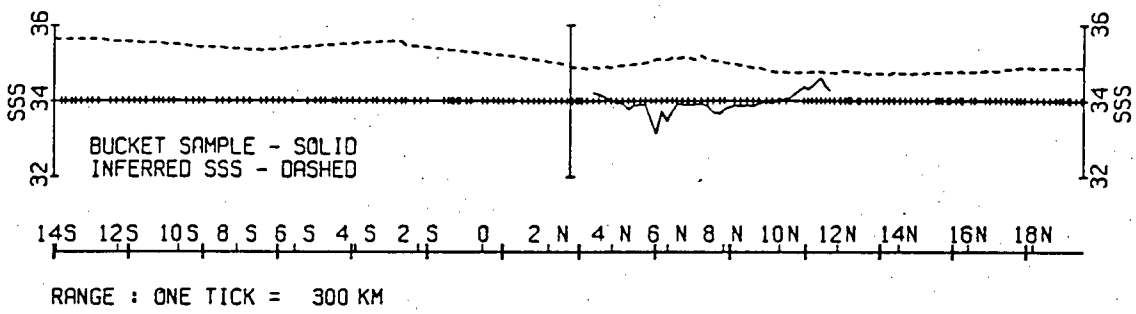

H. HMCS SAGUENAY. 2-8 OCTOBER 1981.

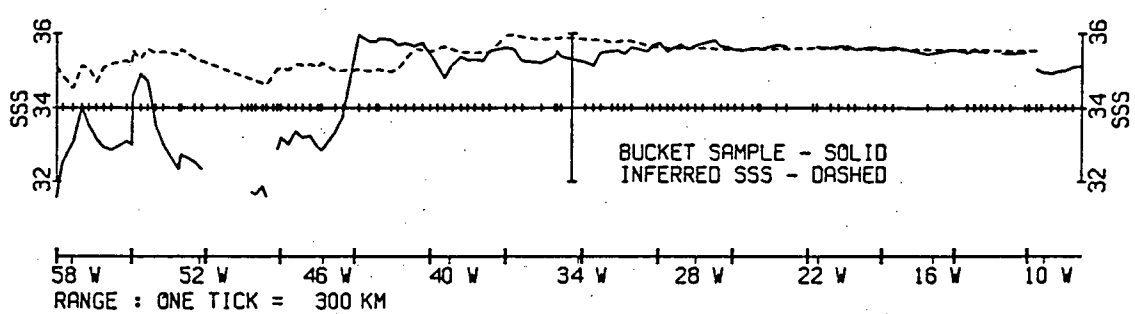

Figure II-4 Continued.

I. HMCS PRESERVER. 1-7 OCTOBER 1982.

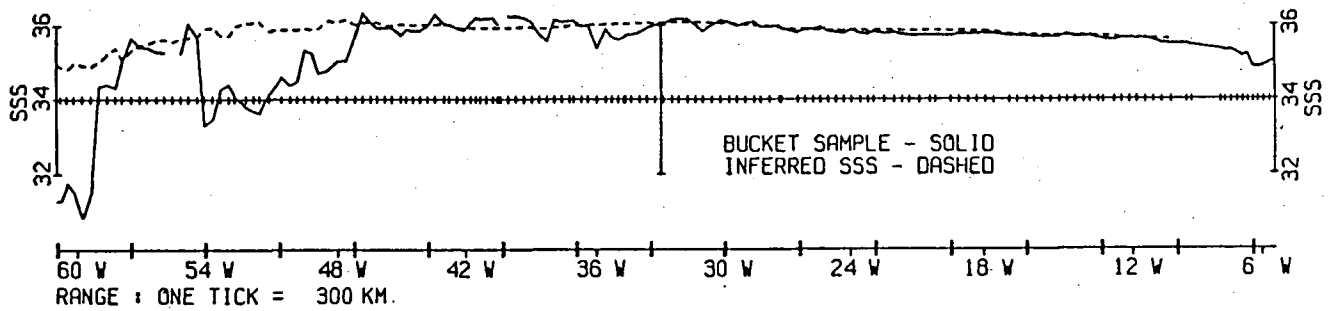

J. HMCS PROTECTEUR. 22-29 JUNE 1983.

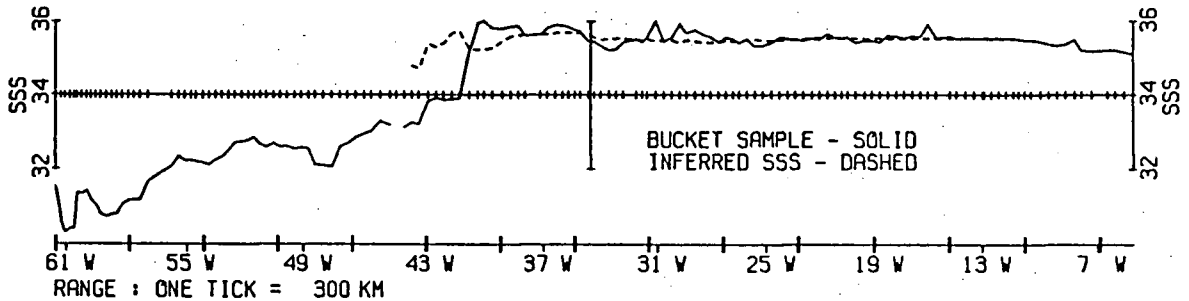

Figure II-4 Continued.

very reasonable agreement between the measured and inferred SSS. Notable exceptions were the western boundary current regions in the three Atlantic sections (Figures II-4 h-j) and the equatorial Pacific (Figure II-4 g). Table II-1 lists the RMS difference for each cruise. The sections in the northeastern and southwestern Pacific all have RMS differences no higher than 0.20×10^{-3}. The section across the central equatorial Pacific (Figure II-4 g) has an RMS difference of 1.07×10^{-3}. The inferred SSS exhibits the general meridional SSS characteristics of this region (Pickard and Emery, 1982: Figure 4.9) with a minimum at about 10°N increasing toward the north and south subtropical regions. The anomalously low bucket SSSs, across the North Pacific Equatorial Countercurrent, are due to the increased precipitation in this central equatorial region during the 1982-83 El Nino - Southern Oscillation (ENSO) event (Rasmusson et al., 1983). The three North Atlantic sections (Figures II-4 h-j) have high RMS differences due to difficulties associated with inferring salinity in the regions of the western boundary currents (Emery and Dewar, 1982). To the east of these regions, the bucket and inferred SSS show a very reasonable agreement. The differences in the western boundary current regions arise from applying mean T-S curves to T-Z profiles taken across a front separating water masses of very different T-S characteristics.

The anomalously low salinity values in the equatorial section will not protrude much deeper than the mixed-layer depth of about 60 m, so the T-S curves should provide reasonable salinity estimates for most of the water column. In the western boundary current regions, particularly where the data for this investigation were obtained, the T-S curves of Emery and Dewar (1982) are dominated by the contribution from offshore oceanic waters rather than the less saline continental shelf and slope waters. Thus, the eddy variability determined from the geopotential anomaly due to cold-core rings will be underestimated, which is much preferable to overestimating the eddy variability. For the above reasons, the method of inferring salinity from mean T-S curves in these regions is considered more appropriate and useful than using a mean salinity for the purposes of this investigation.

Oceanographic Variables

Further processing of the measured temperature and inferred salinity profiles were required for each XBT in preparation for the descriptive and

Table II-1 RMS differences between bucket SSS and inferred SSS for the CAF trans-oceanic sections shown in Figure II-4.

Ship	Date	Ocean	RMS Difference ($\times 10^{-3}$)
a. HMCS Provider	Feb 80	Northeast Pacific	0.17
b. HMCS Provider	Apr 80	Northeast Pacific	0.18
c. HMCS Provider	May 81	Northeast Pacific	0.15
d. HMCS Saskatchewan	Nov 81	Northeast Pacific	0.20
e. HMCS Terra Nova	May 82	Northeast Pacific	0.13
f. HMCS Qu'Appelle	Nov 82	Southwest Pacific	0.15
g. HMCS Qu'Appelle	Nov 82	Equatorial Pacific	1.07
h. HMCS Saguenay	Oct 81	North Atlantic	1.22
i. HMCS Preserver	Oct 82	North Atlantic	0.93
j. HMCS Protecteur	Jun 83	North Atlantic	0.54

statistical analyses. As will be discussed in Chapters III and IV, temperature will be used to examine the mesoscale variability in the mid-thermocline and the geopotential anomaly will be used to examine the baroclinic eddy variability in the upper layer (400 m) of the ocean.

The mid-thermocline temperature was calculated as vertical averages of the measured temperature over two 50 m segments of the water column (i.e. 150 to 200 m and 350 to 400 m). The applicability of these temperature variables for describing the mesoscale variability of the ocean will be discussed in Chapter IV. The geopotential anomaly from 0 to 4000 kPa (i.e. 0 to 400 db or 0 to 400 m) was calculated as the integral of the specific volume anomaly. This required the determination of the sigma-t profile from the measured temperature and inferred salinity. Sigma-t was obtained from the International Equation of State of Sea Water, 1980 (Millero and Poisson, 1981) with the given temperature and salinity at atmospheric pressure.

III. DESCRIPTIVE ANALYSES

The purpose of the descriptive analyses is to qualitatively discuss the geographic variability of the observed mesoscale structure. Geographic regions with different scales and amplitudes of mesoscale structure are defined and typical sections and maps of each region are used to examine the geographic variability of the thermal structure in the quasi-synoptic XBT data set.

A. GEOGRAPHIC REGIONS

Geographic regions with different horizontal scales and amplitudes of eddy variability were defined using the quasi-synoptic sections of each cruise, with the aid of previous work using climatological data sets (Wyrtki, 1975; Emery, 1983a; Cheney et al., 1983). These investigators examined the geographic variability of the mesoscale structure with the standard deviations of: dynamic height from archived hydrographic records, temperature and inferred dynamic height from archived XBT records, and sea surface altimetry from SEASAT. All three yielded similar results, with regions of high mesoscale variability near the western boundary currents and low variability in the interior of the ocean basins and in the eastern boundary currents. Cheney et al.'s results, using the SEASAT altimetry, were used to define approximate boundaries between regions of high and low eddy variability. These results were considered most appropriate for this purpose due to the global coverage and even distribution of the SEASAT altimetry data. Figure III-1, adapted from Cheney et al. (1983), shows the geographic variability of the eddy field with the standard deviation of the SEASAT altimetry.

Six geographic regions were defined using the SEASAT mesoscale variability, the observed structure in the quasi-synoptic data set and the geographic distribution of the data. These regions were classified, in a manner similar to that of Fu (1983), as areas of high or low eddy variability. The 6 cm contour in Figure III-1 was used as a guide to delineate the boundary between high- and low-energy regions. These geographic regions, classified by high- and low-energy levels, are:

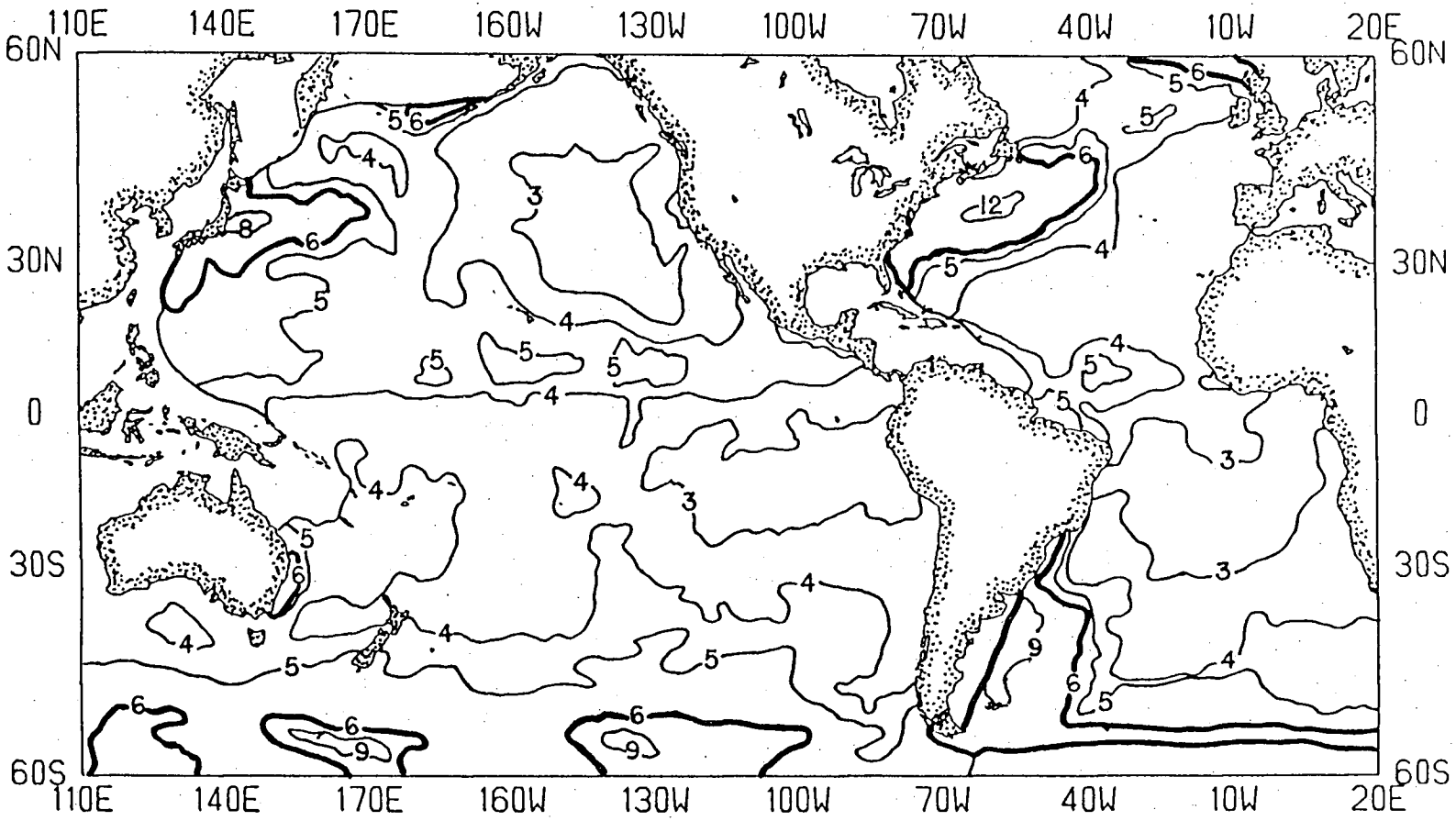

Figure III-1 Global mesoscale variability from collinear SEASAT altimeter ground tracks. The standard deviation of the altimetry is contoured in centimeters. The bold 6 cm contour separates regions of relatively high and low eddy activity.

High-energy Regions	Low-energy Regions
NWA - Northwest Atlantic	NEA - Northeast Atlantic
NWP - Northwest Pacific	SA - South Atlantic
	NEP - Northeast Pacific
	SP - South Pacific

Two composite regions were defined to represent the combined high-energy regions and the combined low-energy regions. The HIGH region comprises the NWA and NWP regions (i.e. the high-energy regions). The LOW region comprises the NEA, SA, NEP and SP regions (i.e. the low-energy regions).

The geographic distribution of the quasi-synoptic XBT data and the demarcation of the six geographic regions are shown in Figure III-2. The quasi-synoptic XBT data, from the single-ship sections and the multiship/AXBT surveys, were binned into the appropriate geographic regions. If a cruise passed through both high- and low-energy regions, it was divided where the section exhibited a marked change in the mesoscale expression. The resulting single-ship sections were discarded if they had less than 25 XBTs or were less than 1000 km in length. There are a total of 95 trans-oceanic single-ship sections (hereafter known as sections) and 29 multiship/AXBT surveys (hereafter known as surveys).

B. GEOGRAPHIC VARIABILITY OF THE THERMAL STRUCTURE

The purpose of this section is to describe the geographic variability of the baroclinic eddy field as expressed in the temperature structure of the XBT data set. Typical temperature sections from each geographic region are examined and compared to the geographic eddy variability revealed in previous works by researchers using climatological data sets. It is considered important to examine the qualitative aspects of the mesoscale variability in each region and to demonstrate that the eddy fields observed in the quasi-synoptic XBT data set are consistent with previous observations.

Three different climatological data sets have been used, by other investigators, to examine the global geographic variability of the mesoscale

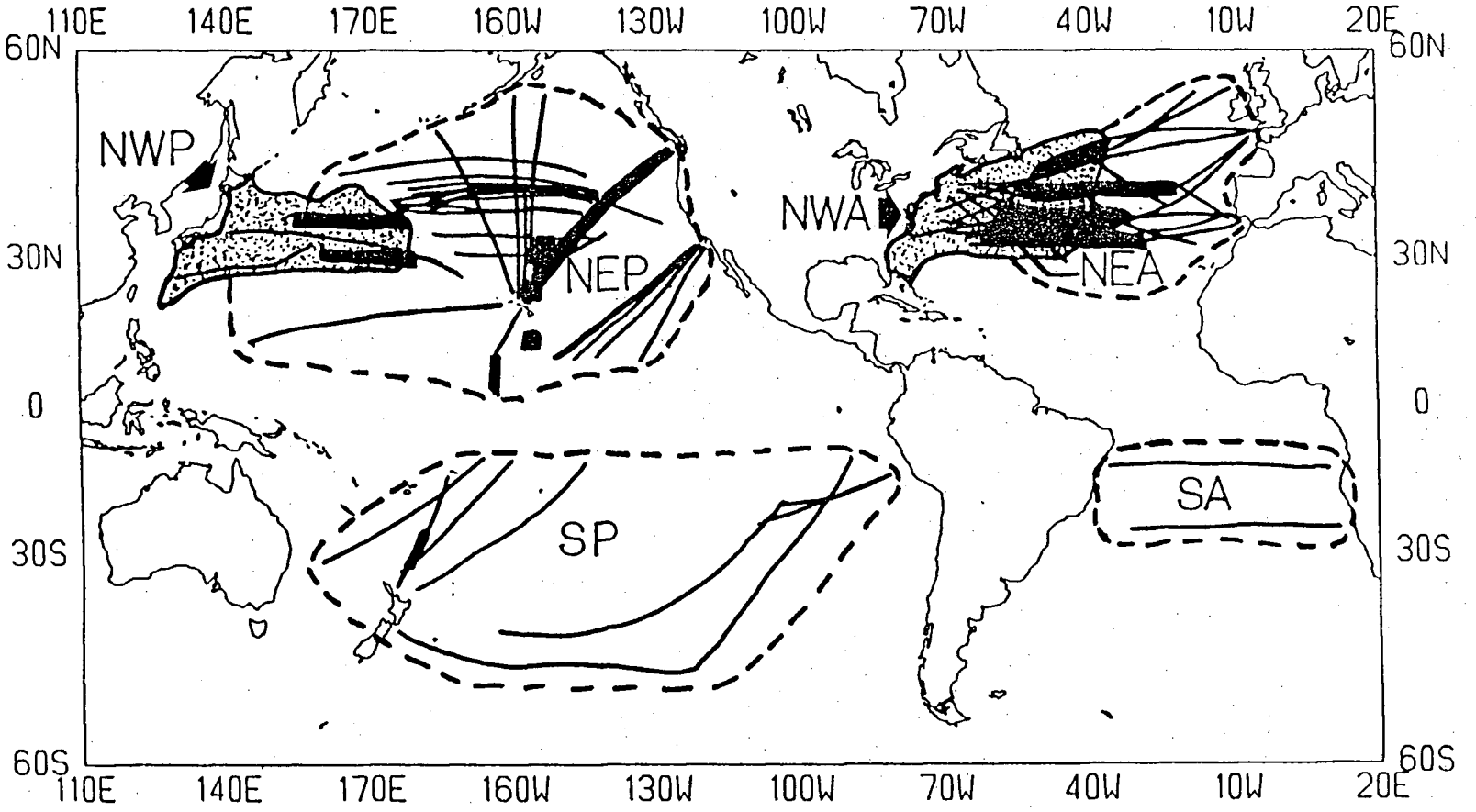

Figure III-2 The six geographic regions as defined for this investigation are shown with the XBT data set. The regions designated as high eddy energy areas are stippled.

eddy field. The global map of the eddy kinetic energy computed from the historical ship drift file (adapted from Wyrtki et al., 1976) is shown in Figure III-3. Figure III-1 presents the geographic variability of the eddy field obtained by Cheney et al. (1983) using the standard deviation of SEASAT altimetry. The standard deviation of temperature at 260 m, based on a variable grid analysis of the XBT file for the North Pacific and North Atlantic, has been adapted from Emery (1983a) in Figure III-4.

These three different studies offer views of the geographic variability of the global eddy field that show regions of high eddy activity near the western boundary currents and low eddy activity in the interior and eastern boundary current regions. As previously discussed, the 6 cm contour of the SEASAT altimetry deviation map (Figure III-1) has been used as a guide for delineating the high- and low-energy regions (Figure III-2). In Figure III-1, high values of 12 and 9 cm are found in the NWA and NWP, respectively. Low values of 4 cm are found in the NEA, with low values of 3 cm in the SA, NEP and SP. The standard deviation of the altimetry represents the eddy potential energy (EPE) of the barotropic signal. Since only a total of 24 days of data were used (in August of 1978), the energies at periods longer than 24 days were inadequately sampled. Fu (1983) determined the transfer function of this 24-day filter and found that the bulk of the mesoscale energy at periods from 50 to 150 days was severely suppressed.

The eddy kinetic energy (EKE) map (Figure III-3), as determined from ship drift data by Wyrtki et al. (1976), represents the barotropic signal. High- and low-energy regions, similar to those of Figure III-1, can be defined using the 600 cm^2/s^2 contour. The EKE has maximum values of over 2000 cm^2/s^2 in the NWA and over 1000 cm^2/s^2 in the NWP. Minimum values of about 300 cm^2/s^2 occur in the SA and SP. The ship drift data were not corrected for drift due to the wind acting on the vessels, thus overestimating the EKE. This overestimate and the seasonal signal of the winds and currents explains the distinct difference between Figure III-1 and III-3 in the equatorial regions of both the Pacific and Atlantic Oceans. Figure III-1 shows deviations of SEASAT altimetry of 5 cm in the equatorial regions, which are about one-half of the maximum values in the high-energy regions. Figure III-3 has equatorial values of about 1000 cm^2/s^2 which are equal to the maximum values in the NWA. The SEASAT altimetry implies a ratio of one-quarter for the eddy kinetic energies in the equatorial regions compared to the western boundary current regions.

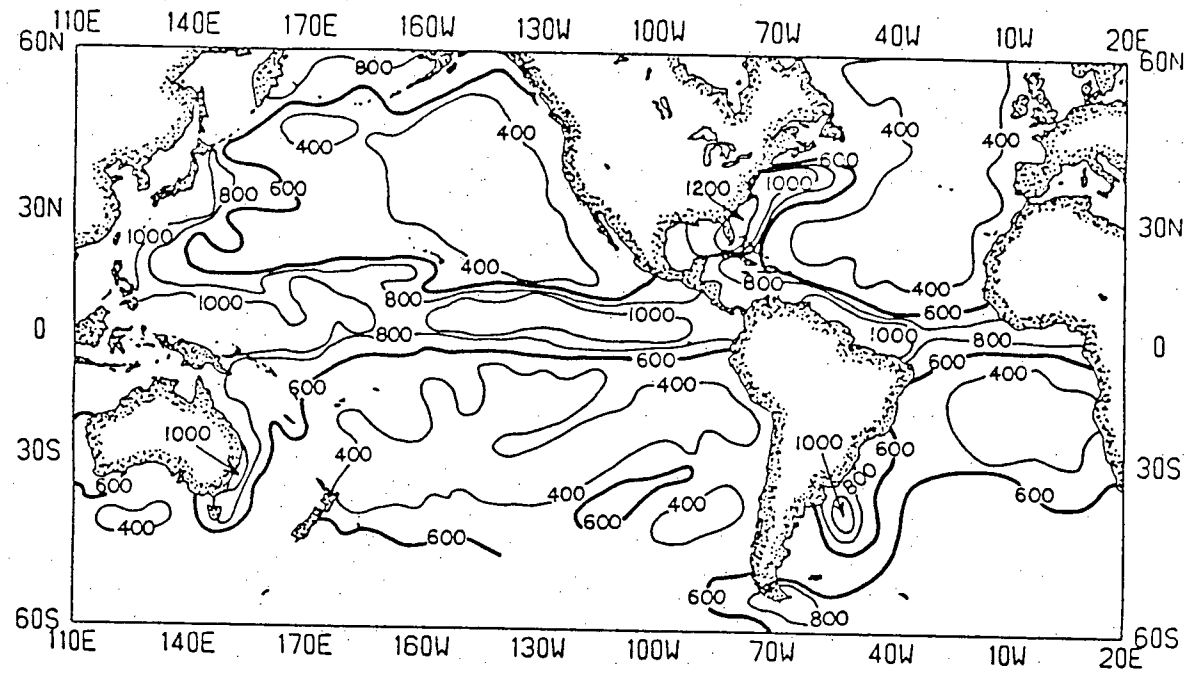

Figure III-3 Eddy kinetic energy (cm^2/s^2) obtained from the NODC historical ship drift file.

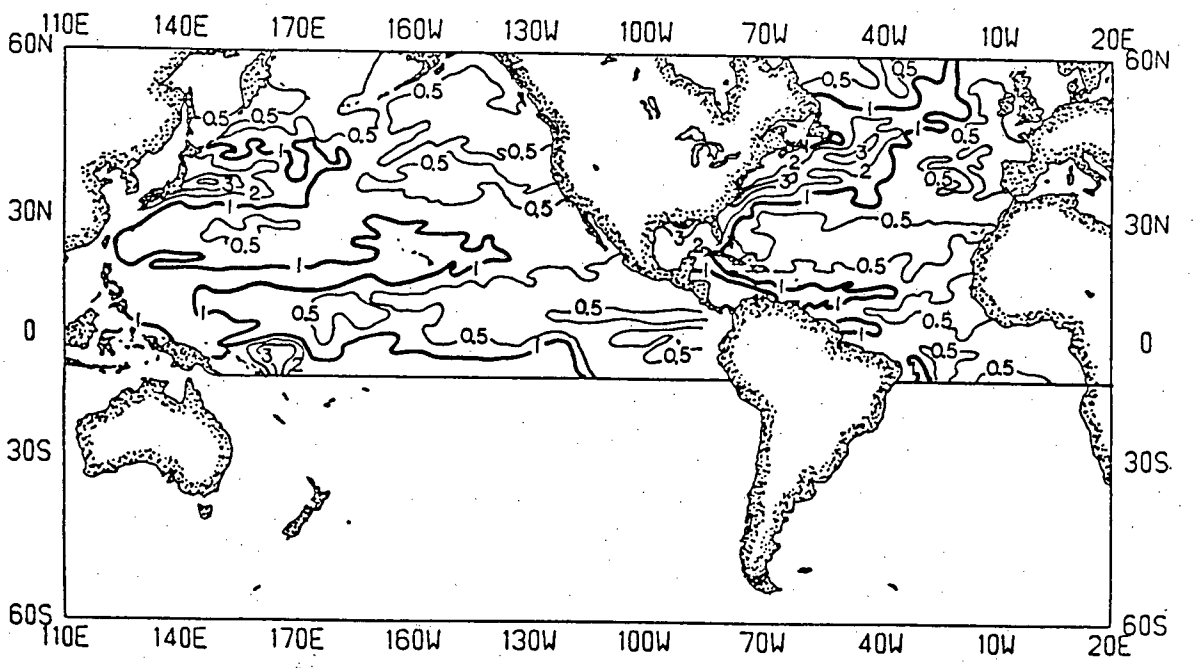

Figure III-4 Standard deviation of temperature at 260 m based on a variable grid analysis of the NODC XBT file north of 10°S.

The ship drift data provide eddy kinetic energies two to four times greater for the equatorial regions, than the relative comparison of the SEASAT EKEs. The relatively higher eddy energies reported by Wyrtki et al. (1976) in the equatorial regions are due to the seasonal variability of the equatorial current and trade wind systems, and the high-frequency (i.e. periods on the order of days and weeks) signal of the winds. The significant seasonal variability of the meridional position and magnitude of these currents and winds (Wyrtki et al., 1981) will induce an "apparent" eddy signal into the ship drift data that will not be apparent in the 24-day record of the SEASAT altimetry data. It should be noted, that the high-energy regions associated with the western boundary currents, as delineated with the ship drift data (Figure III-3), are spatially smaller than the high-energy regions delineated with the SEASAT altimetry (Figure III-1).

The standard deviation of temperature at 260 m for the North Pacific and North Atlantic (Figure III-4) represents the mid-thermocline temperature variability which can be related to the baroclinic mesoscale activity (Emery, 1983a). The temperature variability corresponds to the EPE of the baroclinic signal at 260 m. The high- and low-energy areas in Figure III-2 can be approximated by the 1.0°C contour of Figure III-4. The NWA and NWP have maximum standard deviations of over 3.0 and 4.0°C, respectively, while the NEA and NEP have minimum values less than 0.5°C. The temperature deviation map shows high values in the equatorial regions which are relatively smaller than those of the ship drift data (Figure III-3), but relatively greater than those of the SEASAT altimetry (Figure III-4). This is consistent with the limitations of each data set for examining the eddy variability on a global scale. The EKEs of Wyrtki et al. (1976) are overestimated due to the winds. The SEASAT altimetry will underestimate the eddy variability due to the short data record of 24 days. The temperature variability will not be biased by either the surface winds nor the length of the data record, however, it will miss an important part of the barotropic variability.

In summary, the ship drift data, the SEASAT altimetry, and the temperature deviations are three different representations of the global eddy variability. Wyrtki et al. (1976) estimated the EKEs with the ship drift data. The SEASAT altimetry (Cheney et al., 1983) represents the EPE of the barotropic eddy variability, and the temperature deviations (Emery, 1983a) correspond to the EPE of the baroclinic signal. The limitations of each have been discussed.

The temperature deviation maps of Emery (1983a) are the most appropriate for comparison with the results of this investigation, with the exception that these maps provide no coverage south of 10°S. The following discussion will examine typical quasi-synoptic sections and maps of the temperature structure for each geographic region and compare them with results of the above analyses.

Northwest Atlantic

The Northwest Atlantic region, defined in Figure III-2, is a region of high eddy activity. The intensity of the eddy field increases as one approaches the Gulf Stream (Figure III-5). The mean circulation of the region is dominated by the Gulf Stream System (Fofonoff, 1981), consisting of the Florida Current, the Gulf Stream and the North Atlantic Drift. Characteristic mesoscale features include Gulf Stream meanders and the resulting warm- and cold-core rings in the continental slope waters and Sargasso Sea, respectively. Approximately ten cold-core rings co-exist in the Sargasso Sea at a single time (Richardson, 1983). Five to eight cold-core rings form per year with diameters of approximately 200 km and raised isotherms in their centers of up to 600 m. The warm-core anticyclonic rings form in a triangular region bounded by the continental slope on the north and the Gulf Stream on the south (Saunders, 1971). The largest rings, 200 to 300 km in diameter form to the east of Georges Bank, however smaller rings (100 km) form to the west. Typically, five warm rings form per year with average diameters smaller than that of the cold rings (Lai and Richardson, 1977). Approximately three warm-core rings exist at a single time (Richardson, 1983).

Twenty-three sections were obtained for the NWA. The SXBT data collected by the HMCS Preserver across the North Atlantic in October 1982 (Figure III-6) exhibit the salient mesoscale features of the NWA. Figure III-6a shows the SXBT locations. The Gulf Stream, a warm-core ring, a cold-core ring and several smaller cold eddies in the Sargasso Sea can be clearly seen in Figure III-6b. The Gulf Stream at 55°W separates a warm ring at 57°W and a cold ring at 51°W. The warm ring has a width of 350 km with a depression of the 10°C isotherm of about 200 m. The cold ring has a width of 450 km with an elevation of the 14°C isotherm of about 300 m. Between 47°W and 32°W (Figure III-6b) there are three smaller eddies with widths of 250 to 300 km. The upward deflections of the 15°C isotherm are 200 m and 175 m for the eddies at 45°W and

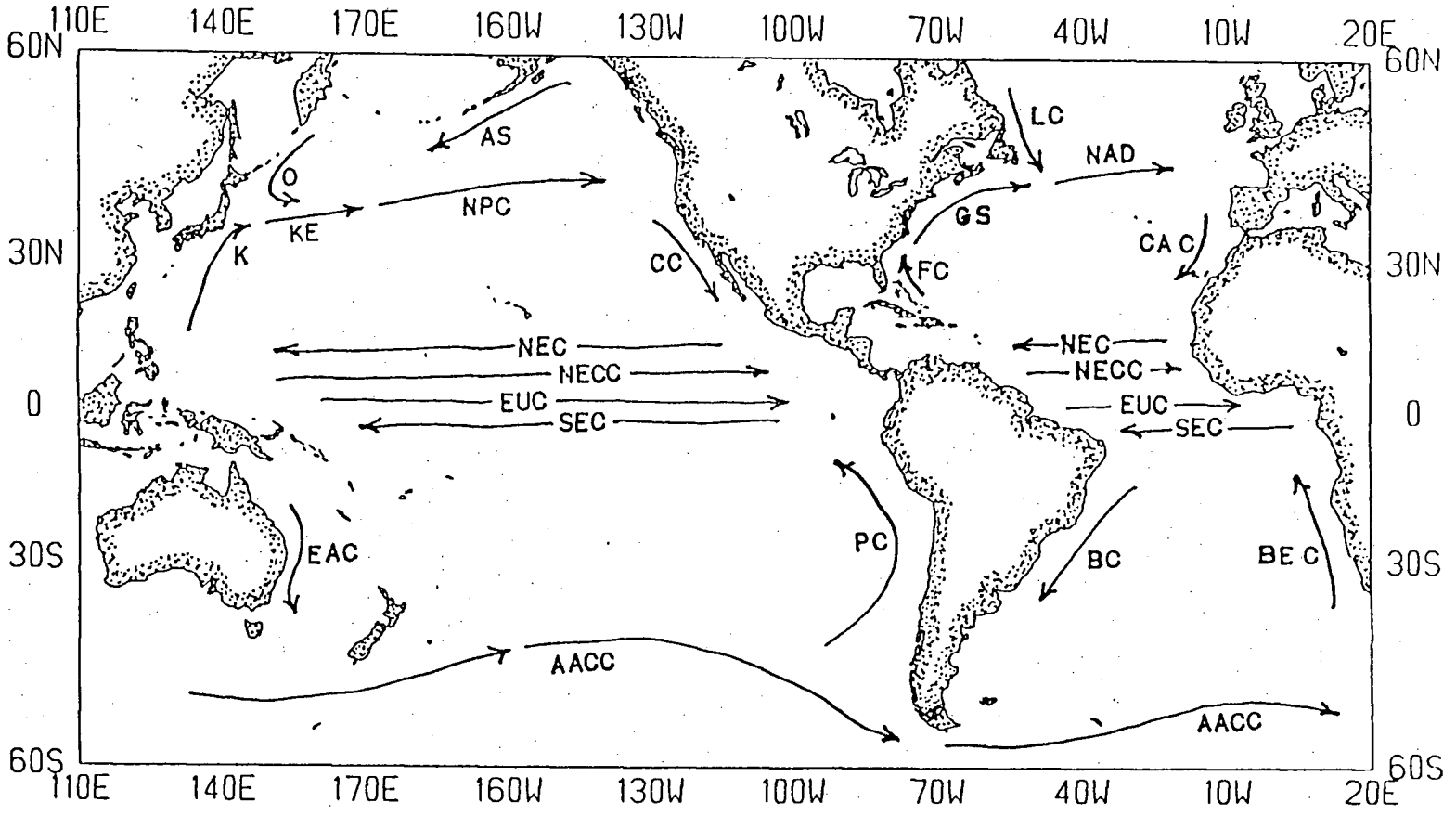

O	-	Oyashio	NECC	-	North Equatorial Countercurrent	LC	-	Labrador Current
K	-	Kuroshio	EUC	-	Equatorial Undercurrent	NAD	-	North Atlantic Drift
KE	-	Kuroshio Extension	SEC	-	South Equatorial Current	GS	-	Gulf Stream
AS	-	Alaskan Stream	EAC	-	East Australian Current	FC	-	Florida Current
NPC	-	North Pacific Current	PC	-	Peru Current	BC	-	Brazil Current
CC	-	California Current	AACC	-	Antarctic Circumpolar Current	BEC	-	Benguela Current
NEC	-	North Equatorial Current						

Figure III-5 Surface currents of the Pacific and Atlantic Oceans.

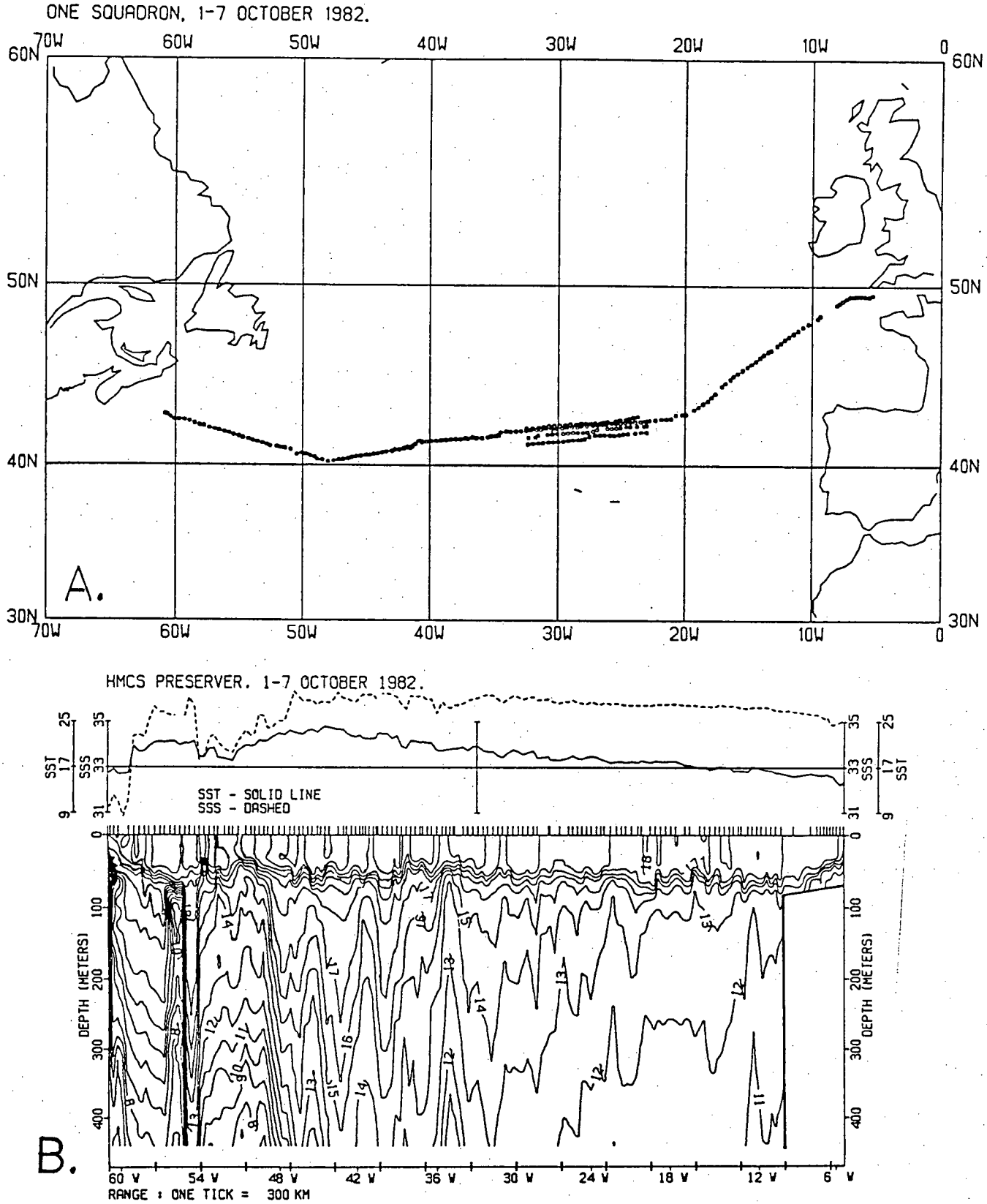

Figure III-6 **SXBT section (PE-071082) collected by the HMCS Preserver, in October 1982 across the North Atlantic.**

a. SXBT locations.

b. Temperature (°C) section.

41°W, respectively. The eddy at 34°W has a 275 m deflection of the 14°C isotherm. A further sample section, obtained from the USN multiship survey in December 1976 (Figure III-7) (east of the Gulf Stream ring concentrations) at 33°N, shows three cold eddies at 52°W, 38°W and 32°W. These eddies have widths of 450, 400 and 350 km, respectively, with vertical deflections of the 17°C isotherm of 200 m.

Six surveys were obtained for the NWA region. Four of these are the multiship USN surveys examined by Emery et al. (1980) for the fraction of vertical isotherm deflections associated with closed eddies. Seventeen closed eddies were identified west of 30°W with mean diameters of 150 km. These investigators noted that about one-half of the eddies were Gulf Stream rings. Individual maps of these surveys will not be examined here in light of this detailed work. It will suffice to say that the individual sections obtained from these surveys, and the surveys as a whole, exhibit the characteristic mesoscale structure of the NWA.

The two multiship surveys collected by the CAF, southeast of Newfoundland, are in Figure III-8. Both surveys show the strong subsurface thermal front of the Labrador Current meeting the North Atlantic Drift. In the October 1981 survey (Figure III-8a), the front has a northeast-southwest alignment. With a survey width of 110 km, it is not surprising that no closed eddies can be identified. The front retains its general northeast-southwest alignment in the June 1983 survey (Figure III-8b), with the addition of an eastward cold water excursion of about 150 km. There are also alternating near-meridional bands of warm and cold water to the east of the front. Again, the limited width of the survey (200 km) does not permit the horizontal structure of these features to be resolved any further.

Northwest Pacific

The Northwest Pacific (Figure III-2) is a region of high eddy activity which includes the Kuroshio, the Kuroshio Extension, the Oyashio and the western portion the North Pacific Current. Both the Kuroshio and the Oyashio meander and shed warm- and cold-core rings similar to the Gulf Stream. Recent investigations of historical data in the region (Richardson, 1983) documented the coexistance of 13 cold rings and two warm rings in the summer of 1939, and suggested that the cold rings form at three or four specific sites. A synoptic

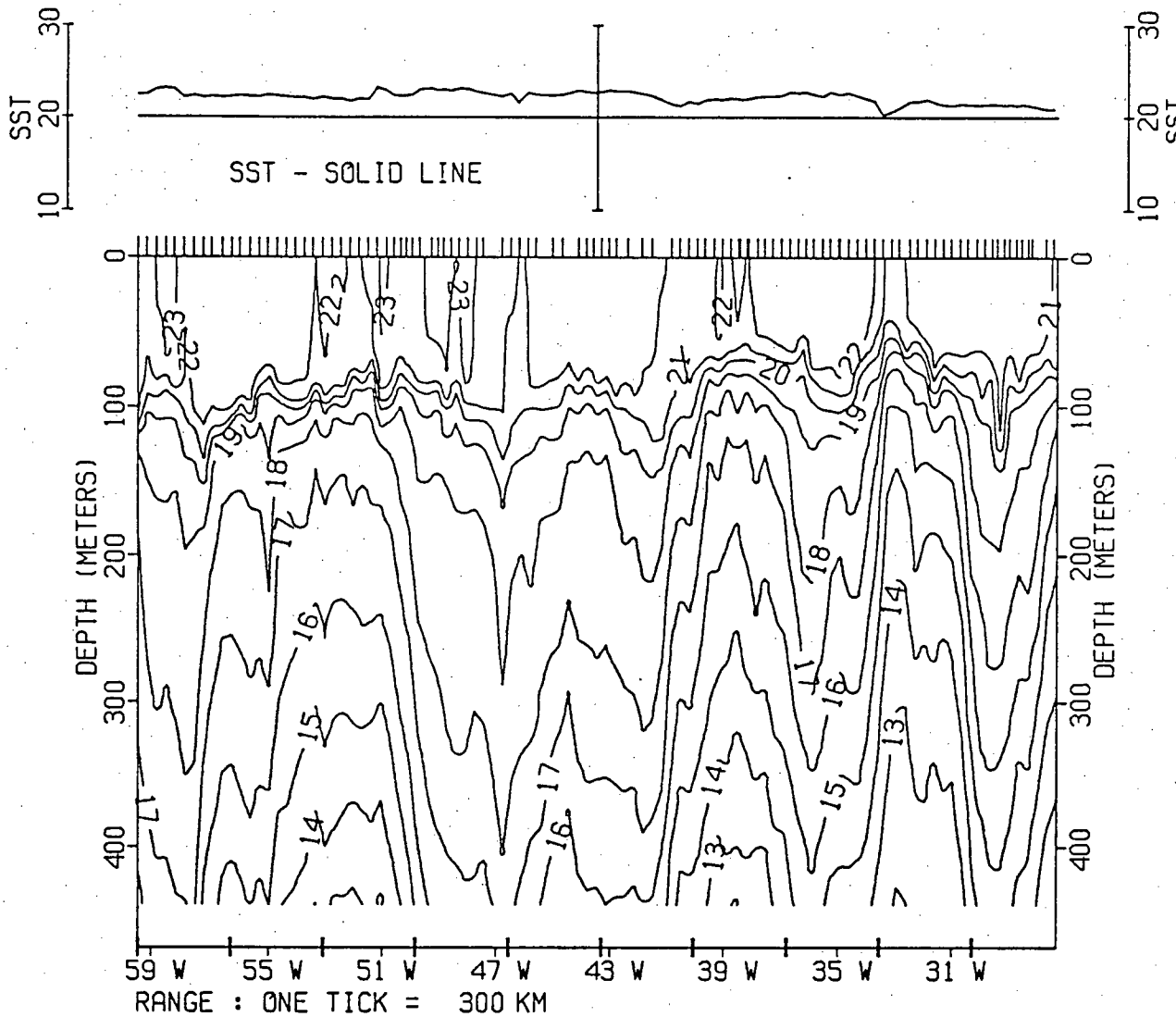

Figure III-7 Temperature (°C) section (72-001276) obtained from the USN multiship survey at 33°N in the NWA.

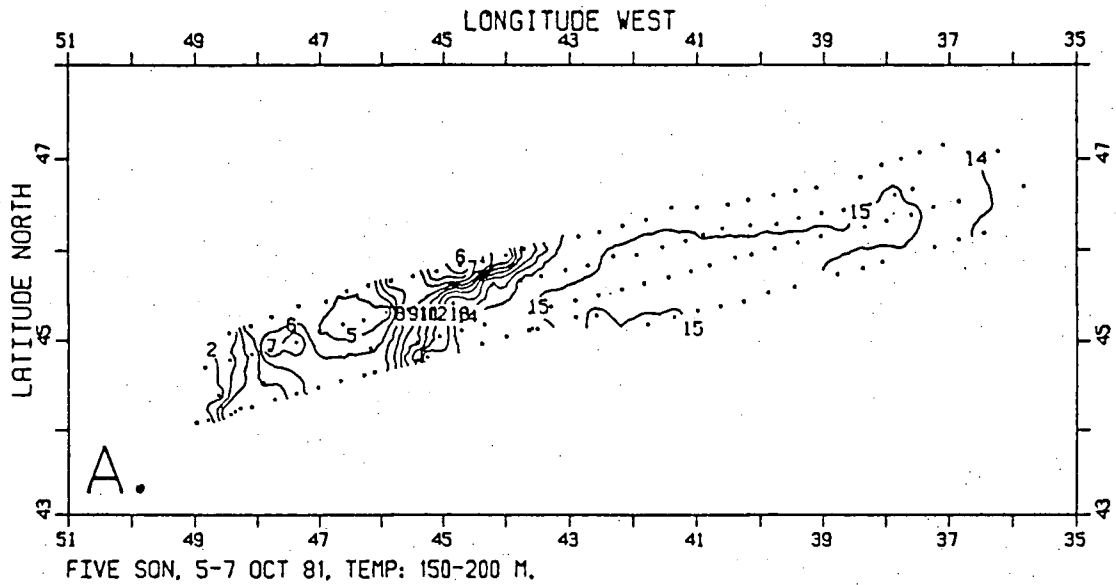

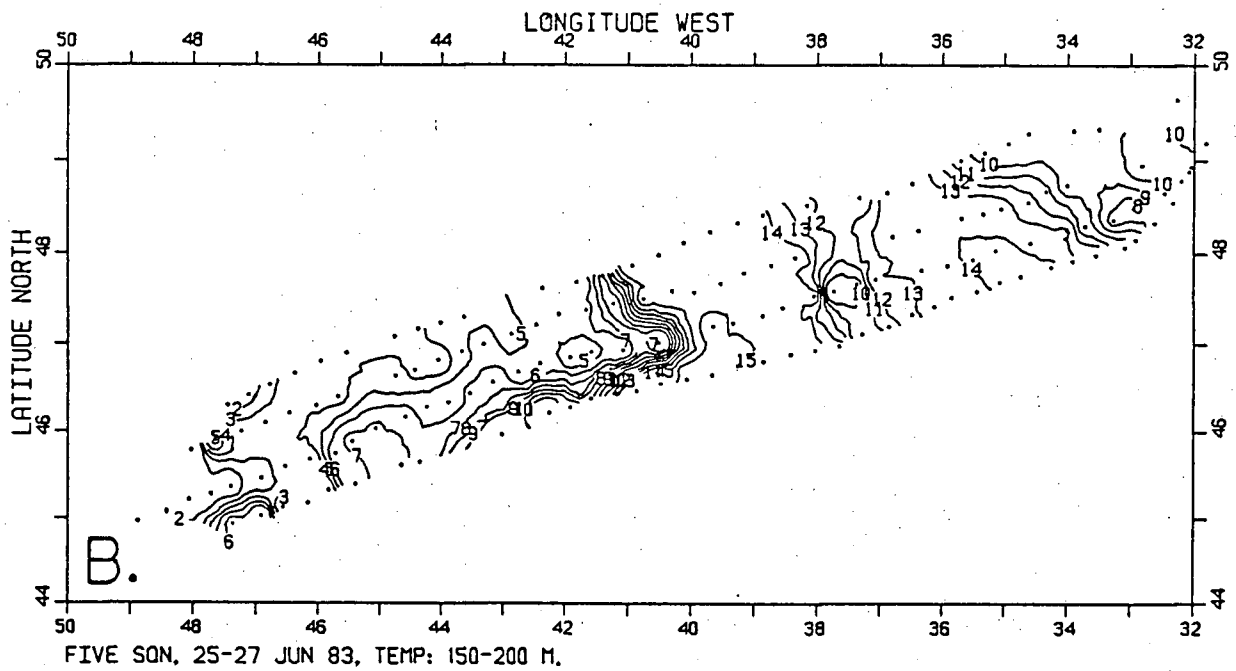

Figure III-8 Maps of temperature (°C) vertically-averaged from 150 to 200 m in the NWA, from multiship surveys collected by the CAF.
a. Survey PE-071081, October 1981.
b. Survey FR-270683, June 1983.

study reported by Cheney (1977) identified three warm and two cold rings. One of the rings had a diameter of 250 km. Kitano (1975) examined 154 warm-core rings from the Kuroshio and the Oyashio and found an average diameter of 140 km.

The XBT data set obtained for the NWP comprises two multiship surveys conducted by the USN (Wilson and Dugan, 1978) and two sections acquired from the NODC. Figure III-9 shows two sample temperature sections in the region (one from each of the USN surveys), eastward of the concentrations of Kuroshio and Oyashio rings. Section 54-000575 (Figure III-9a) was taken at 37.5°N, north of the mean Kuroshio axis (Wilson and Dugan, 1978). Three cold eddies can be identified at 165°E, 172°E and 178°E (presumably from the Oyashio), and one warm eddy at 170°E (presumably from the Kuroshio). These features have widths of 180, 250, 180 and 250 km, respectively, with displacements of the 11°C isotherm of 170, 350, 200 and 300 m. Section 40-001175 was taken south of the mean Kuroshio axis at 31.5°N. Three cold eddies are discernable at 163°E, 172°E and 176°E, with widths of 180, 200 and 280 km, respectively. The deflections of the 14°C isotherm for these features are 220, 170 and 140 m, respectively.

Emery et al. (1980) examined these two USN surveys for the fraction of vertical isotherm deflections associated with closed eddies. Again, the individual maps of these surveys will not be examined here. A total of five closed eddies were identified.

Northeast Atlantic

The Northeast Atlantic is a region of low eddy activity relative to the western boundary current regions. Generally, the mean circulation is weak. The North Atlantic Drift crosses the mid-Atlantic ridge from the west in two branches (Saunders, 1982) north of 45°N and at 35°N (north and south of the Azores) which turn north and south, respectively.

Gould (1983) identifies four distinct areas where mesoscale features can be found. In the first area, perturbations of the southern edge of the polar front are manifested in large isotherm displacements northwest of a line from 40°N 30°W to 50°N 20°W. The meanderings of the polar front (Gould, 1983) have typical radii on the order of 100 to 150 km with large geopotential anomaly

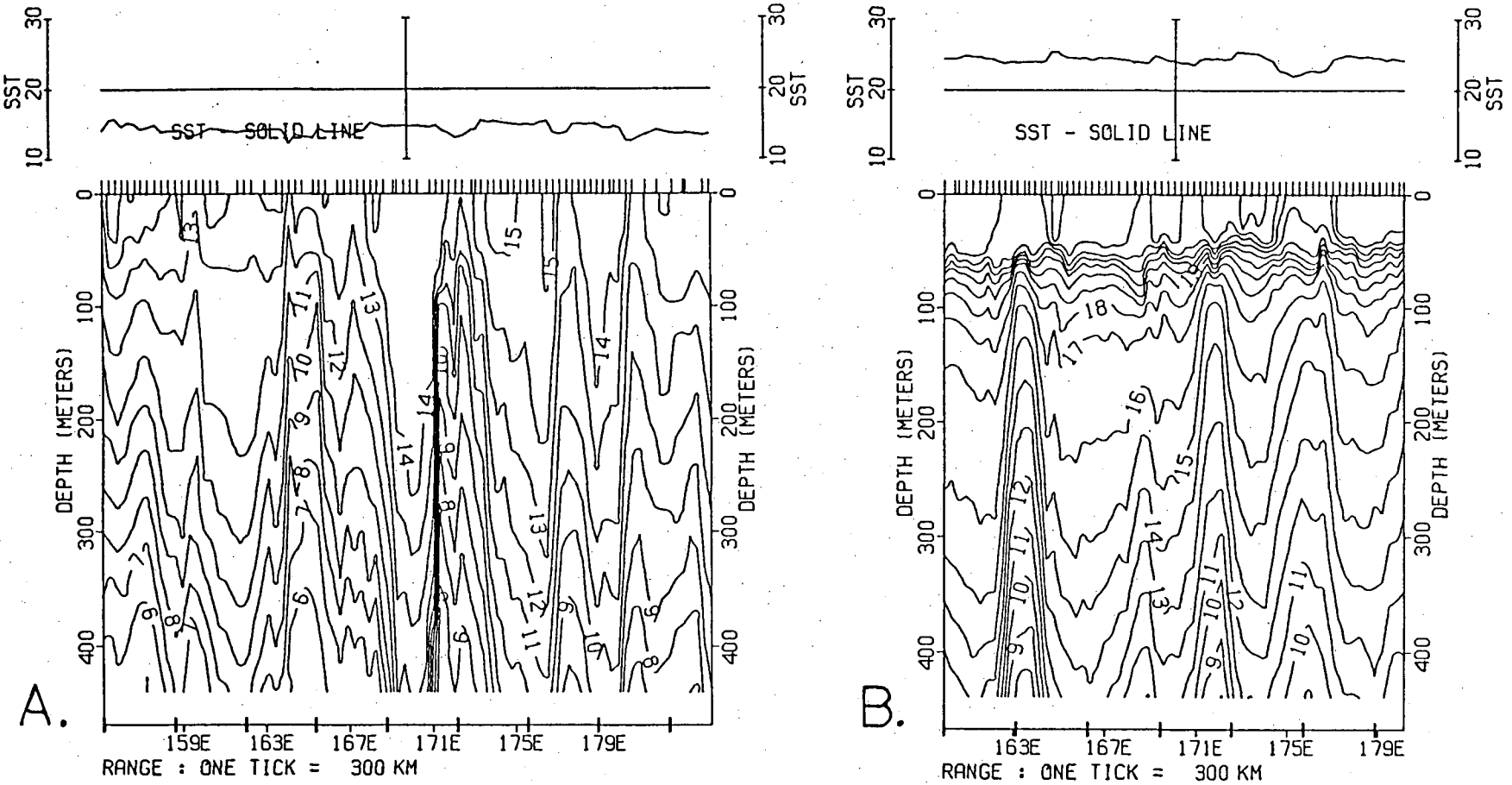

Figure III-9 **Temperature (°C) sections from the USN multiship surveys in the NWP.**

a. Section 53-000575 at 37.5°N.

b. Section 40-001175 at 31.5°N.

fluctuations. Howe and Tait (1967) examined a cold eddy near 53°N and 19°W, confined to the upper 500 m. This feature was elongated in a north-south direction and measured approximately 200 km by 100 km. It was speculated that this was a pinched off meander of the North Atlantic Drift. The second area is above and to the east of the mid-Atlantic ridge, just southwest of the Azores. Intense lenses of Mediterranean water have been reported with diameters of about 50 km. These eddies are found at depths between 700 and 1200 m and have no thermohaline signature above 500 m. Gould (1983) also reported a cyclonic eddy at 33°N 32°W with a diameter of 100 km. It was observed separating from a frontal feature in the summer of 1981. The third area is in the zonal band of 30°N to 40°N between 12°W and 20°W. The eddy variability is rather poorly defined, but Gould suggests that it may reflect the influence of the Mediterranean outflow. A fourth area, east of a line from the UK to the Azores, appears to have very little mesoscale activity.

The XBT data set obtained for the NEA consists of 16 sections and four surveys. Figure III-6b and Figure III-10 are the trans-oceanic sections for the CAF cruises in October 1982 and October 1981, respectively. Both sections illustrate the reduced mesoscale activity of the NEA, east of about 30°W. Figure III-6b also provides a realization of the mesoscale structure in two of the four areas observed above. Between 32°W and 20°W, the temperature structure has numerous perturbations between 100 to 200 km in width, with isotherm deflections of about 100 m, characteristic of the area northwest of the Azores. East of 20°W, the structure is relatively quiescent. The CAF survey conducted northwest of the Azores (Figure III-11) shows a warm eddy at 30°W with a diameter of 100 km. From the temperature section in Figure III-6, the eddy can be seen to be confined to the upper 500 m of the water column and have a maximum isotherm (14°C) deflection of about 40 m.

Three of the North Atlantic USN surveys extend sufficiently eastward to be included in an examination of the NEA. Survey 64-000776 is north of the Azores, while 93-000577 and 21-001077 are south of the Azores. West of 35°W Emery et al. (1980) found no closed eddies, although vertical isotherm deflections similar to those of Figure III-6b can be found in all the sections taken from these surveys.

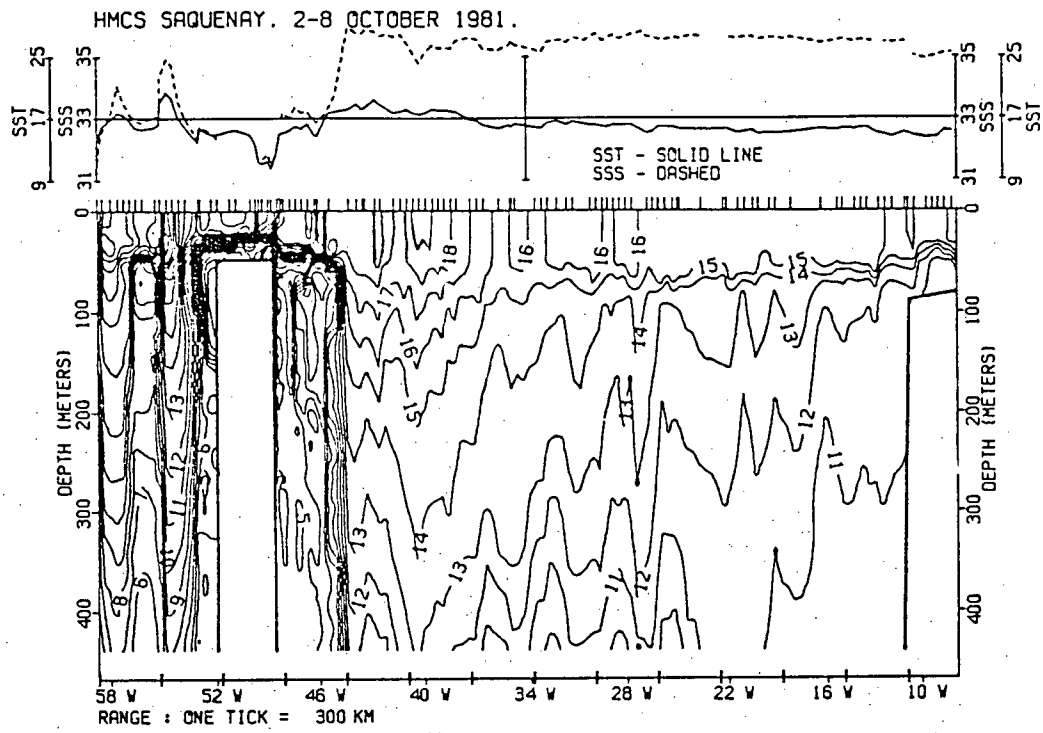

Figure III-10 Temperature (°C) section (SY-051081) collected by the HMCS Saguenay (CAF) across the North Atlantic in October 1981.

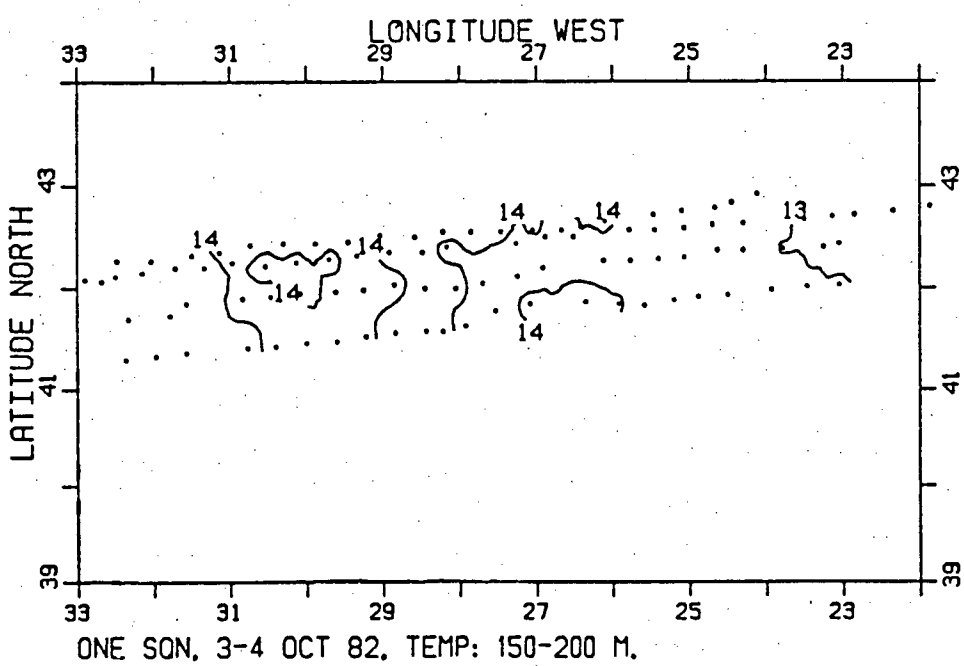

Figure III-11 Map of vertically-averaged temperature (°C) from 150 to 200 m in the NEA obtained by the CAF, October 1982 (ME-041082).

South Atlantic

The South Atlantic region, defined in Figure III-2, has relatively little mesoscale eddy activity. It is a low in the maps of both the eddy kinetic energy (Figure III-3) and the standard deviation of SEASAT altimetry (Figure III-1). The region is bounded by the South Atlantic Equatorial Current, the Brazil Current, the Antarctic Circumpolar Current and the Benguela Current. There have been virtually no observational studies of the eddy variability of the region.

The data set acquired for the SA consists of two zonal sections from NODC (Figure III-12). The station spacings are about 100 km, so eddies smaller than 200 km in width cannot be resolved. Section 40-190283 was taken in February 1983 at 24°S. Several mesoscale features are discernable: a warm eddy at 27°W, a cold eddy at 20°W and an eddy at 5°W, with a cold core above 200 m and a warm core below 200 m. The features have widths of 400, 400 and 200 km, respectively, with vertical deflections of the 15°C isotherm of 25, 25 and 50 m. Section 04-310383, taken at 12°S, has cold eddies at 34°W and 2°E. Their widths are 300 and 500 km, respectively, with deflections of the 12° isotherm of 40 and 75 m.

Northeast Pacific

The Northeast Pacific region has been defined as the low eddy activity region of the subtropical and subpolar gyres, bounded in the north by the Alaskan Stream and in the south by the North Equatorial Countercurrent. Bernstein (1983) provided a review of the eddy variability of the NEP and described a general increase in the mesoscale activity as one proceeded toward the tropics. This is consistent with the zonal band of higher eddy activity shown in the deviations of SEASAT altimetry (Figure III-1) between 5°N and 25°N. Royer (1978), in a meridional hydrographic section, found the eddies to be few in number and weak between 54°N and 34°N. Their typical amplitudes were 5 dyn-cm with widths of about 40 km. Between 34°N and 22°N the eddies were more numerous with typical amplitudes of 10 to 15 dyn-cm and widths of 150 to 200 km. Roden (1980) found eddies north and south of the subtropical front, north of Hawaii at 30°N. Bernstein and White (1974) analysed a data set near Hawaii south of the subtropical front at 25°N. Eddies appeared regularly in the data with average isotherm perturbations of about 40 m and diameters of

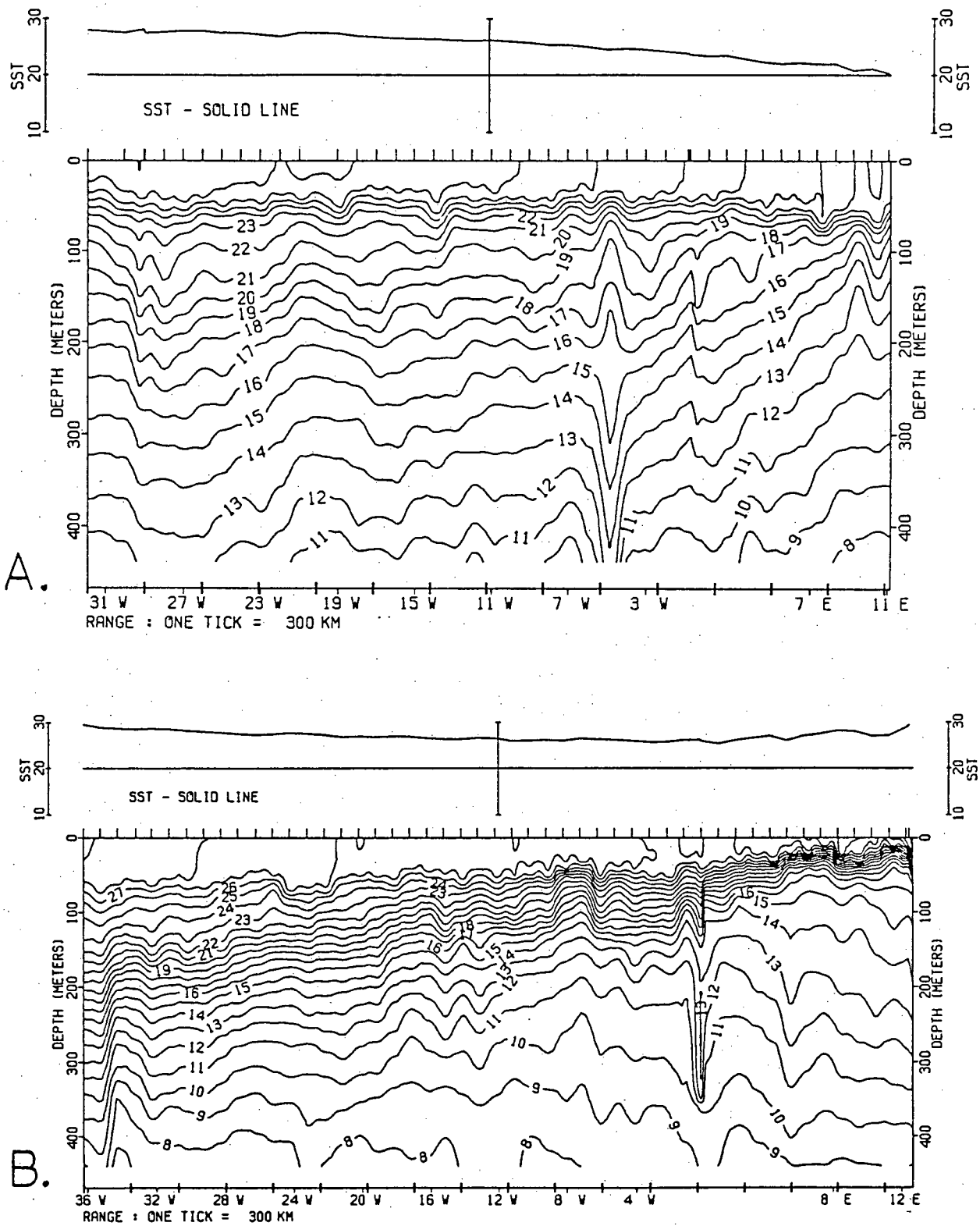

Figure III-12 Temperature (°C) sections from the NODC in the SA.
a. Section 40-190283, February 1983.
b. Section 04-310383, March 1983.

200 km. The Hawaii to Tahiti Shuttle Experiment (Wyrtki et al. 1981; Wyrtki, 1982) identified two types of eddies drifting westward with the North Equatorial Current. The first type appeared at 158°W near 20°N, south of Oahu, on nine of the 26 sections and was extensively studied by Patzert (1969). These cold eddies were formed to the west of the island of Hawaii and had widths on the order of 200 km with vertical displacements of the 14°C isotherm of about 60 m. The second type appeared in the North Equatorial Current between 14°N and 19°N. There were cold eddies present in the meridional sections between 150°W and 158°W, 50% of the time. These eddies ranged in width from 150 to 350 km with perturbations in the 14°C isotherm of 40 to 65 m in amplitude. Wyrtki found no obvious relationship between eddy diameters and amplitudes. Immediately south, is the North Equatorial Countercurrent, a strong seasonally varying eastward current. Legeckis (1977) discovered meanders occurring when the current flow is strongest, in September to January, with zonal wavelengths of 1000 km and north-south amplitudes of 100 km.

The data obtained for the NEP consist of 37 sections (six from the CAF and 32 from the NODC), and 16 surveys. Figure III-13 is a typical section taken by the CAF (from Hawaii to Vancouver Island) that illustrates the difference in the mesoscale structure on either side of the North Pacific Subtropical Front at 35°N. Climatologically, the subtropical front is defined as the northern limit of the North Pacific Central Water, which has wintertime temperatures greater than 18°C and salinities greater than 34.8×10^{-3}. South of the front, three cold eddies can be identified at 22°N, 25°N and 34°N. Their widths are 200, 350 and 150 km, respectively, with vertical displacements of the 11°C isotherm of 30 m. North of 35°N, the thermal structure is relatively quiescent.

The SXBT section collected by the CAF in November 1982 (Figure III-14) exhibits the temperature pattern characteristic of the Pacific equatorial current system at 165°W. The 14°C isotherm is in the lower portion of the thermocline and reflects the geostrophic slope associated with the North Equatorial Current (NEC) north of 9°N, the North Equatorial Countercurrent (NECC) between 4° and 9°N, and the South Equatorial Current (SEC) south of 4°N. Imbedded in the SEC, the Equatorial Undercurrent (EUC) is marked by a spreading of the isotherms at 175 m between 2°S and 2°N. The South Equatorial Countercurrent (SECC), also imbedded in the SEC, is a relatively weak eastward flowing current between 11°S and 8°S. A cold eddy can be identified in the NEC

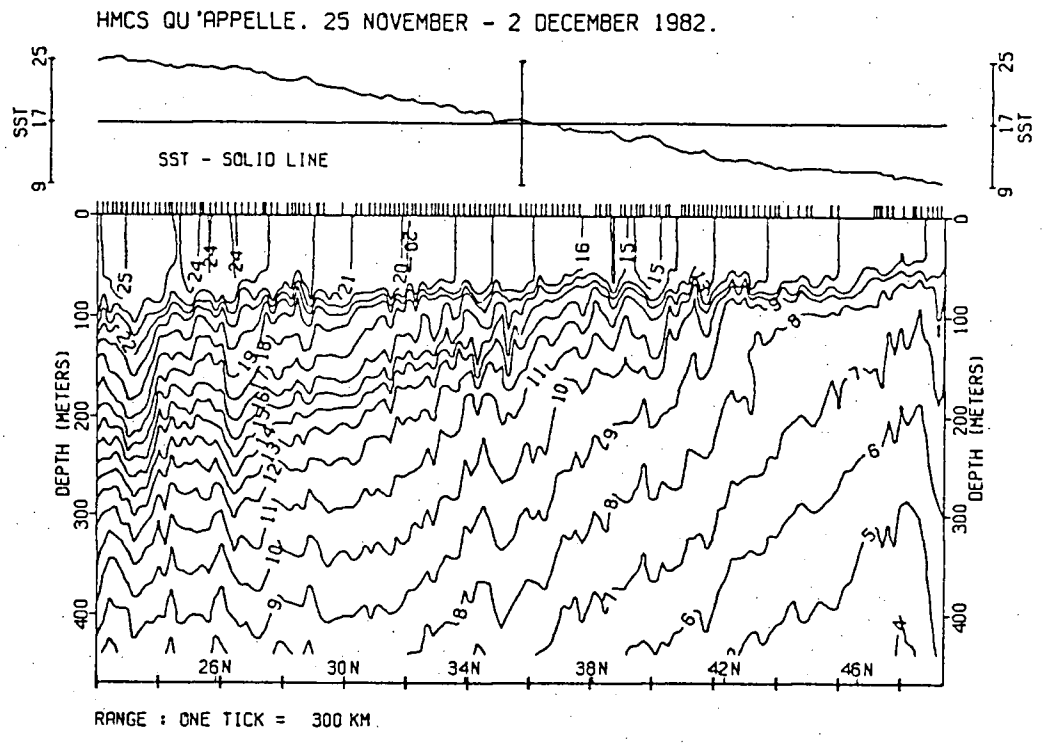

Figure III-13 Temperature (°C) section (QE-251182) collected by the HMCS Qu'Appelle (CAF) in the NEP, from Hawaii to Vancouver Island in November 1982.

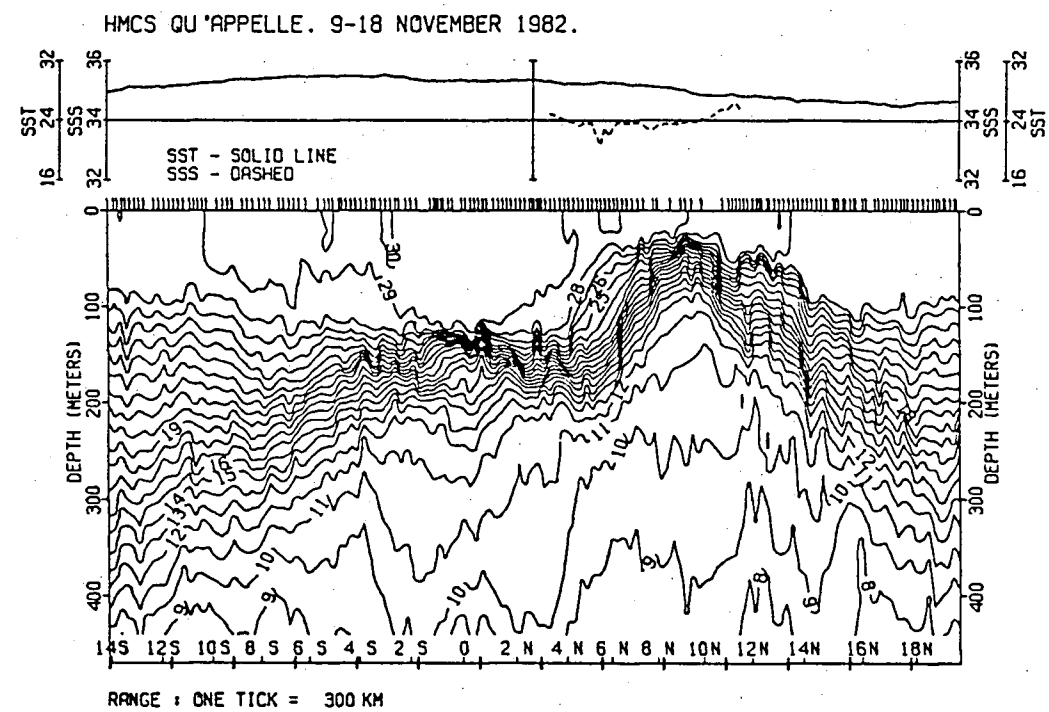

Figure III-14 Temperature (°C) section collected by the HMCS Qu'Appelle (CAF) from Samoa to Hawaii in the central equatorial Pacific, November, 1982. Only the portion of this section north of 4°N has been retained (QE-151182) for the XBT data set summarized in Table A-4.

in Figure III-14 with characteristics very similar to eddy "A" discussed by Wyrtki (1982). It has a width of 350 km and a 25 m vertical deflection of the 14°C isotherm. In the Hawaii to Tahiti Shuttle Experiment, two sections almost simultaneously intersected eddy "A". Its width was 350 km and the deflections of the 14°C isotherm were 27 m and 50 m at 150°W and 153°W, respectively. Presumably, the section in Figure III-14 cut through the side of a larger amplitude eddy.

The XBT surveys in the NEP are in the vicinity of the subtropical front north of Hawaii and in the NEC and NECC south of Hawaii. Figure III-15 shows the subsurface temperature maps of the four CAF multiship surveys conducted across the front between February 1980 and May 1982. With the notable exception of the March 1980 survey, no closed eddies could be defined due to the narrow width of the surveys. In March 1980 (Figure III-15b), an anticylonic eddy is clearly defined by the 17°C isotherm at 28.5°N 153°W, south of the front. The along-track and cross-track temperature sections through the eddy are shown in Figure III-16. It has a vertical deflection of the 17°C isotherm of about 60 m and a diameter of 130 km which is consistent with the local internal Rossby deformation radius (Emery et al., 1984) of 45.5 km.

A time series of six AXBT surveys was collected by the USN across the subtropical front north of Hawaii. The temperature maps in Figure III-17 show an active frontal regime. Between 18 December 1979 to 25 January 1980, a meander forms. The northward displacement of the tongue of warm water has an amplitude of about 100 km. On 7 February 1980, this feature is replaced by a "trough" of cold water of the same amplitude.

South of Hawaii a series of four USN AXBT surveys shows another active eddy field in the North Equatorial Current (Figure III-18). On 30 January 1981, a cyclonic eddy is clearly defined at 15°N 156°W with a diameter of about 200 km. Two weeks later (Figure III-18b) the feature has moved westward at a speed of 10 cm/s to the edge of the survey area. Another cyclonic eddy (150 km diameter) has appeared at 15°N 155°W. The 13 March 1981 survey (Figure III-18c) is on average about 3°C warmer than a month earlier. This is a signature of the annual weakening of, and the southward displacement of, the tropical trough that separates the NEC and NECC, south of the survey area. The survey of 16 April 1981 (Figure III-18d) is again, warmer than the survey of a month earlier. A cold eddy can be seen at 14°N 155°W with a diameter of

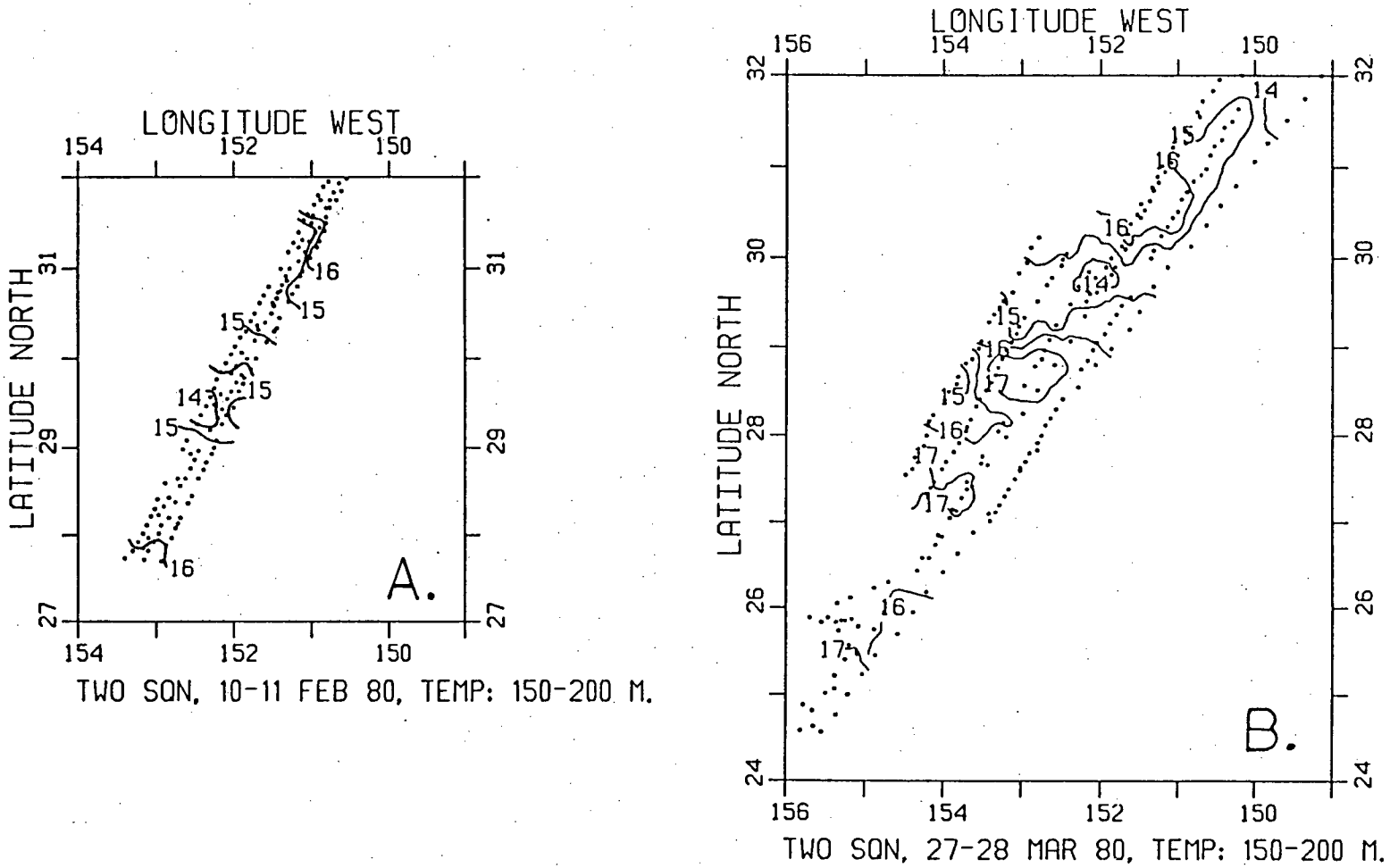

Figure III-15 **CAF multiship surveys of vertically-averaged temperature (°C) from 150 to 200 m taken in the vicinity of the North Pacific Subtropical Front between February 1980 and May 1982.**
a. Survey PR-110280, February 1980.
b. Survey GU-270380, March 1980.

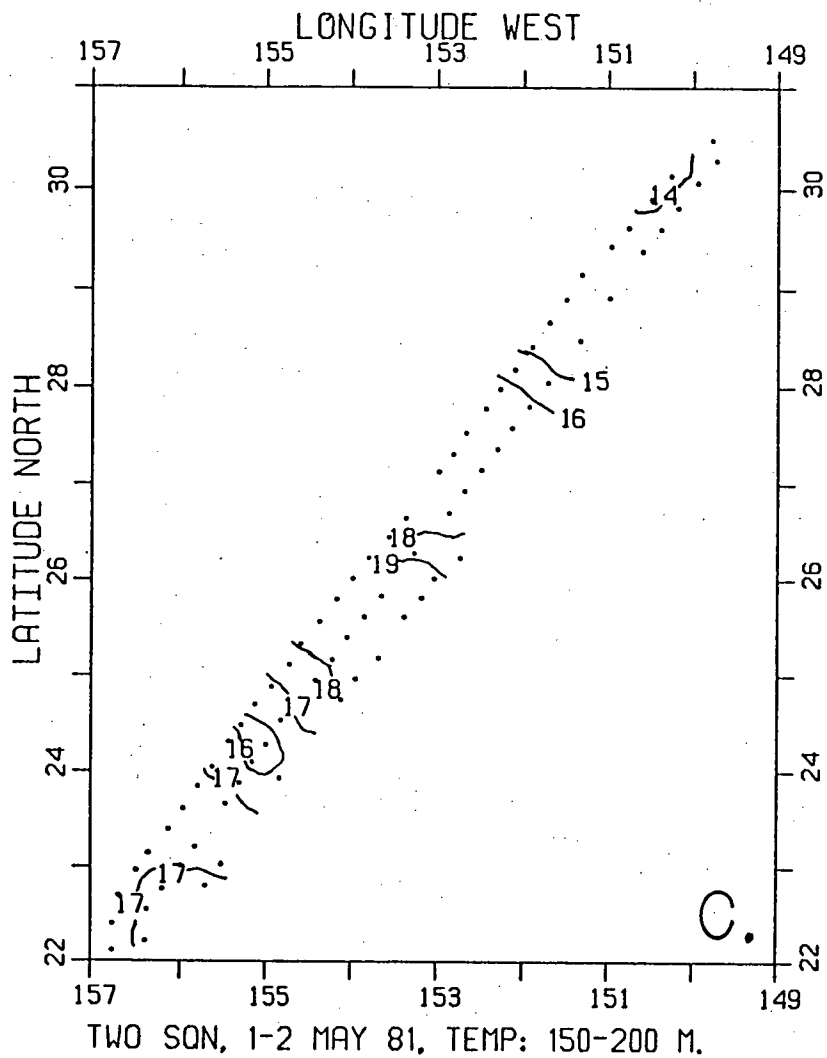

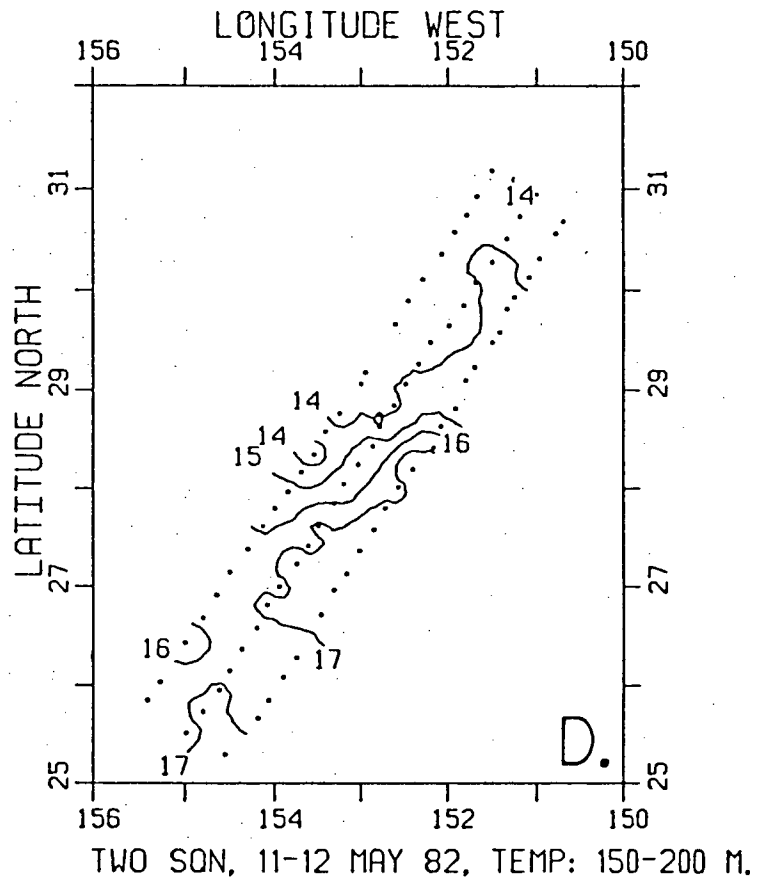

Figure III-15 Continued.

c. Survey PR-010581, May 1981.

d. Survey TA-110582, May 1982.

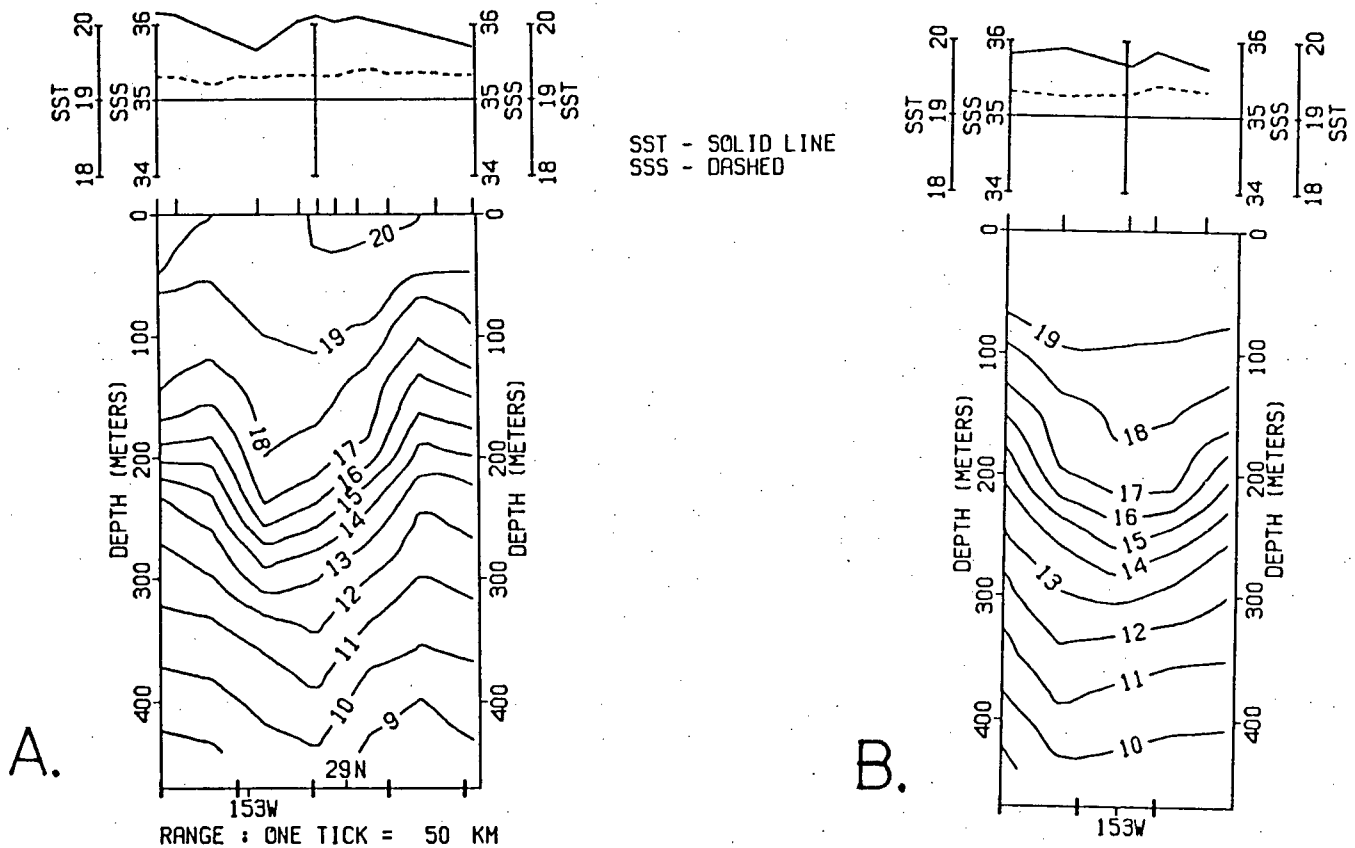

Figure III-16 Detailed temperature (°C) sections of the anticyclonic eddy found in the March 1980 CAF multiship survey (GU-270380) in the NEP (Figure III-15b).

a. Along-track section (southwest to northeast).

b. Cross-track section (northwest to southeast).

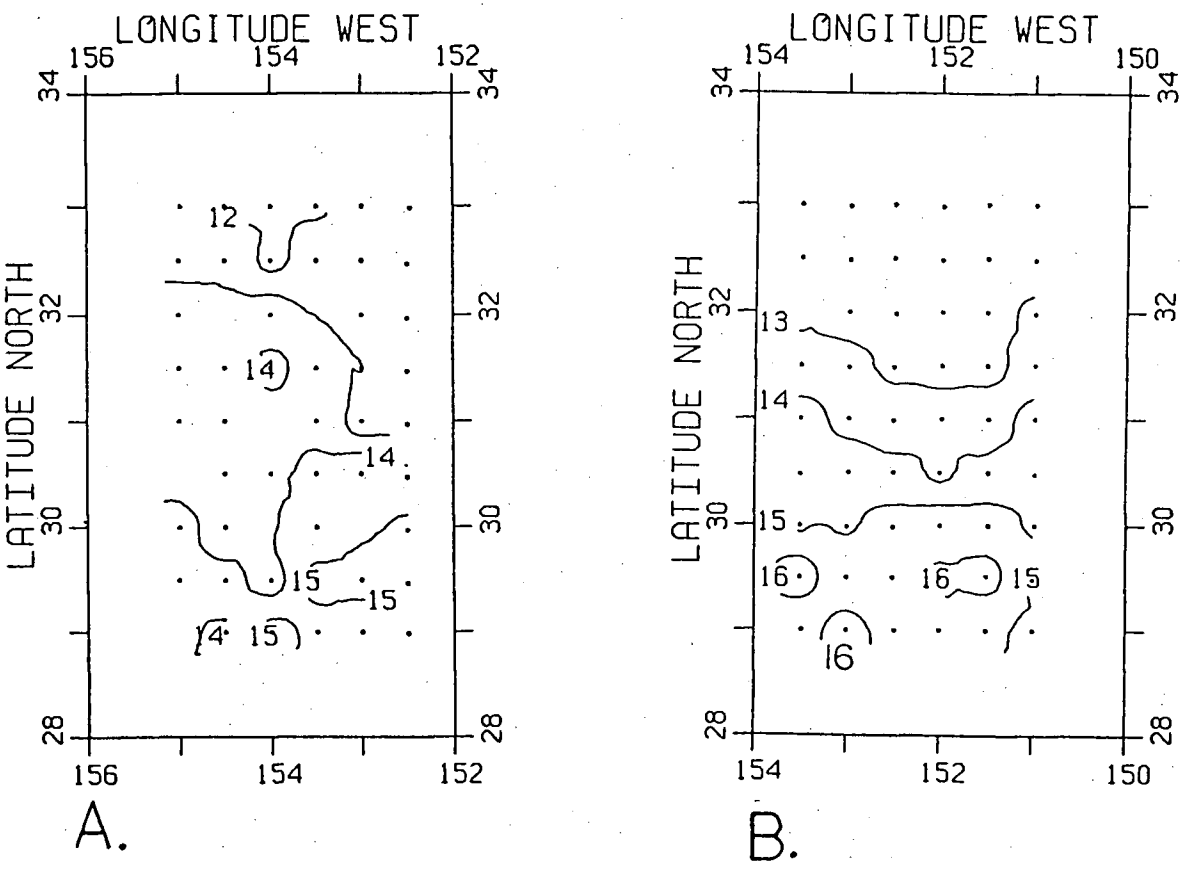

Figure III-17 USN AXBT surveys of vertically-averaged temperature (°C) from 150 to 200 m taken in the vicinity of the North Pacific Subtropical Front between December 1979 and February 1980.
a. Section BB-181279, 18 December 1979.
b. Section CC-211279, 21 December 1979.

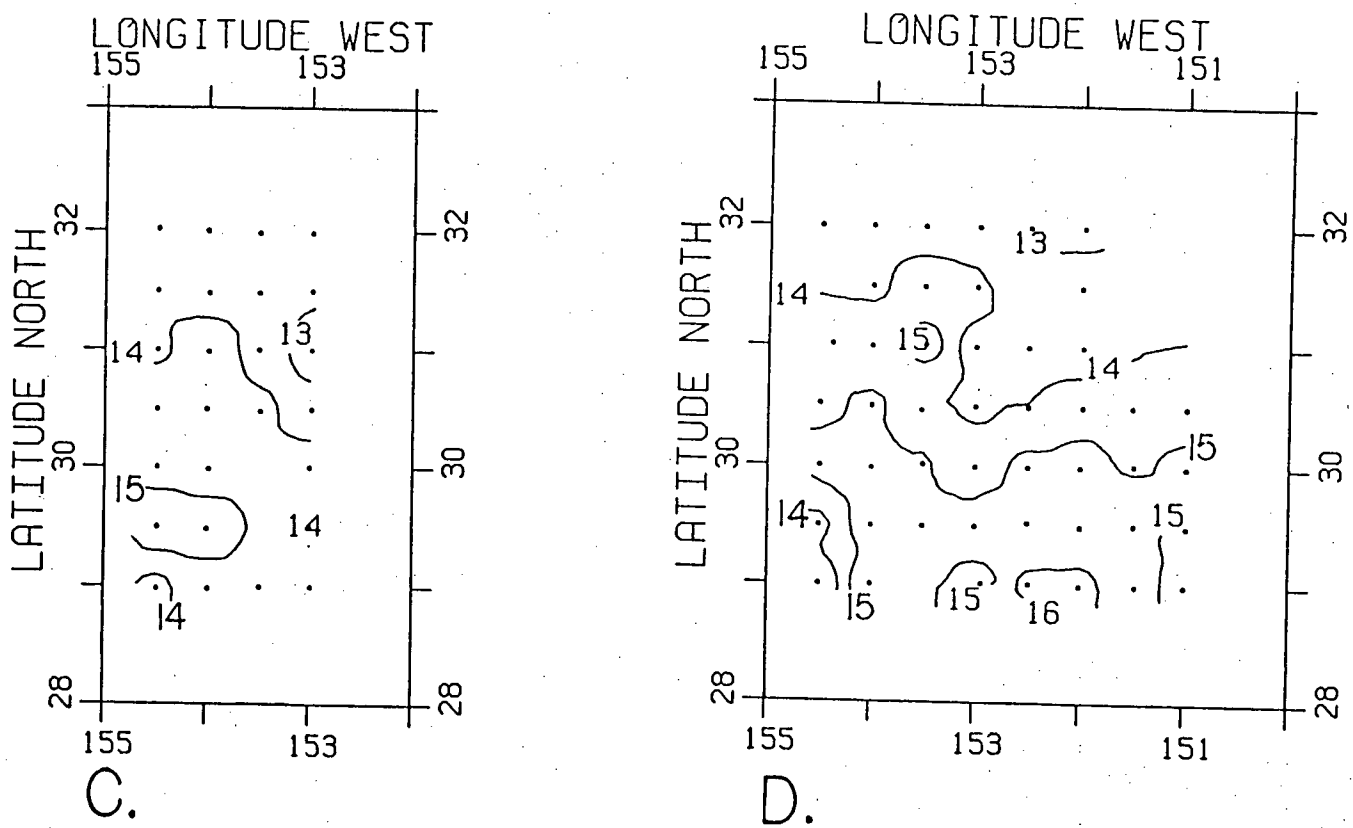

Figure III-17 Continued.

c. Section DD-040180, 4 January 1980.

d. Section EE-170180, 17 January 1980.

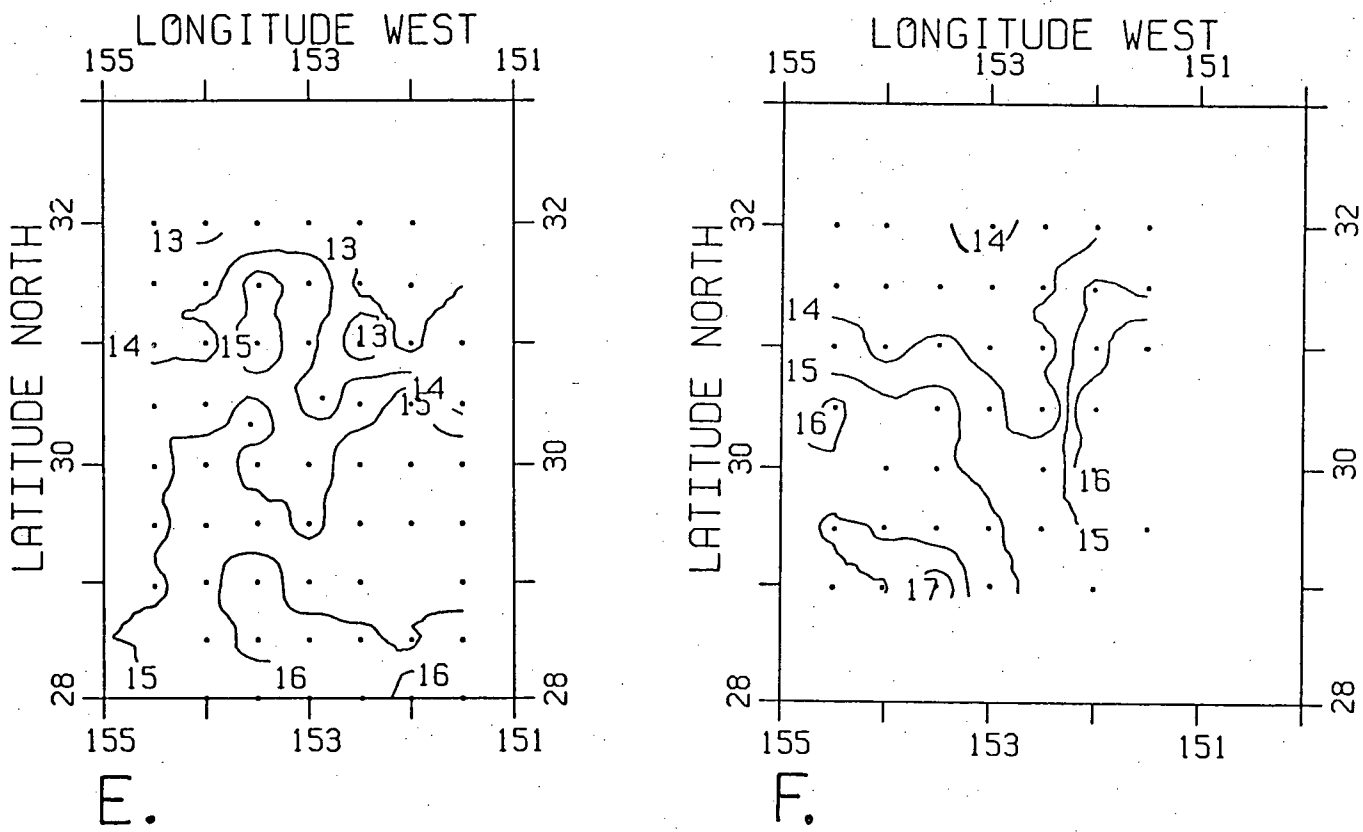

Figure III-17 Continued.

e. Section FF-240180, 24 January 1980.

f. Section GG-060280, 6 February 1980.

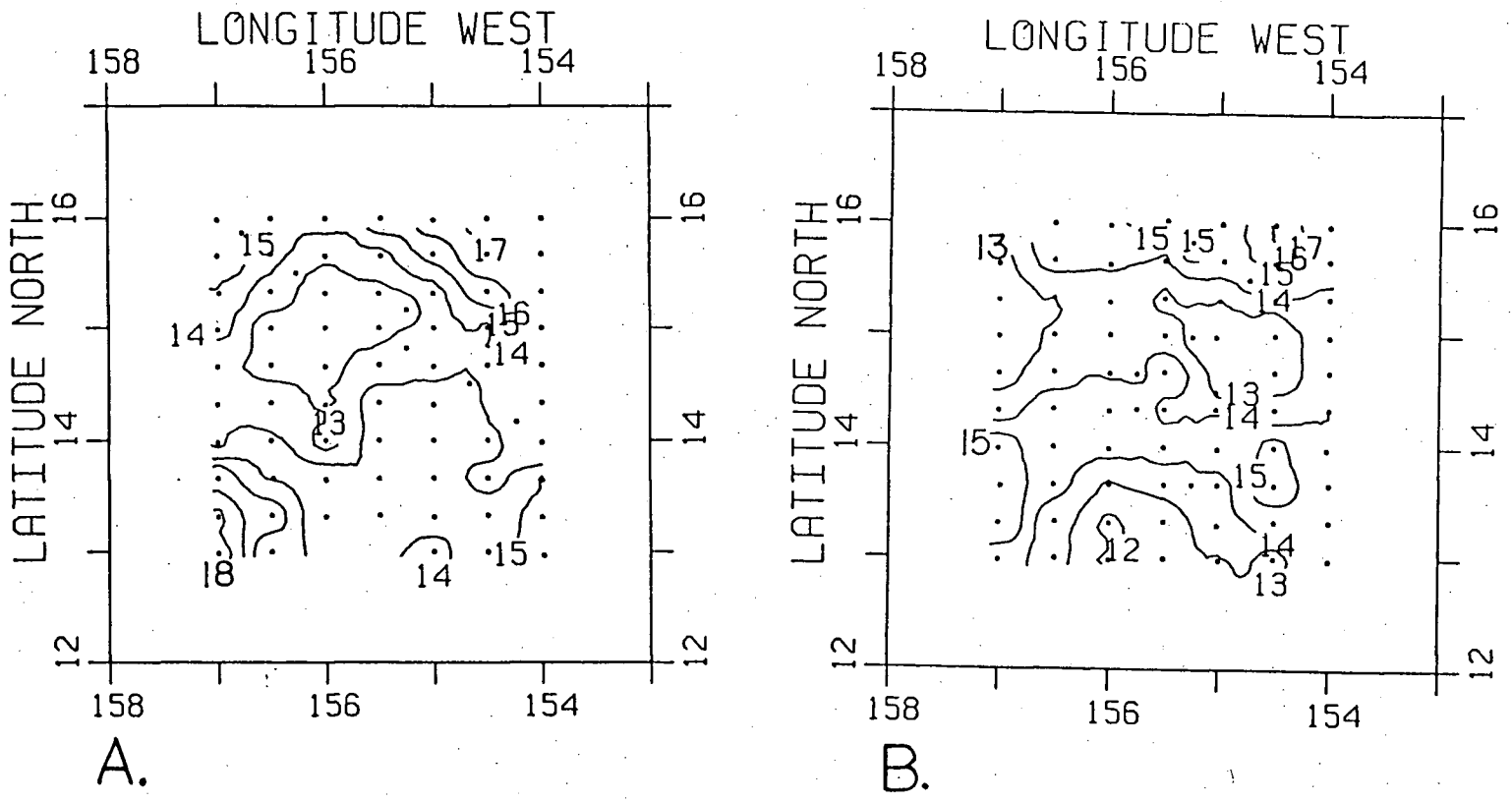

Figure III-18 **USN AXBT surveys of vertically-averaged temperature (°C) from 150 to 200 m taken in the North Pacific Equatorial Current south of Hawaii, between January 1981 and April 1981.**
a. Section BB-300181, 30 January 1981.
b. Section CC-110281, 11 February 1981.

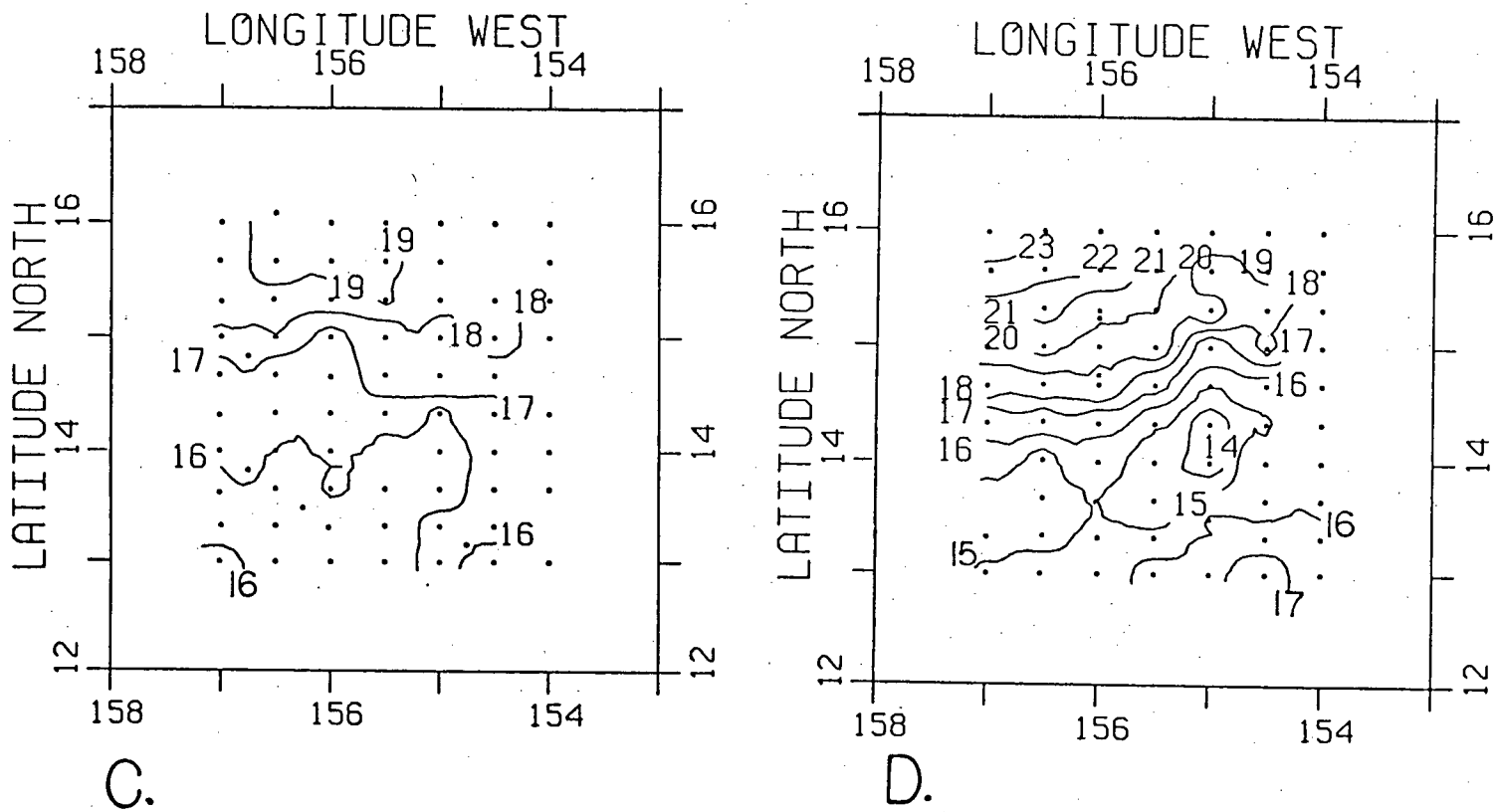

Figure III-18 Continued.
c. Section DD-120381, 12 March 1981.
d. Section EE-150481, 15 April 1981.

approximately 150 km. The intensified meridional temperature gradient north of 14°N is a signature of an increased westward flow, during a period of the annual cycle of the NEC when the flow is generally abating. The presence of the cold eddy during this warming trend may account for the anomalous thermal gradients.

The CAF conducted a multiship survey across the NECC/NEC boundary at 9°N 164°W in November 1982 (Figure III-19). The flow is zonal and the meridional temperature gradient of the NECC dominates the survey. There is no discernible eddy variability.

North of Hawaii, but south of the subtropical front, the USN collected an additional AXBT survey in January 1981 (Figure III-20). A large and distinct southward displacement of the 18°C isotherm with a cold 17°C core can be observed at 25°N 155°W. This feature has a meridional size of 240 km and a zonal width of 120 km, which is consistent with the local internal deformation radius of 53 km (Emery et al., 1984).

South Pacific

The South Pacific region, defined in Figure III-2, is an area of low eddy activity to the north and east of New Zealand, bounded by the South Equatorial Current, the Antarctic Circumpolar Current, and the Peru Current. The extreme paucity of data in this region makes it perhaps the least-surveyed part of the global ocean (Bennett, 1983). The "Scorpio" expedition (Stommel et al., 1973) substantially added to the existing data with its two trans-Pacific transects at 28°S and 43°S, however, the station spacing east of New Zealand could not resolve mesoscale eddies. Patzert and Bernstein (1976) reported on the eddy variability observed in two mesoscale resolving XBT sections taken in the central South Pacific Region. Only one mesoscale feature, with a width of 200 km, was identified. The maps of Wyrtki et al. (Figure III-3) and Cheney et al. (Figure III-1) both show low eddy levels in the region and increasing eddy activity with proximity to the Antarctic Circumpolar Current.

The XBT data obtained for the SP consist of nine sections and one survey. Figure III-21 shows a high resolution SXBT cruise by the CAF from New Zealand to Samoa in November 1982. The thermal signature of the South Subtropical Countercurrent (Tabata, 1975) is apparent at 24°S (Figure III-21a). This

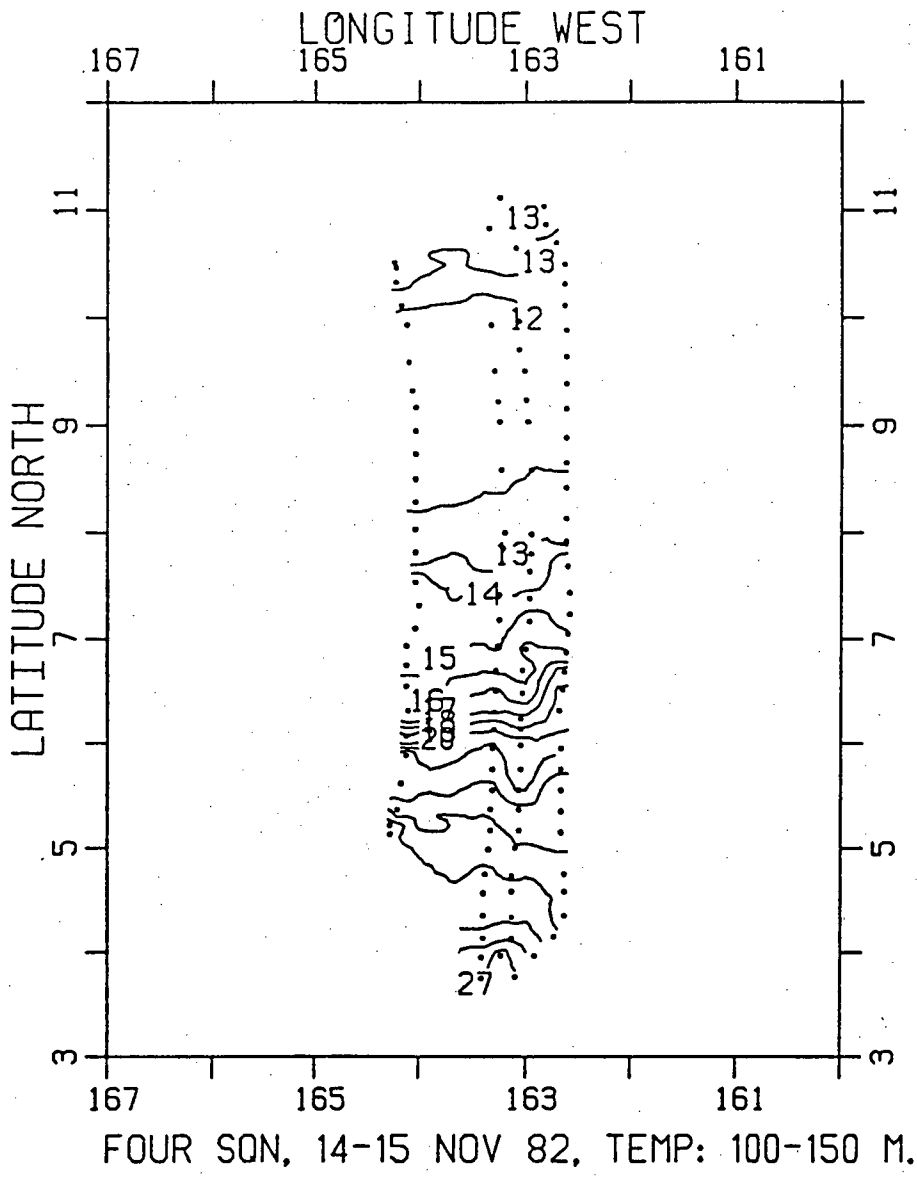

Figure III-19 CAF SXBT survey (QE-141182) of vertically-averaged temperature (°C) from 100 to 150 m taken across the North Pacific Equatorial Countercurrent, November 1982.

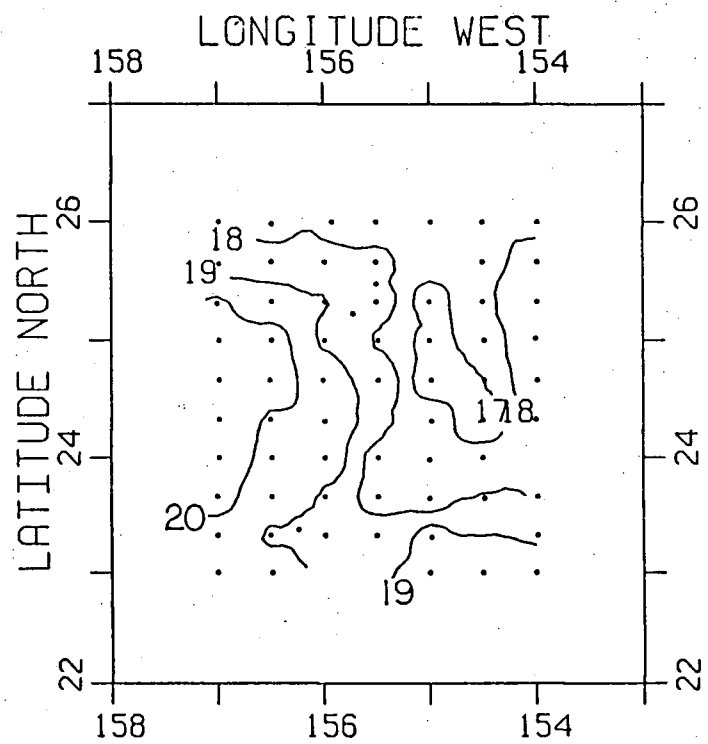

Figure III-20 USN AXBT survey (AA-16081) of vertically-averaged temperature (°C) from 150 to 200 m taken north of Hawaii, 16 January 1981.

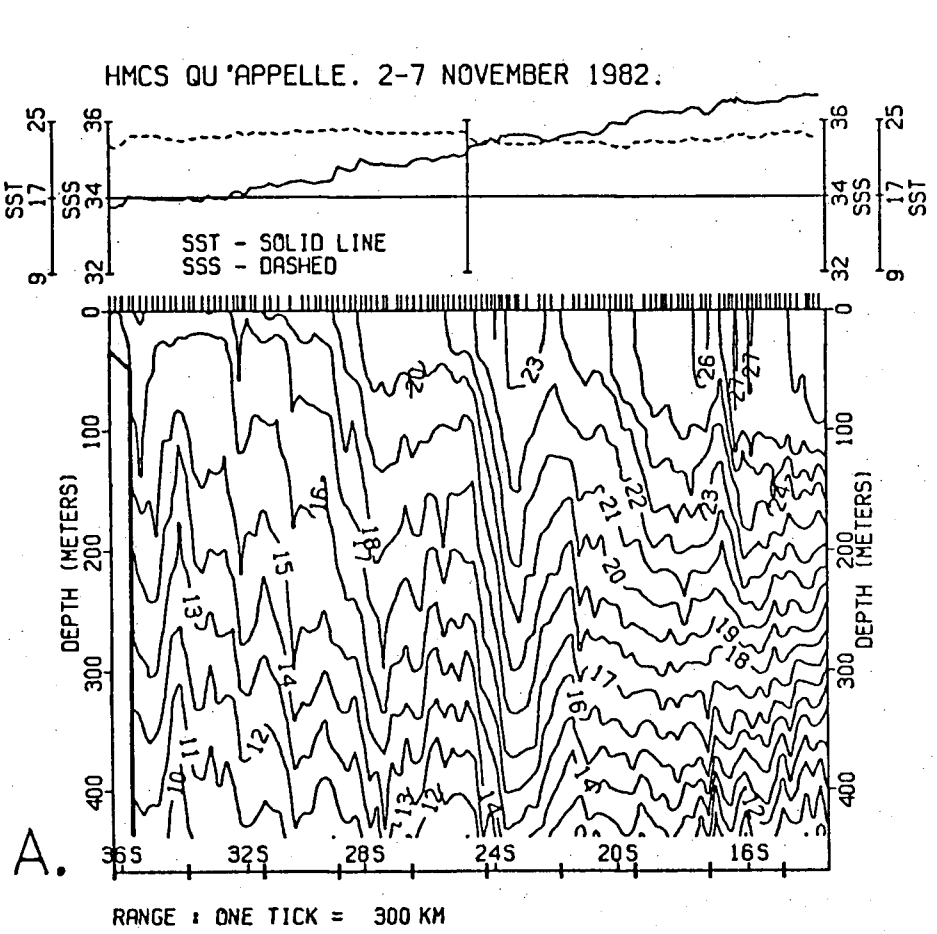

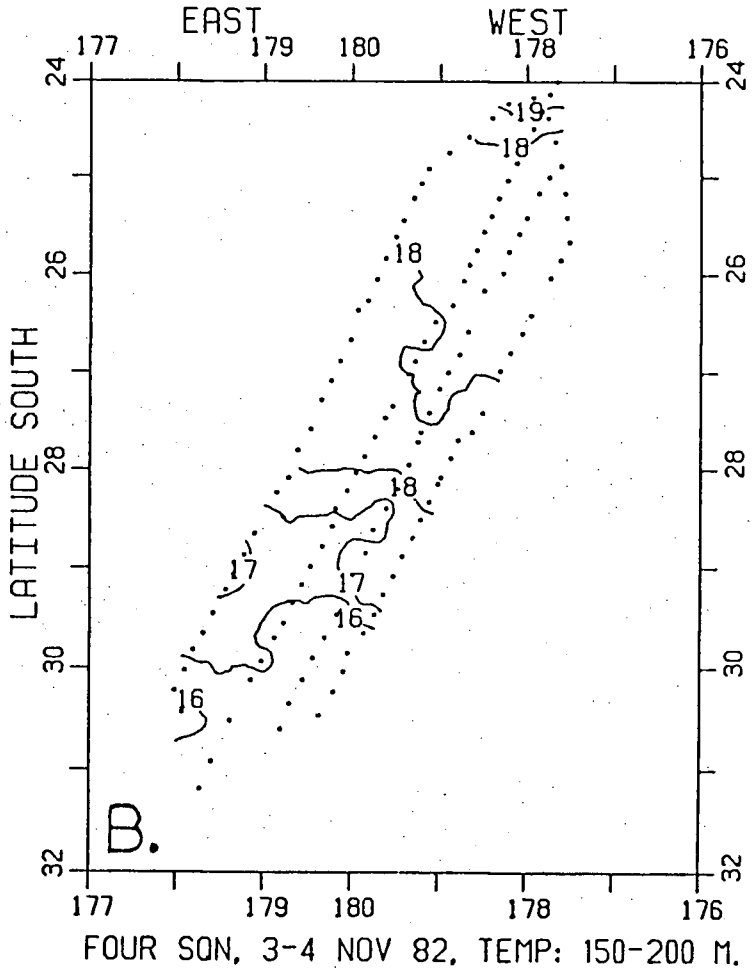

Figure III-21 CAF SXBT survey from New Zealand to Samoa, November 1982.
a. Temperature section (°C), QE-021182.
b. Map of vertically-averaged temperature (°C) from 150 to 200 m, QE-031182.

subsurface thermal front appears to be a permanent feature that was also present in all five SXBT sections reported by Denham et al. (1981) from New Zealand to Fiji. The amplitude and horizontal scale of the thermal eddy structure exhibit marked increases south of the front. Figure III-21a shows a warm eddy at 27.5°S with a width of about 400 km and a 150 m deflection of the 16°C isotherm. The multiship survey collected by the CAF on this cruise (Figure III-21b) was too narrow (180 km) to close the feature. Section 24-230483 (Figure III-22), taken in the northeast corner of the SP region, was obtained from NODC. It is relatively quiescent, although three eddies can be seen: a warm eddy at 106°W, a cold eddy at 93°W and a warm sub- thermocline eddy at 85°W. These features have widths of 300, 250 and 400 km, respectively, with displacements of the 11°C isotherm of 25, 30 and 60 m.

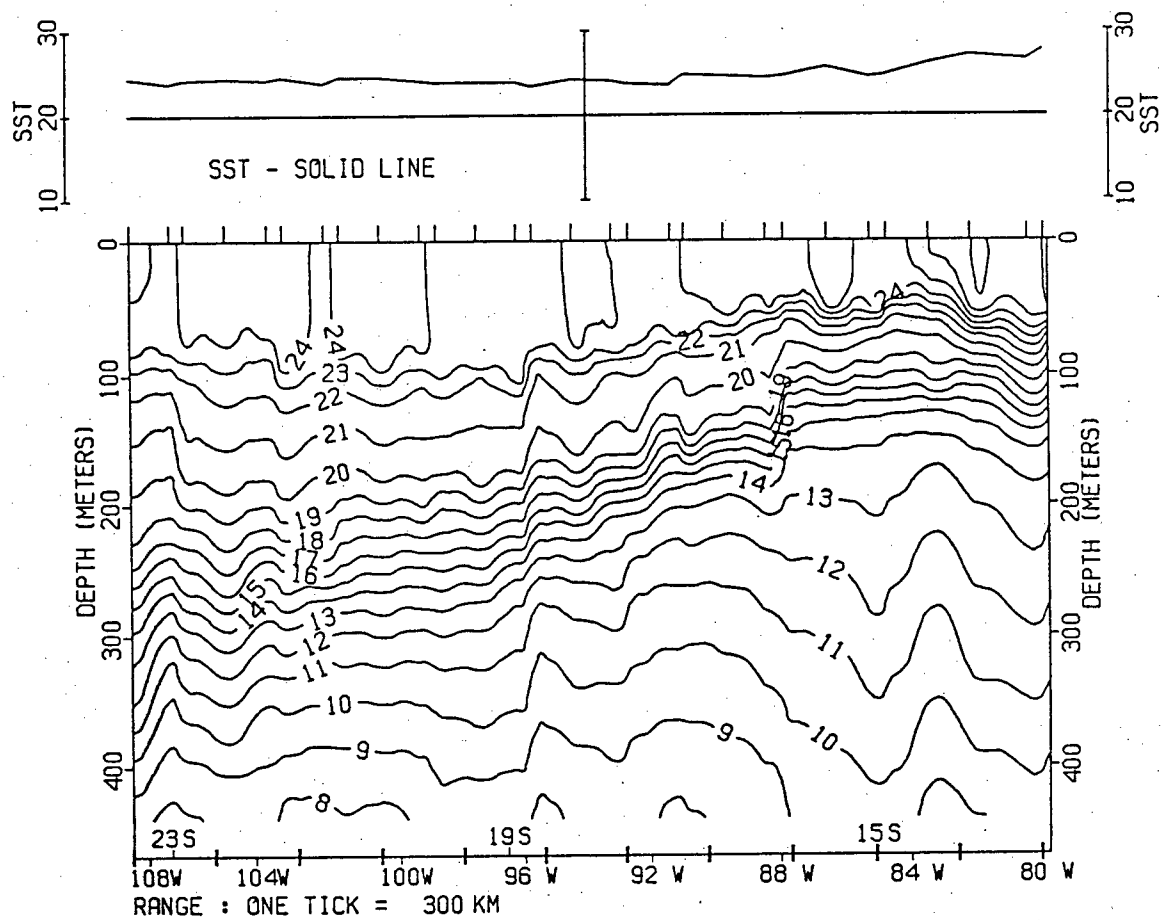

Figure III-22 **Temperature (°C) section (24-230483) obtained from the NODC in the eastern SP.**

IV. STATISTICAL ANALYSES

The purpose of this chapter is to quantify the geographic variability of the quasi-synoptic mesoscale structure in the upper 400 m of the ocean. Statistical analyses were used to compress the numerous observations into concise statements about what "usually" happens in the geographic regions, and how the regions differ from each other. The mid-thermocline temperature and the geopotential anomaly were used to represent the mesoscale eddy variability.

A sufficient number of observations must be available to obtain sample statistics which estimate the population statistics with reasonably small uncertainties. Each section and survey must be considered relatively small, in light of the few mesoscale perturbations per cruise and the relatively large decorrelation scales (on the order of the internal Rossby deformation radius). To increase the degrees of freedom, and therefore decrease the error bars, sample statistics were obtained using pooled estimates of the statistics in each geographic region. This required the assumption that the temperature field and the baroclinic eddy field were ergodic, stationary, random processes and that each XBT section or survey was an independant realization. The data were processed in three ways to substantiate these assumptions. First, as discussed in Chapter III, the geographic regions were defined on the basis of the variance of the eddy field. Only cruises in the same geographic region or in geographic regions with similar mesoscale variances were "averaged". Second, the large-scale current systems (trends) were removed from each section or survey to obtain the perturbation variables (i.e. mean equal to zero), of the mid-thermocline temperature and the geopotential anomaly, with near-normal frequency distributions. Third, the sections and surveys used were separated in space by at least the local internal Rossby radius, and separated in time by periods of weeks to years.

In this chapter, a quantitative representation of the mesoscale variability will be obtained by computing the central moments of the frequency distributions and the wavenumber spectra of the mid-thermocline temperature and the geopotential anomaly for each geographic region. The standard deviation, skewness, kurtosis and intermittency of the frequency distributions of each section and survey will be used. The seasonal variability of the mesoscale statistics in the NEP region will be examined. Isotropic, meridional and zonal

autocorrelation functions will be employed to discuss the assumption of isotropy. Wavenumber spectra will be used to identify spectral bandwidths of distinctive wavenumber ranges, and the dominant length scales of variability. Velocity spectra will be computed using the geostrophic relation to obtain kinetic energy estimates and the geostrophic velocity scales for each region.

A. SPATIAL SERIES

Spatial series and maps of the mid-thermocline temperature and geopotential anomaly, used to represent the upper-layer variability, were required for the statistical analyses. This involved the calculation of several quantities for each XBT and the removal of the low-wavenumber signal of the "large-scale" circulation. The resulting perturbation variables are signatures of the relatively high-wavenumber mesoscale eddy fields.

Three quantities were calculated for each XBT in the sections and surveys: the vertically-averaged temperature between 150 and 200 m, the vertically-averaged temperature between 350 and 400 m, and the geopotential anomaly between the surface and 4000 kPa (i.e. 0-400 db or 0-400 m). The temperature was averaged over two 50 m depth intervals to represent the mid-thermocline temperatures. The temperatures were averaged over a portion of the water column (i.e. 50 m) to reduce the high-wavenumber noise that might be induced by instrument error. No one depth can be adequately used to examine the variability of the thermocline on a global scale (Emery, 1983a). Examinations of the mean thermal structure of the geographic regions (Stommel et al. 1960; Defant, 1981; Emery and Dewar, 1982; Thomson et al. 1984b), and the standard deviations of the temperatures at 150 to 200 m and 350 to 400 m revealed the most appropriate depth interval for each region. In the NWA, NWP and NEA, the temperature between 350 and 400 m were used to represent the mid-thermocline variability, whereas, the temperature between 150 and 200 m were used in the SA, NEP and SP. The signature of the upper-layer baroclinic eddy field in the XBT data set was characterized by the geopotential anomaly (0-4000kPa).

The perturbation variables of the mid-thermocline temperature (T) and the geopotential anomaly (D) were obtained for each section by removing a 1000 km running mean. A running mean of this size was chosen to take out the low-wavenumber signal of the large-scale mean circulation systems and retain

the full amplitude of the mesoscale features. Bernstein and White (1974) observed dominant wavelengths of 600 to 400 km in the North Pacific, so an averaging interval of a greater scale was required. Detrending the sections with least-squares-fit polynomials was considered at some length, but rejected in favour of the running mean. Running means of 500, 750, 1000, and 1250 km were applied to typical spatial series in different geographic regions. The 1000 km running mean was considered the most appropriate. Figure IV-1 shows examples of the spatial series obtained for sections in the NWP and NEP.

The perturbation variables for each survey were determined by removing the meridional and zonal linear trends. This was considered more appropriate than the large running mean due to the relatively small dimensions of the surveys (except the USN multiship surveys). The removal of the zonal linear trend of the USN multiship surveys was still considered adequate, since these surveys were confined to the interior of the subtropical or subpolar gyres and did not cross major frontal systems (e.g. Gulf Stream or Kuroshio).

B. CENTRAL MOMENTS

The mesoscale variability represented by T and D may be quantitatively examined with the central moments of their sample probability density functions: the standard deviation, skewness and kurtosis. These statistics were calculated for each section and survey, and pooled statistics were obtained for each geographic region. The geographic variability of the temperature field and the baroclinic eddy field will be discussed.

A few comments must first be made about the use of the standard deviation, skewness and kurtosis for describing the mesoscale eddy field. The sample standard deviation, S, will provide a convenient measure of the average amplitude of the fluctuations. The standard deviation of the large-scale flow has been commonly used by oceanographers to quantify the intensity and geographic variability of the mesoscale eddy field (Wyrtki, 1975; Dantzler, 1976; Ebbesmeyer and Taft, 1979; Emery et al., 1980; Emery, 1983a). The standard deviations of T (S_T) obtained from this quasi-synoptic data set may be directly compared to the results of Emery (1983a) using climatological data (Figure III-4). The sample standard deviation was obtained for each section and survey by the relation:

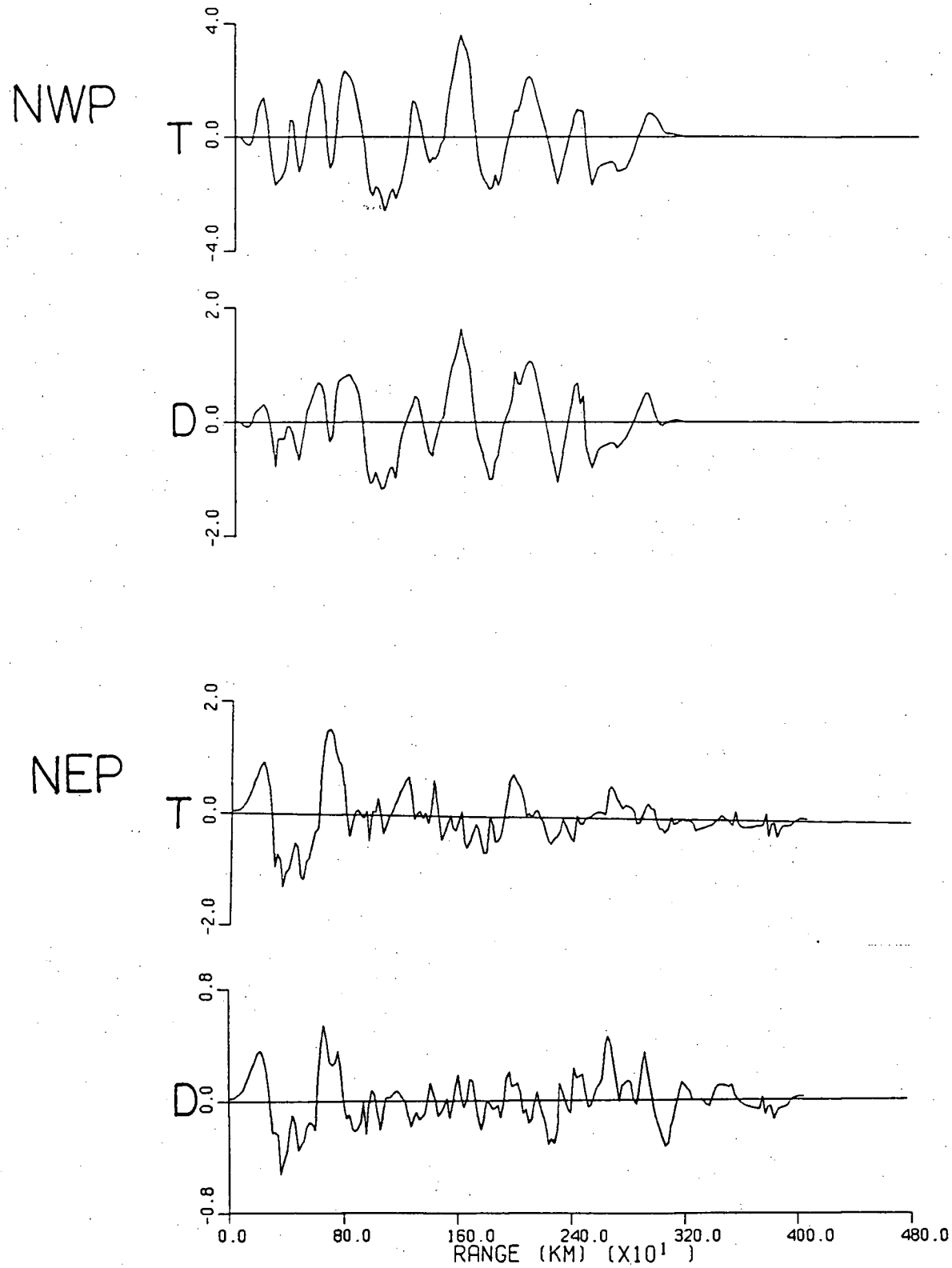

Figure IV-1 **Examples of the spatial series of the mid-thermocline temperature perturbations (T) and the geopotential anomaly perturbations (D) for trans-oceanic sections in the NWP and NEP.**

$$S = ((\Sigma_1^n x_i^2)/(n-1))^{1/2} \tag{4.1}$$

where x_i is T or D and n is the number of observations.

Skewness is a measure of departure of the frequency distribution from symmetry. It is the third central moment normalized by the standard deviation. A convenient estimate of skewness is:

$$W = \frac{(\Sigma_1^n x_i^3)/(n-1)}{S^3} \tag{4.2}$$

If the mode lies to the left of the mean, so that the frequencies fall off sharply to the left , the skewness is positive. This indicates that more values are negative and consequently the frequency distribution has a number of extreme positive values. A positive skewness of T or D would suggest that the mesoscale eddy field consists of a number of warm eddies in a relatively quiescent, cold background. The skewness of the population is considered to be significantly (95% confidence level) nonzero if the absolute value of W is greater than $1.96(6/n_i)^{1/2}$ (Brooks and Carruthers, 1953), where n_i is the number of independent observations.

Kurtosis is a measure of the disproportionality of the number of observations in the intermediate range between the mean and extreme values. It is the fourth central moment normalized by the standard deviation. A useful form of kurtosis is given by (Brooks and Carruthers, 1953):

$$K = \frac{((\Sigma_1^n x_i^4)/(n-1))}{S^4} - 3 . \tag{4.3}$$

If K is positive the frequency distribution is termed "leptokurtic" and it will have a relatively small number of observations in the intermediate ranges and a relatively large number of observations near the mean; if K is negative the frequency distribution is termed "platykurtic", with a large proportion of values in the intermediate ranges and a relatively small number of observations near the mean; and if K is zero the distribution is "isokurtic", as is a Gaussian distribution. The acceptance regions for testing the null hypothesis that K=0, at the 0.05 level of significance, are given by Brooks and Carruthers

(1953). The kurtosis of a population should not be estimated from a sample of less than 100 independent observations.

In the classical studies of turbulence (Hinze, 1975), K is known as the flatness factor and may be considered a measure for the degree of intermittency. Turbulence investigators have defined an intermittency factor, Q, as the fraction of the record length over which turbulence occurs. On the assumption that the variable concerned is normally distributed during the turbulent state, and is zero during the nonturbulent state, the relation Q(K+3)=3 was suggested (Hinze, 1975). The intermittency of the mesoscale eddy field may thus be quantified by estimating K and using the above relation.

In summary, the standard deviation is a measure of the average amplitude of the fluctuations of the variable; the skewness is a measure of the symmetry of the sampling density distribution; and the kurtosis is a measure of the relative number of values near the mean. Where K is significantly different from zero, the intermittency factor, Q, may be obtained. Q is the fraction of the sample where mesoscale perturbations occur. Thus, for given statistics, it may be said that the average amplitude of the mesoscale perturbations is S, that these perturbations occur in Q x 100% of the region and that the perturbations are predominantly cold (W<0) or warm (W>0) eddies.

Central Moments of the Sections

The sample statistics of T and D were calculated for each of the 95 sections. The numbers of independent observations (n_i) per section were determined from the autocorrelation function (ACF) of each variable. Spatial scales may be inferred from zero-crossings of the ACF, since the ACF of a field having a dominant wavelength should cross zero at the quarter-wavelength point (MODE Group, 1978). This decorrelation scale may be divided into the length of the spatial series to obtain n_i. The number of independent observations may not, of course, exceed the actual number of observations. The ACF of each variable was determined for each geographic region by averaging the ACFs of all the sections in the region. Table IV-1 presents the decorrelation scales obtained from the first-zero crossings of each variable in each region. These decorrelation scales were used to determine the numbers of independent observations.

Table IV-1 Decorrelation scales obtained from the first-zero crossings of the averaged autocorrelation functions for the sections in each geographic region.

Region	Decorrelation Scales (km)	
	T	D
NWA	59	63
NWP	72	76
NEA	54	52
SA	95	102
NEP	78	83
SP	81	77
HIGH	66	66
LOW	76	76

In order to examine the geographic variability of the variables, "pooled" statistics were calculated for each region. The pooled estimate of the sample standard deviations (S_p) is obtained from the relation (Walpole, 1974),

$$S_p^2 = (\Sigma_1^j (n_i-1)S_i^2)/(\Sigma_1^j n_i - j) \tag{4.4}$$

where j is the number of individual sample standard deviations, S_i. The pooled estimates of skewness (W_p) and kurtosis (K_p) are,

$$W_p = (\Sigma_1^j (n_i-1)S_i^3 W_i)/(\Sigma_1^j n_i - j)/S_p^3 \tag{4.5}$$

$$K_p = ((\Sigma_1^j (n_i-1)S_i^4 (K_i+3))/(\Sigma_1^j n_i - j)/S_p^4) - 3 \tag{4.6}$$

In the following discussion on the geographic variability of the mesoscale statistics, the significance of the pooled estimates, with respect to the population statistic of each region, is important. The methods used to determine whether or not W and K of the population are nonzero have been detailed already. The 95% confidence interval for the variance of a population (σ^2) is:

$$((n_i-j)/\chi^2_{.025})\ S^2 < \sigma^2 < ((n_i-j)/\chi^2_{.975}))\ S^2 \tag{4.7}$$

where $\chi^2_{.025}$ and $\chi^2_{.975}$ are the values of a chi-square distribution with n_i-j degrees of freedom, leaving areas of .025 and .975, respectively to the right. For $(n_i-j)>30$, a normal distribution is quite accurate, and thus χ^2 values may be computed by the formulas (Selby, 1965):

$$\chi^2_{.025} = 0.5\ (1.96 + (2(n_i-j)-1)^{1/2})^2$$

$$\chi^2_{.975} = 0.5\ (-1.96 + (2(n_i-j)-1)^{1/2})^2 \tag{4.8}$$

i. Mid-thermocline Temperature Statistics

The sample statistics of T are listed in Table IV-2. The standard deviations of the NWA and NWP are not significantly different. The S_T values in the low-energy regions are all equal within the 95% confidence limits. The HIGH region has a standard deviation of 1.40°C with a 95% confidence interval of 1.35 to 1.46°C from 1184 independent observations. The LOW region has a value of 0.54°C with a 95% confidence interval of 0.52 to 0.56°C from 2223 independent observations.

The geographic variability and the values of S_T are very consistent with the climatological results of Emery (1983a) shown in Figure III-4. The boundaries between the high-energy regions and the low-energy regions are approximately delineated by the 1.0°C contour of the standard deviation of the 260 m temperature. The high- and low-energy regions can also be approximately delineated by the 1.0°C contour in a similar map of the standard deviation of temperature at 460 m (Emery, 1983a). The NWA, NWP and HIGH regions have S_T values greater than 1.0°C; the NEA, SA, NEP, SP and LOW regions have S_T values less than 1.0°C. The amplitudes of the mesoscale variability as reflected in the standard deviations of the mid-thermocline temperatures of the quasi-synoptic data and the climatological data are very consistent.

The HIGH and LOW regions have Q_T values of 0.45 and 0.49, respectively. These statistics suggest that perturbations of T greater than 1.40°C occur in about 45% of the HIGH region, while perturbations of 0.54°C occur in about 49% of the LOW region. The skewness of the HIGH region ($W_T<0$) suggests that the perturbations are predominantly cold eddies, whereas, the skewness of the LOW region ($W_T>0$) suggests that they are warm eddies. The ratio of the standard deviation of the mid-thermocline temperature of the HIGH region to the LOW region is 2.59. The 95% confidence limits of this ratio, obtained using the F distribution (Selby, 1965), are 2.16 and 3.09. Thus the average amplitude of the mid-thermocline temperature perturbations in the high-energy regions is 2.5 times that of the low-energy regions.

ii. Geopotential Anomaly (0-4000 kPa) Statistics

The sample statistics of the geopotential anomaly (0-4000 kPa) perturbations are listed in Table IV-3. The NWA and the NWP have significantly

Table IV-2 Sample standard deviation, skewness, kurtosis and intermittency of the mid-thermocline temperature (T) for the geographic regions from the sections. W and K values that are significantly nonzero are underlined. Q is shown only when K is significantly nonzero.

Region	n_i	S_T (°C)	95% Confidence Limits (°C)	W_T	K_T	Q_T
NWA	901	1.43	1.37 - 1.50	-0.66	3.96	0.43
NWP	283	1.30	1.20 - 1.40	0.13	1.63	0.63
NEA	503	0.51	0.48 - 0.54	0.04	3.89	0.44
SA	88	0.48	0.42 - 0.54	0.14	-0.22	-
NEP	1354	0.57	0.55 - 0.59	0.17	3.55	0.46
SP	278	0.56	0.51 - 0.60	0.12	1.69	0.74
HIGH	1184	1.40	1.35 - 1.46	-0.51	3.60	0.45
LOW	2223	0.54	0.52 - 0.56	0.11	3.16	0.49

Table IV-3 Sample standard deviation, skewness, kurtosis and intermittency of the geopotential anomaly (D) for the geographic regions from the sections. W and K values that are significantly nonzero are underlined. Q is shown only when K is significantly nonzero.

Region	n_i	S_D (m^2/s^2)	95% Confidence Limits (m^2/s^2)	W_D	K_D	Q_D
NWA	854	0.69	0.66 - 0.72	0.12	<u>3.63</u>	0.45
NWP	271	0.58	0.54 - 0.63	-0.05	<u>1.44</u>	0.68
NEA	517	0.21	0.19 - 0.22	<u>0.25</u>	<u>1.73</u>	0.63
SA	85	0.20	0.18 - 0.23	-0.01	0.88	-
NEP	1330	0.26	0.25 - 0.27	<u>0.21</u>	<u>3.44</u>	0.47
SP	279	0.32	0.30 - 0.35	<u>0.63</u>	<u>4.50</u>	0.40
HIGH	1125	0.67	0.64 - 0.69	0.10	<u>3.44</u>	0.47
LOW	2211	0.26	0.25 - 0.27	<u>0.33</u>	<u>4.10</u>	0.42

different S_D values. The low-energy regions all have standard deviations that are significantly lower than the high-energy regions and are generally not significantly different from each other. The HIGH region has a standard deviation of 0.67 m^2/s^2 with a 95% confidence interval of 0.64 to 0.69 m^2/s^2 from 1125 independent observations. The LOW region has a standard deviation of 0.26 m^2/s^2 with a 95% confidence interval of 0.25 to 0.27 m^2/s^2 from 2211 independent observations. The skewness of the HIGH region is not significantly different from zero, whereas, the skewness of the LOW region is significantly positive. The HIGH and the LOW regions have intermittencies of 0.47 and 0.42, respectively.

These statistics suggest that geopotential anomaly perturbations greater than 0.67 m^2/s^2 may be found in about 47% of the HIGH region, that perturbations greater than 0.26 m^2/s^2 may be found in about 42% of the LOW region and that the LOW region has mesoscale perturbations that are predominantly warm eddies. The ratio of the standard deviations of the HIGH region to the LOW region is 2.58 with 95% confidence limits of 2.15 and 3.08. Thus, the average amplitude of the geopotential anomaly perturbations (0-4000 kPa) in the high-energy regions is about 2.5 times that of the low-energy regions.

Central Moments of the Surveys

The central moments of the mid-thermocline temperature and the geopotential anomaly were calculated for each of the 29 surveys. Pooled estimates of each statistic were determined for the geographic regions. In the NEP, two subregions were also examined: the North Pacific Subtropical Front (NPSF), and the North Pacific Equatorial Current (NPEC). These statistics will be discussed and compared with those of the trans-oceanic sections. The number of independent observations, n_i, was determined by dividing the square of the decorrelation scale (Table IV-1, from the first-zero crossings of the averaged ACFs of the sections) of the appropriate region into the area of each survey.

i. Mid-thermocline Temperature Statistics

The sample statistics of T from the surveys are shown in Table IV-4. The standard deviations of the NWA and NWP are significantly different. The S_T

Table IV-4 Sample standard deviation, skewness, kurtosis and intermittency of the mid-thermocline temperature (T) for the geographic regions, the NPSF and the NPEC from the surveys. W and K values that are significantly nonzero are underlined. Q is shown only when K is significantly nonzero.

Region	No. of Surveys	n_i	S_T (°C)	95% Confidence Limits (°C)	W_T	K_T	Q_T
NWA	6	494	1.71	1.61 - 1.81	-0.59	1.89	0.61
NWP	2	230	1.42	1.30 - 1.54	0.47	1.06	0.74
NEA	4	466	0.66	0.62 - 0.70	0.63	1.41	0.68
NEP	16	236	1.11	1.02 - 1.20	0.37	0.86	0.78
NPSF	10	129	0.91	0.81 - 1.02	0.24	0.44	-
NPEC	4	68	1.39	1.19 - 1.60	0.36	0.20	-
SP	1	16	0.46	0.34 - 0.71	0.04	-0.48	-

of the NEP is significantly larger than the other two low-energy regions. The NPEC has a S_T of 1.39°C which is significantly larger than that of the NPSF. Compared to the S_T values of the sections in each region, the S_T of the surveys are significantly higher (except in the SP), particularly that of the NEP which is almost twice as large. The skewness of T is significantly nonzero in the NWA, NWP, the NEA and the NEP. The signs of W_T from the sections for these regions are the same for the NWA and NEP. The values of Q_T compare reasonably well with those obtained from the sections, with the exception of the NEP. Q_T of the surveys, for the NEP, is larger by a factor of 1.7. These statistics are consistent with those of the sections. The intermittencies Q_T are somewhat larger than the corresponding statistics of the sections.

ii. Geopotential Anomaly (0-4000 kPa) Statistics

The sample statistics of the geopotential anomaly obtained from the surveys are shown in Table IV-5. In the high-energy regions, the NWA and the NWP have S_D values that are equal within the 95% confidence limits. The NEA, the NEP and the SP have values of S_D that are, generally, equivalent within the 95% confidence limits. The NPEC has a standard deviation which is significantly larger than the value of the NPSF. The standard deviations from the surveys are equal to those from the sections within the 95% confidence limits in the NWA, the NWP and the SP. The NEA and the NEP have significantly higher S_D values from the surveys than from the sections. The skewness is significant in the NWP, the NEA, the NPSF and the NPEC. The NWP and the NEA values, only, are consistent with those from the sections. The intermittences are all within 0.10 of the corresponding Q_D from the sections, except for the NWA which has a higher Q_D from the surveys than the sections. The NPSF has a Q_D of 0.61 compared to the NEP Q_D of 0.37.

Summary of the Central Moments

The geographic variability of the mesoscale temperature field and baroclinic eddy field have been discussed with the pooled estimates of the central moments of the sections and surveys. The primary results can be summarized as follows:

Table IV-5 Sample standard deviation, skewness, kurtosis and intermittency of the geopotential anomaly (D) for the geographic regions, the NPSF and the NPEC from the surveys. W and K values that are significantly nonzero are underlined. Q is shown only when K is significantly nonzero.

Region	No. of Surveys	n_i	S_D (m^2/s^2)	95% Confidence Limits (m^2/s^2)	W_D	K_D	Q_D
NWA	6	432	0.71	0.67 - 0.76	0.21	1.76	0.63
NWP	2	207	0.63	0.59 - 0.71	0.52	1.04	0.74
NEA	4	502	0.32	0.30 - 0.34	0.99	2.42	0.55
NEP	16	206	0.46	0.42 - 0.50	-0.06	5.11	0.37
NPSF	10	112	0.32	0.28 - 0.35	0.53	1.91	0.61
NPEC	4	60	0.53	0.45 - 0.61	-1.09	6.75	-
SP	1	17	0.46	0.34 - 0.70	0.26	-0.70	-

a. The baroclinic mesoscale eddy field in the high- and low-energy regions can be quantitatively compared using the central moments of the HIGH and LOW regions. The HIGH region has geopotential anomaly perturbations with average amplitudes of 0.67 m^2/s^2, and the LOW region has perturbations with average amplitudes of 0.26 m^2/s^2. The average amplitudes of the geopotential anomaly perturbations are 2.58 times greater in the HIGH region than in the LOW region. The positive skewness of the LOW region suggests that the baroclinic eddy field consists, predominantly, of warm eddies. The skewness of the HIGH region is not significantly different from zero. The intermittencies are the same and indicate that the mesoscale perturbations occur over about 45% of each region.

b. The geographic variability of the mesoscale eddy field can also be examined with the mid-thermocline temperature statistics. The HIGH and LOW regions have standard deviations of 1.40 and 0.54°C, respectively. The ratio of the standard deviation of the HIGH region to the LOW region is 2.59, which is the same as that for the geopotential anomaly of the two regions. The positive skewness of the temperature in the LOW region is consistent with that discussed above. The negative skewness in the HIGH region suggests that the baroclinic eddy field consists of predominantly cold eddies, as opposed to the field of warm eddies in the low-energy regions.

c. The standard deviations and intermittencies of the surveys are, for the most part, greater than the corresponding statistics of the sections. In the NEP, this is a result of sampling subregions of relatively high eddy activity (i.e. the NPSF and NPEC). In the NWA, NWP and NEA, this is a result of detrending the surveys with a linear trend, rather than a 1000 km running mean.

d. The NPSF and NPEC, as subregions of the NEP, have mesoscale statistics characteristic of the low-energy regions. The standard deviations of temperature and geopotential anomaly in the two subregions are greater than the corresponding statistics of the NEP from the sections. The standard deviations of the mid-thermocline temperature and baroclinic eddy fields are greater in the NPEC than the NPSF. The skewness of D in the NPSF is positive. This is consistent with the NEP statistics. The NPEC has a negative W_D. This is consistent with the field of cold eddies that was found in the AXBT surveys discussed in Chapter III.

C. SEASONAL VARIABILITY OF THE STATISTICS

The seasonal variability of the mesoscale statistics of the NEP will be examined in this section. The distribution of the quasi-synoptic XBT data set, in the four quarters of the year (Table IV-6), shows some seasonal biases. In particular, the high-energy regions have no sections in the first quarter and over 60% of the sections in the last quarter. Each low-energy region, generally, has a good distribution of data throughout the year (with the obvious exception of the SA). When the low-energy regions are considered as a whole, there is a reasonably even distribution of data throughout the year. The effect that these seasonal biases will have on the results is not clear. The NEP is the geographic region with the most even distribution of sections over the four quarters of the year. The variability of the pooled statistical estimates of the NEP for the four quarters of the year will be used to investigate the potential for the seasonal biasing of the regional statistics due to the uneven distribution of the sections over the year.

The quarterly-pooled statistics of the NEP are summarized in Table IV-7. The standard deviation, skewness and intermittency factor have seasonal variations for both T and D. The standard deviations of T and D are largest in the first two quarters of the year and smallest in the last two quarters of the year. The quarterly-pooled skewness of each variable is consistent with the corresponding regionally-pooled skewness with one exception. W_D in the fourth quarter is negative rather than positive. The intermittencies of T and D exhibit similar seasonal variations with the largest intermittencies in first and third quarters and the smallest intermittencies in the second and fourth quarters.

In summary, it has been seen that in the NEP the standard deviation, skewness and intermittency exhibit a seasonal variability. This suggests that the mesoscale statistics obtained from the quasi-synoptic XBT data set may be seasonally biased for the NWA, NWP, HIGH, NEA, SA and SP (i.e. all the regions except the NEP and LOW) due to the uneven distribution of the sections over the year.

These regions will have seasonally-biased statistics only, of course, where the statistics have seasonal signals. To the author's knowledge, the seasonal variability of the mesoscale eddy field has been reported only in a subregion

Table IV-6 Summary of the number of sections by geographic region and quarter of the year.

Geographic Region	Quarter of the Year 1	2	3	4	Total
HIGH					
NWA	0	4	4	15	23
NWP	0	4	0	4	8
Total	0	8	4	19	31
LOW					
NEA	1	4	4	7	16
SA	2	0	0	0	2
NEP	8	5	10	14	37
SP	3	1	0	5	9
Total	14	10	14	26	64

Table IV-7 Summary of the statistics of T and D from the sections for the NEP by quarter of the year. W and K values that are significantly nonzero are underlined. Q is shown only when K is significantly nonzero. The T standard deviations have units of °C. The D standard deviations have units of $(m/s)^2$.

Variable	Quarter	No. of Sections	n_i	S	95% Confidence Limits	W	K	Q
T	1	8	294	0.68	0.63 - 0.73	0.09	1.17	0.72
	2	5	205	0.65	0.59 - 0.71	0.59	4.43	0.40
	3	10	407	0.42	0.39 - 0.44	0.45	2.04	0.60
	4	14	448	0.58	0.54 - 0.61	-0.12	4.05	0.43
D	1	8	285	0.29	0.26 - 0.31	0.34	2.40	0.56
	2	5	202	0.32	0.29 - 0.35	0.42	3.90	0.44
	3	10	402	0.22	0.20 - 0.23	0.45	1.29	0.70
	4	14	441	0.25	0.23 - 0.26	-0.30	3.20	0.48

of the NEA. Dickson et al. (1982) found a significant seasonal signal of the eddy kinetic energy estimates at a number of sites in the Northeast Atlantic, north of the Azores (35°N to 60°N). The North East Atlantic Dynamics Study (NEADS) collected two-year-long current records at depths between 200 and 4000 m. The amplitude of the signal was large enough that the records were dominated by the winter maxima. This effect was seen from 200 to 4000 m at all the sites with significant bottom slopes or roughness.

The paucity of the data available will not permit a more comprehensive examination of the issue. This analysis may be used to highlight the potential of the biasing of the results due to seasonal signals of the mesoscale eddy field, however the biasing cannot be quantitatively or even qualitatively determined.

D. HORIZONTAL ANISOTROPY

An anisotropy factor, A_S has been evaluated using the averaged autocorrelation functions of the surveys to parameterize the horizontal anisotropy of the mesoscale eddy fields. The anistropy factor is obtained from the relation, $A_S = L_M/L_Z$, where L_M and L_Z are the meridional and zonal decorrelation scales obtained from the first zero-crossings of the averaged meridional and zonal autocorrelation functions, respectively. The anisotropy factor is important, to evaluate the assumption of isotropy that has been widely used in this and other studies. Where the mesoscale eddy fields are not isotropic, A_S will provide a measure of that anisotropy.

The averaged isotropic, meridional and zonal autocorrelation functions (ACFs) were calculated from the surveys in each geographic region. The ACFs of each survey were calculated by binning the perturbation variables of each pair of XBTs into 20 km wide bins. For the isotropic ACF, the XBT pairs were binned according to the rhumbline distance between them. The meridional and zonal ACFs where calculated by binning the XBT pairs by their meridional and zonal separation, respectively, within 20 km wide swaths. Due to the limited meridional or zonal extent of some of the surveys, the meridional and zonal ACFs are somewhat noisy. The averaged ACFs were obtained by averaging the appropriate individual ACFs within the geographic regions. As an example, plots of the ACFs for the NWP and the NEP are shown in Figure IV-2.

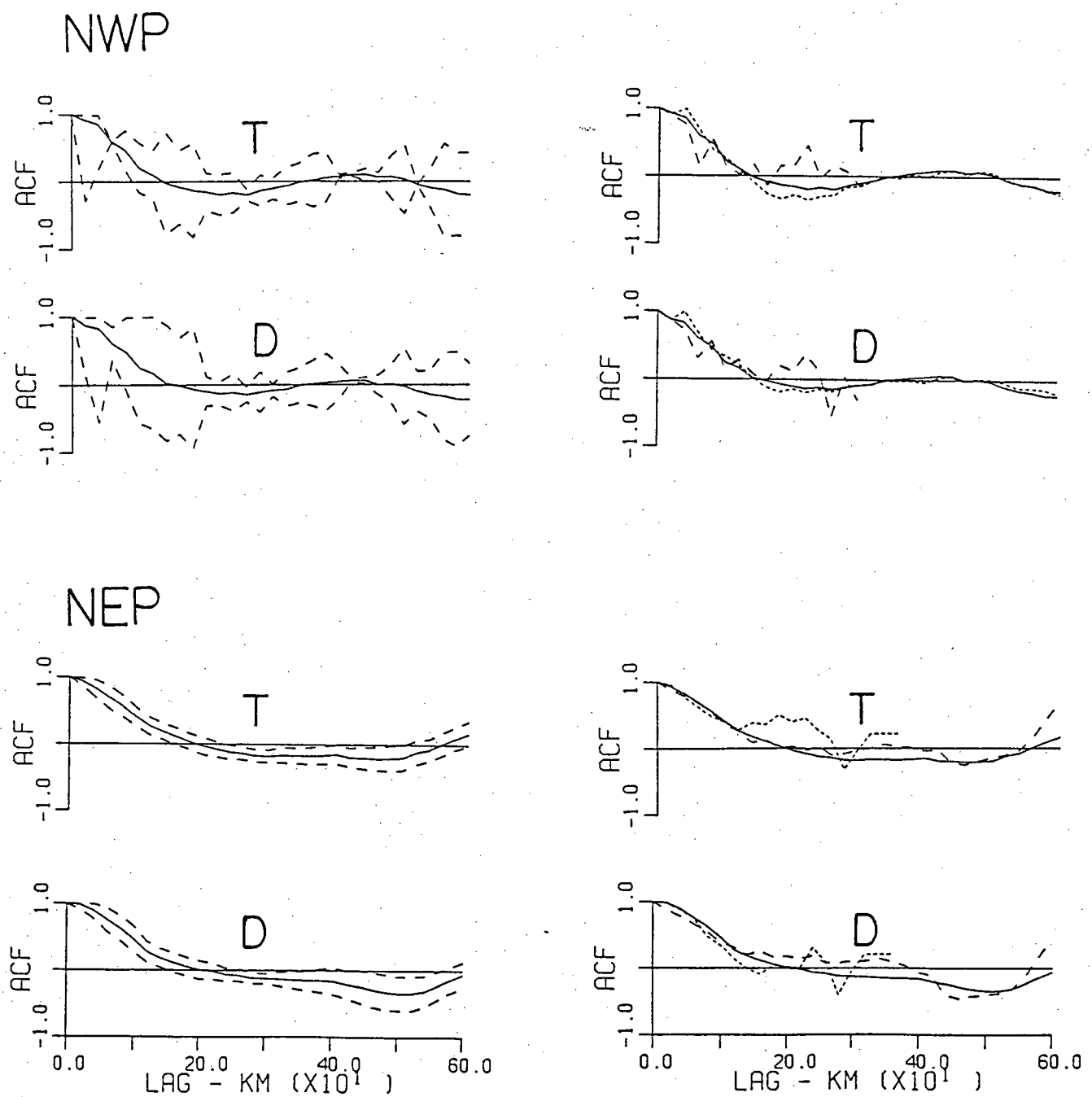

Figure IV-2 Sample plots of the averaged isotropic, meridional and zonal autocorrelation functions for the NWP and NEP. The plots on the left are the isotropic ACFs with 95% confidence limits (dashed lines). The plots on the right are the isotropic ACFs (solid line), meridional ACFs (long-dashed line) and the zonal ACFs (short-dashed line).

The isotropic decorrelation scales obtained from the first-zero crossings of the regionally-averaged ACFs of the surveys are summarized in Table IV-8. The geographic variability of these decorrelation scales, that can be defined to the 95% confidence limits (i.e. the scales that are underlined in Table IV-8), exhibit the same general geographic variability as the decorrelation scales from the sections (Table IV-1). These decorrelation scales are about twice as large as those of the sections because the large-scale signal was detrended with a linear fit for the surveys and a 1000 km running mean for the sections. The 95% confidence limits of the scales in Table IV-8 may be determined from the first-zero crossings of the 95% confidence limits of the ACFs. The decorrelation scale cannot be uniquely determined at the 95% confidence level where the upper 95% confidence limit does not cross zero. The confidence limits are wide and are not shown. It is sufficient to say that, without a single exception, the isotropic decorrelation scales are not significantly different from each other.

The anisotropy factor and the meridional and zonal decorrelation length scales are summarized by geographic region in Table IV-9. The 95% confidence limits of L_M and L_Z may be determined in the same manner as the isotropic decorrelation scales with the 95% error bars (not shown). L_M and L_Z are nowhere significantly different from each other, thus, A_S is not different from one. There is no significant indication from these results that the mesoscale eddy fields are anisotropic and therefore the assumption of isotropy, for the mesoscale eddy fields examined in this investigation, appears to be quite reasonable.

E. WAVENUMBER SPECTRA

The purpose of this section is to examine the geographic variability of the wavenumber spectra of the mid-thermocline temperature and the geopotential anomaly perturbations. This section is divided into subsections discussing the methods used to estimate the spectra, the total spectral variance, the distribution of variance in wavenumber space, the dominant wavelengths, the eddy kinetic energy, and the baroclinic length and velocity scales.

This examination of the wavenumber spectra will be restricted to the range of 10^{-3} to 10^{-2} cycles/km (i.e. 1000 to 100 km wavelengths) similar to the SEASAT altimetry analysis of Fu (1983). The mesoscale signals are either

Table IV-8 Isotropic decorrelation scales obtained from the first-zero crossings of the regionally-averaged autocorrelation functions of the surveys. The decorrelation scales that can be defined to the 95% confidence level are underlined.

Region	Decorrelation Scales (km)	
	T	D
NWA	147	145
NWP	135	150
NEA	146	130
NEP	191	200
NPSF	150	143
NPEC	122	104
SP	115	>180

Table IV-9 The anisotropy factor, $A_S = L_M/L_Z$, is the ratio of the meridional decorrelation length scale (L_M) from the averaged meridional autocorrelation function of the the surveys to the zonal decorrelation length scale (L_Z) from the averaged zonal autocorrelation function. The units of L_M and L_Z are kilometers.

Region	T			D		
	A_S	L_M	L_Z	A_S	L_M	L_Z
NWA	**0.34**	85	250	**0.55**	123	224
NWP	**1.10**	152	138	**1.08**	153	142
NEA	--	>160	149	--	>160	140
NEP	**0.73**	210	289	**2.76**	387	140
NPSF	**0.75**	119	159	**0.86**	111	129
NPEC	--	89	>320	--	85	>320
SP	**1.01**	117	116	--	110	>180

sufficiently small or sufficiently attenuated by the high-pass filter to be unimportant at wavenumbers less than 10^{-3} cycles/km. The average sampling intervals of the spatial series in the geographic regions vary considerably from 100 to 35 km. This creates a wide range of Nyquist wavenumbers that are generally (with the exception of the SA and the SP) greater than 10^{-2} cycles/km. As will be seen, the geophysical signals at wavenumbers higher than 10^{-2} cycles/km, contain relatively small amounts of the variance compared to the 10^{-3} to 10^{-2} cycles/km range. The use of this wavenumber range also facilitates the comparison of the spectra between the geographic regions and with the results of Fu (1983).

Estimation of the Spectra

The geographic variability of the variance in wavenumber space will be examined using normalized variance-conserving spectral plots, and the dominant wavelengths will be identified using variance-conserving spectral plots with error bars.

The spectra of each geographic region were obtained by averaging the spectra of the individual trans-oceanic sections. The raw spectral estimates of each section were calculated using a Fourier transform subroutine available in the UBC Computing Centre software library (Moore, 1981). This subroutine requires no padding or truncating of the data. The raw estimates of the sections were binned into wavenumber bins with widths of 3.9×10^{-3} cycles/km and averaged, to obtain regional raw spectral estimates between 1.95×10^{-4} and 2.5×10^{-2} cycles/km. Smoothed spectral estimates were computed with a Daniell (boxcar) window over five adjoining spectral estimates.

Variance-conserving plots of the spectra where produced by multiplying the smoothed spectral estimates by their corresponding wavenumbers and plotting the results on a logarithmic wavenumber scale. The area under any wavenumber band of this plot is equal to the variance within that wavenumber band times 2.3. (If these plots were produced on a natural logarithmic wavenumber scale, the area under the curve would be equal to the variance.) Normalized variance-conserving plots of the spectra were produced for the wavenumber range 10^{-3} to 10^{-2} cycles/km by dividing the variance-conserving spectra by the total variance within this wavenumber range. The area under the curve of a

normalized variance-conserving plot between 10^{-3} and 10^{-2} cycles/km on a natural logarithmic wavenumber scale is equal to one. The spectra have been plotted on a logarithmic wavenumber scale to the base ten to facilitate interpretation. Examples of the normalized variance-conserving spectra are shown in Figure IV-3. These spectra will be used to discuss the geographic variability of the distribution of the variance of each variable between the wavelengths of 1000 and 100 km.

Two different sets of error bars were produced for each variance-conserving spectrum. An example is shown in Figure IV-4. Ninety-five percent and eighty percent confidence intervals were determined using the standard error of each spectral estimate. The 95% confidence intervals were calculated with the relation $\pm C_{.025}S_S/(n_S)^{1/2}$, where S_S is the sample standard deviation of the smoothed spectral estimate and n_S is the number of spectral estimates. For $n_S > 30$, $C_{.025} = 1.960$, the value of the standard normal distribution leaving an area of .025 to the right. For $n_S \leq 30$, $C_{.025}$ was obtained from the Student-t distribution with n_S-1 degrees of freedom. The 80% confidence intervals were calculated with the same relation using $C_{.01}$. These error bars, account for the uncertainty of the spectral estimates due to the computational procedure and the uncertainty due to the instrument noise and geophysical signal.

Spectral Variance

The spectral variance of T and D, between wavelengths of 1000 and 100 km, was obtained by integrating the variance-conserving spectra. The SA and SP regions were integrated up to their Nyquist wavenumbers at about the 200 km wavelength, so their variances are not directly comparable to the other regions. The variance estimates with 95% confidence limits are summarized in Table IV-10. The spectral variances in this wavenumber band, naturally, exhibit the same patterns of geographic variability as the regionally-pooled estimates of the standard deviations of the spatial series. In the HIGH region, the variances of T and D are $1.018°C^2$ and $0.237\ (m/s)^4$, respectively. In the LOW region these variances are $0.169°C^2$ and $0.040\ (m/s)^4$. The variance of each variable is significantly higher in the HIGH region compared to the LOW region.

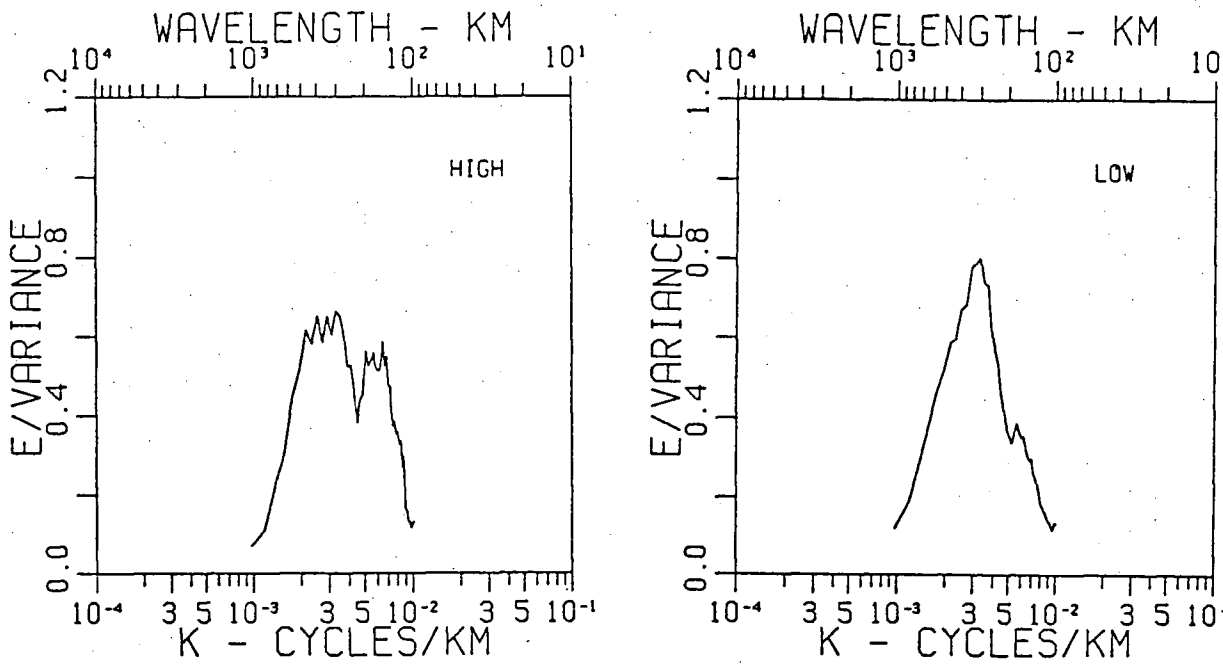

Figure IV-3 Examples of the normalized variance-conserving spectra. These two spectra represent the variance of the geopotential anomaly perturbations, D, as a function of wavenumber for the HIGH and LOW regions. The variance-conserving spectra were normalized by the total variance between wavenumbers of 10^{-3} and 10^{-2} cycles/km. These spectra are used to compare the spectral shapes between geographic regions.

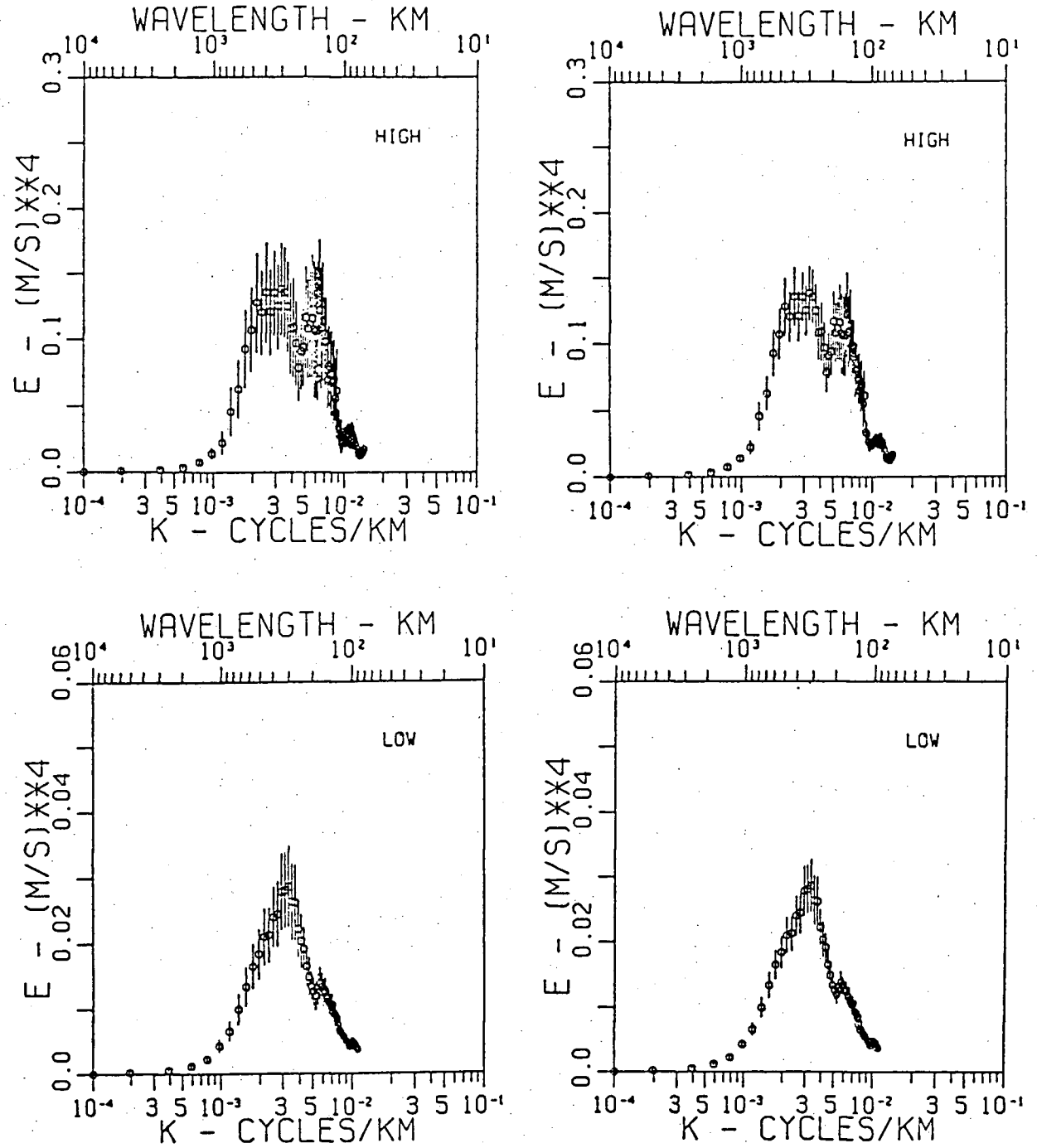

Figure IV-4 **Examples of the variance-conserving spectra with confidence limits. This figure presents the spectra of the geopotential anomaly perturbations for the HIGH and LOW regions with two different sets of error bars. The spectra on the left side have 95% confidence intervals obtained with the standard error of the spectral estimates of the sections. The spectra on the right side have 80% confidence intervals obtained in the same manner. These spectra are used to identify distinct peak wavenumbers and the confidence with which they are defined.**

Table IV-10 Variance of T and D with 95% confidence limits obtained by integrating the spectra between wavelengths of 1000 and 100 km. The SA and SP variances have asterisks since these regions have average Nyquist wavenumbers less than 10^{-2} cycles/km. The variances of these regions were obtained by integrating the spectra from 10^{-3} cycles/km to the Nyquist wavenumber (at approximately a 200 km wavelength).

	T		D	
Region	Variance ($°C^2$)	95% Confidence Limits ($°C^2$)	Variance (m^4/s^4)	95% Confidence Limits (m^4/s^4)
NWA	1.014	0.665 - 1.426	0.239	0.142 - 0.336
NWP	1.015	0.580 - 1.378	0.219	0.131 - 0.307
NEA	0.107	0.041 - 0.173	0.017	0.010 - 0.027
SA	0.096*	0.077 - 0.121	0.016*	0.011 - 0.023
NEP	0.194	0.149 - 0.246	0.045	0.036 - 0.056
SP	0.131*	0.092 - 0.170	0.035*	0.017 - 0.049
HIGH	1.018	0.732 - 1.304	0.237	0.168 - 0.321
LOW	0.169	0.139 - 0.211	0.040	0.031 - 0.049

Interpretation of the Spectra

The geographic variability of the wavenumber spectra and the dominant wavelengths of the wavenumber spectra will be discussed with the normalized variance-conserving plots of each variable as depicted on maps showing the geographic regions that the spectra represent (e.g. Figure IV-5). This product has been designed to facilitate the geographic comparisons of the spectral shapes. The dominant wavelengths of variation of each variable are summarized by geographic region in tables (e.g. Table IV-11). This product lists the peak wavelengths, the confidence levels, the bandwidths and the percentage of variance (between 10^{-3} and 10^{-2} cycles/km) that is accounted for by the wavenumber bands. The dominant wavelengths and confidence intervals were determined from variance-conserving spectra with error bars. The wavelength bands were defined by the half-power points of the spectral peaks or the troughs between adjacent bands. The percentage of the variance, that each wavelength band contributes to the total variance between 1000 and 100 km, was determined from normalized variance-conserving spectra.

i. Spectra of the Mid-thermocline Temperature

The normalized variance-conserving spectra of T are shown in Figure IV-5. The dominant wavelengths are tabulated in Table IV-11. The spectrum of the NWA has two dominant wavelengths and the spectrum of the NWP has three dominant wavelengths which are distinct to at least the 80% confidence level. The low-energy regions have one dominant wavelength each (except for the NEP) which are distinct to at least the 80% confidence level. The NEP has two dominant wavelengths, both distinct to the 95% confidence level.

The T spectrum of the HIGH region has peak wavelengths at 340 km, distinct to the 95% confidence levels, and at 195 km, distinct to the 80% confidence levels. The LOW region has peak wavelengths of 320 and 170 km, both distinct to the 95% confidence levels. The difference in the distribution of the variance between these two spectra is characteristic of the differences between the spectral shapes of the high- and low-energy regions. Although the dominant wavelengths are comparable, the HIGH region has a smaller percentage of its variance in the larger wavelength band and twice the percentage of its variance in the shorter wavelength band than the LOW region.

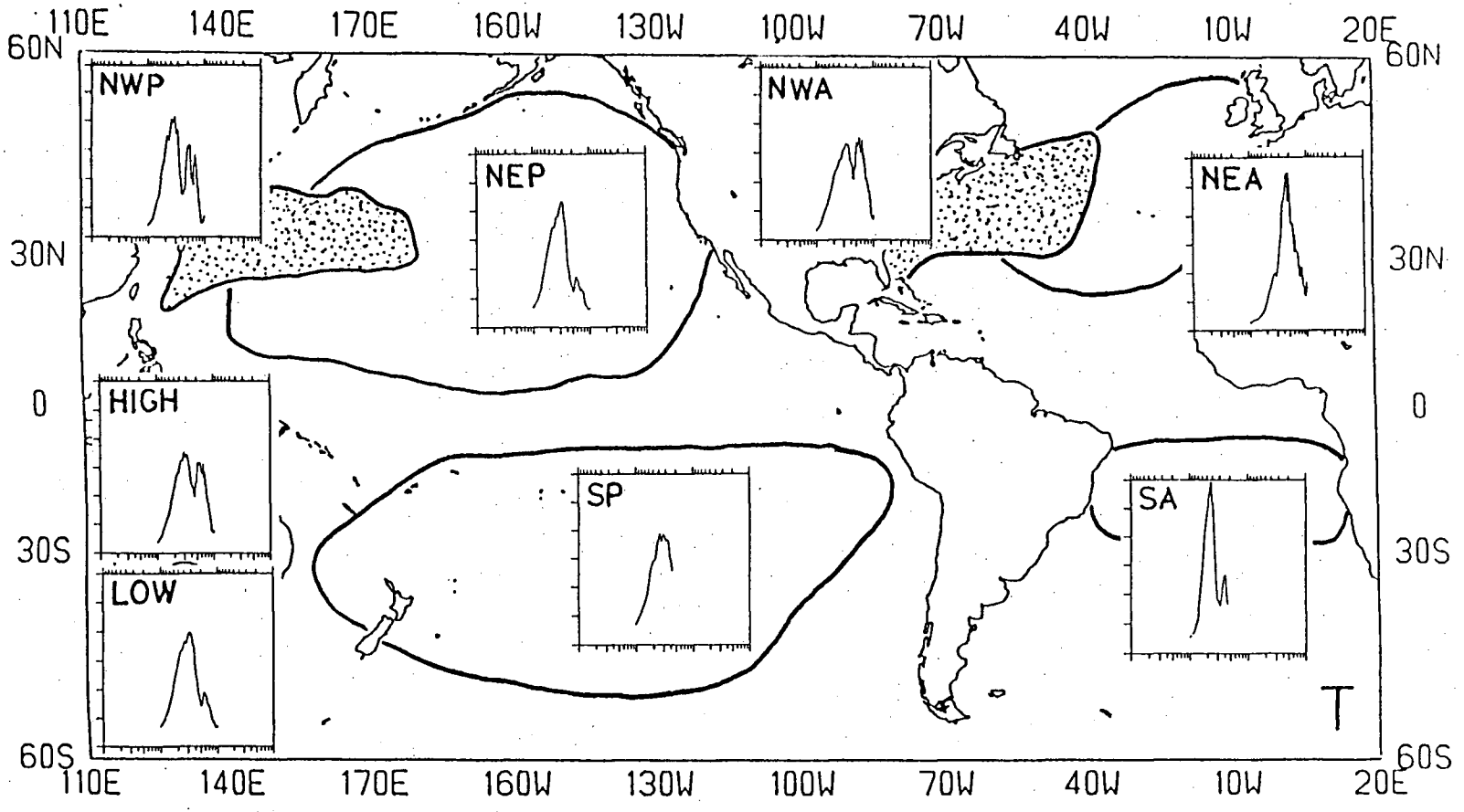

Figure IV-5 Normalized variance-conserving spectra of the mid-thermocline temperatures on a map showing the regions that the spectra represent. The stippled areas are the high-energy regions. The spectra are plotted between wavenumbers of 10^{-3} and 10^{-2} cycles/km.

Table IV-11 Peak wavelengths of the temperature spectra. The peaks are distinct to the confidence limits shown. The wavelength band indicates the range between the half-power points. The percent variance is the contribution to the total variance between wavelengths of 1000 and 100 km. The total variances of the SA and SP were determined between 1000 and 200 km.

Region	Peak Wavelength (km)	Confidence Level	Wavelength Band (km)	Percent of Variance
NWA	285	95%	560 - 220	53
	165	80%	220 - 120	35
NWP	340	95%	590 - 245	58
	180	80%	245 - 160	18
	145	80%	160 - 120	13
NEA	220	95%	320 - 130	63
SA	395	80%	600 - 300	73
	250	--	300 - 210	18
NEP	320	95%	600 - 200	70
	170	95%	200 - 110	13
SP	395	80%	600 - 220	81
HIGH	340	95%	600 - 220	53
	195	80%	220 - 130	30
LOW	320	95%	700 - 195	70
	170	95%	195 - 120	15

ii. Spectra of the Geopotential Anomaly (0-4000 kPa)

The normalized variance-conserving spectra of D are shown in Figure IV-6. The dominant wavelengths are tabulated in Table IV-12. The NWA has two dominant wavelengths. The longest wavelength is distinct to the 95% confidence level and the shorter wavelength is not distinct to the 80% confidence level. The NWP has three peak wavelengths, all distinct to at least the 80% confidence level. The NEA has three dominant wavelengths. The SA and the NEP have two dominant wavelengths each and the SP has one dominant wavelength. The longer wavelengths of the NEA, SA and NEP are distinct to the 95% confidence level. The other wavelengths are not distinct at the 80% confidence level.

The spectral shapes of the HIGH and LOW regions are, of course, similar to those of the mid-thermocline temperature spectra. The respective spectral peaks in the HIGH region occur at 300 km, distinct to the 95% confidence level, and at 155 km. The 155 km peak is not distinct to the 80% confidence level. The D spectrum in the LOW region has peak wavelengths at 300 km, distinct to the 95% confidence level, and at 170 km. The latter spectral peak is not distinct to the 80% confidence level.

iii. Summary of the Wavenumber Spectra

The geographic variability of both the wavenumber spectra and the dominant wavelengths of the mesoscale temperature and baroclinic eddy fields can be summarized as follows:

a. The dominant wavelengths of variability of the T and D variables have been identified with confidence levels at which they are distinct (Tables IV-11 and IV-12). The dominant wavelengths are between 400 and 100 km. There are no significant scale separations between the dominant length scales of the high-energy regions and the low-energy regions. The variances of the high-energy regions are, however, significantly higher than the variances of the low-energy region for a given variable.

b. In all regions, the longer wavelength bands contain the greatest percentage of the mesoscale eddy variances. Although the dominant wavelengths are generally comparable between the high- and low-energy regions, the

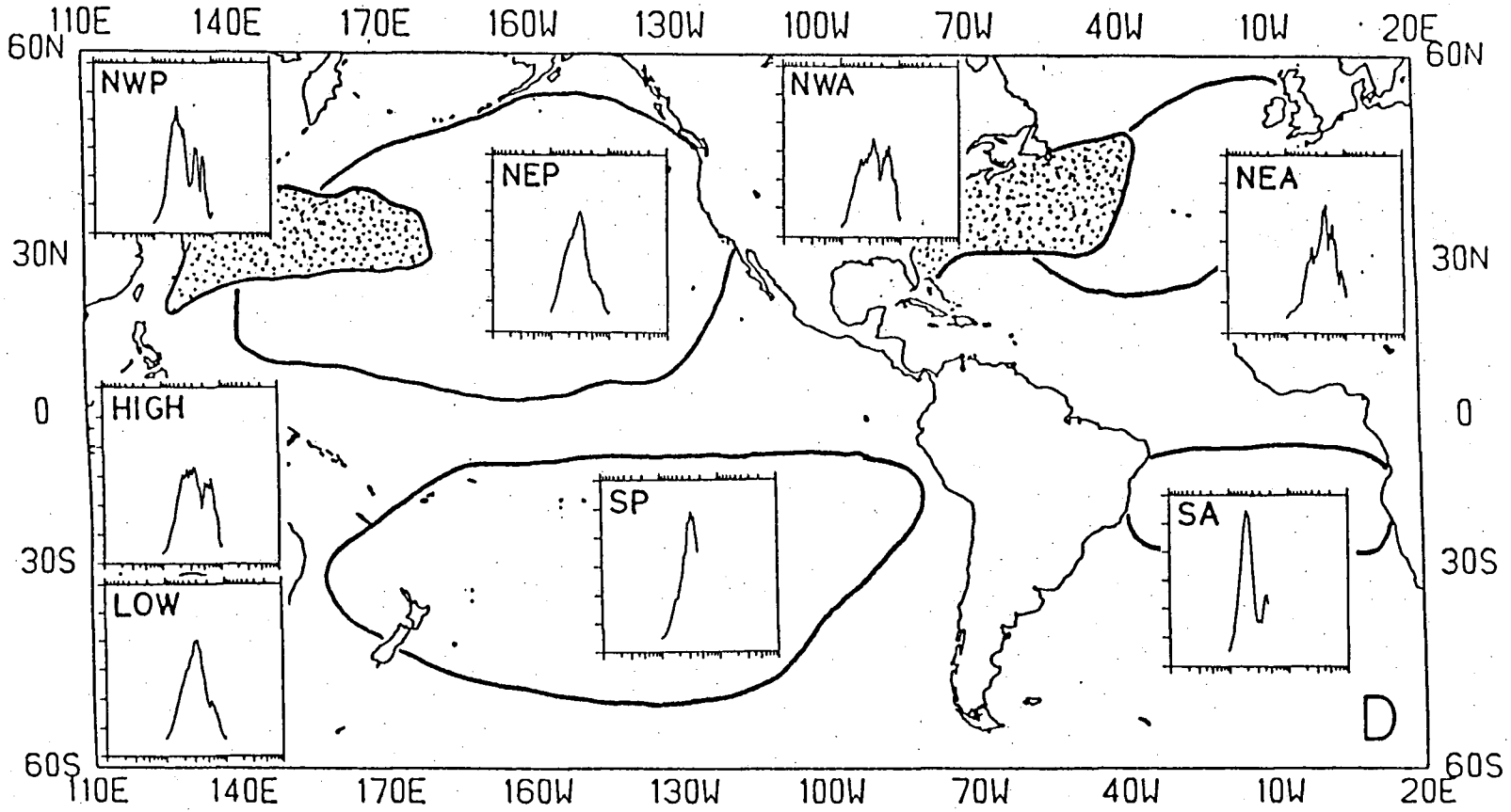

Figure IV-6 Normalized variance-conserving spectra of the geopotential anomaly on a map showing the regions that the spectra represent. The stippled areas are the high-energy regions. The spectra are plotted between wavenumbers of 10^{-3} and 10^{-2} cycles/km.

Table IV-12 Peak wavelengths of the geopotential anomaly spectra. The peaks are distinct to the confidence limits shown. The bandwidths are between the half-power points of the peaks. The percent variance is the contribution to the total variance between wavelengths of 1000 and 100 km. The total variances of the SA and SP were determined between 1000 and 200 km.

Region	Peak Wavelength (km)	Confidence Level	Wavelength Band (km)	Percent of Variance
NWA	285	95%	600 - 220	55
	155	--	220 - 120	35
NWP	395	95%	600 - 240	55
	195	80%	240 - 155	20
	145	95%	155 - 130	10
NEA	205	95%	340 - 190	33
	160	--	190 - 130	23
	115	--	130 - 100	10
SA	510	95%	680 - 320	63
	245	--	320 - 220	15
NEP	320	95%	620 - 190	71
	170	--	190 - 120	16
SP	300	--	500 - 220	73
HIGH	300	95%	620 - 220	60
	155	--	220 - 120	30
LOW	300	95%	690 - 190	73
	170	--	190 - 120	15

high-energy regions, compared to the low-energy regions have smaller percentages of their variances in the longer wavelengths and about twice the percentages of variances in the shorter wavelength bands.

c. The NEA region is an anomalous region. The dominant wavelengths are noticeably shorter than those of the other geographic regions. The anomalous nature of the NEA is perhaps due to some set of characteristic forcing mechanisms in the region.

Eddy Kinetic Energy Estimates

Geostrophic velocity spectra have been used to estimate the geostrophic eddy kinetic energy in the wavenumber range 10^{-3} to 10^{-2} cycles/km and the portions of this EKE attributable to the wavenumber bands of each peak in the geopotential anomaly spectra. The normalized variance-conserving spectra of the geostrophic velocity were obtained from the geopotential anomaly spectra with the geostrophic relation. The wavenumber bands correspond very closely to those of the D spectra. The total eddy kinetic energy per unit mass was calculated for the wavenumber band 10^{-3} to 10^{-2} cycles/km by integrating these variance-conserving spectra. The 95% confidence limits on these EKE estimates were determined by integrating the respective curves defined by the lower bound of the 95% confidence limits and the upper bound of the 95% confidence limits.

The EKEs obtained from the integration of the geostrophic velocity spectra provide only that portion of the kinetic energy due to one of the two orthogonal horizontal components of the perturbation velocities. They must therefore be termed the one-dimensional EKE. The two-dimensional isotropic EKE has been estimated as two times the one-dimensional eddy kinetic energy. Under the present assumption that the perturbation variables in each geographic region are ergodic, stationary, random processes, the autocovariance function is rotationally invariant. The velocity spectra of the two orthogonal components of the perturbation velocities will, thus, be similar and their contributions to the two-dimensional isotropic eddy kinetic energy will be approximately the same. This is admittedly a simplistic, and by no means rigorous argument, but it will provide an estimate of the two-dimensional isotropic eddy kinetic energy for comparison with the estimates of Wyrtki *et al.* (1976) and Fu (1983).

The two-dimensional EKE estimates for the wavelength bands between 1000 and 100 km are summarized in Table IV-13. The two-dimensional EKEs of the high-energy regions are 258 and 236 cm^2/s^2, respectively, in the NWA and the NWP. These estimates are not significantly different. In the low-energy regions, the NEA, SA, NEP and SP have two-dimensional EKEs of 18, 20, 40 and 24 cm^2/s^2 respectively. The NEP has about twice the eddy kinetic energy of the NEA, a significant difference. The SA and SP cannot be directly compared to the NEA and NEP since their kinetic energies were estimated over a smaller wavenumber range. The eddy kinetic energies of the SA and the SP are, however, not signficantly different from each other. The HIGH region has a two-dimensional isotropic EKE of 250 cm^2/s^2 with 95% confidence limits of 222 to 306 cm^2/s^2. The LOW region has a value of 36 cm^2/s^2 with 95% confidence limits of 32 to 40 cm^2/s^2. The HIGH region has about seven times the geostrophic eddy kinetic energy of the LOW region in wavelengths between 1000 and 100 km.

Two-dimensional isotropic eddy kinetic energies were estimated by Fu (1983) using SEASAT altimetry data. He reported EKEs of 290 cm^2/s^2 for the high-energy regions and 50 cm^2/s^2 for the low-energy regions. The estimated EKE of the HIGH region using the quasi-synoptic XBT data set is not significantly different from the results of Fu. In the LOW region, Fu's results are significantly greater than those of the XBT data set by a factor of 1.25. The EKEs estimated by Fu are those associated with the barotropic signals with periods less than 24 days. The EKEs estimated in this investigation are those associated with the baroclinic signals in the upper 400 m of the ocean. The latter EKEs will miss an important part of the barotropic signal because the level of no motion (i.e. the depth at which the barotropic signal is compensated by the baroclinic signal) is generally considered to be on the order of 1000 m, not the 400 m used in this investigation. Despite these underestimates, the EKEs from the quasi-synoptic XBT data set compare very well with those of Fu, since they do not filter any frequency band out of the 1000 to 100 km wavelength band. The eddy kinetic energies reported by Fu and estimated in this investigation are less than those of Wyrtki et al. (1976) by a factor of 5. This can be explained by the fact that the EKEs of Fu and this investigation are underestimated (as discussed above), and the EKEs of Wyrtki et al. are overestimated due to the wind drift of the ships.

Table IV-13 **Two-dimensional isotropic eddy kinectic energy estimates of the geographic regions. The SA and SP were integrated up to the Nyquist wavenumber (i.e. about 200 km).**

Region	Two-dimensional Isotropic Eddy Kinetic Energy (cm^2/s^2)	95% Confidence Limits (cm^2/s^2)
NWA	258	201 - 315
NWP	236	209 - 330
NEA	18	14 - 21
SA	20	15 - 31
NEP	40	33 - 45
SP	24	21 - 30
HIGH	250	222 - 306
LOW	36	32 - 40

The contribution of each dominant bandwidth of the geopotential anomaly spectra to the total two-dimensional isotropic eddy kinetic energy is shown in Table IV-14. In the high-energy regions, the distributions of the EKEs in wavenumber space are very comparable, with the exception that the energy of the NWP in the band of 240 to 130 km is divided between two distinct wavenumber bands. In the low-energy regions, although the total EKE of the SA and SP cannot be directly compared to the other regions, the geographic variability of the eddy kinetic energies within individual wavenumber bands may be compared. With the exception of the NEA, the low-energy regions have eddy kinetic energies of about 20 cm^2/s^2 at wavelengths greater than 200 km. The NEA has one-quarter of the EKE of the other low-energy regions at wavelengths greater than 200 km. The NEA has about half the eddy kinetic energy of the NEP at wavelengths less than 200 km.

The HIGH region has an EKE of 65 cm^2/s^2 at wavelengths larger than 200 km, whereas the LOW region has 14 cm^2/s^2. In wavelengths shorter than 200 km, the EKEs of the HIGH and LOW region are 185 and 17 cm^2/s^2, respectively. Both the HIGH and LOW regions have more of their eddy kinetic energies in the shorter wavelengths.

Baroclinic Length and Velocity Scales

The dominant length scales of variability of the baroclinic mesoscale eddy fields and the corresponding velocity scales were obtained from the wavenumber spectra. The geographic variability of these scales will be discussed and the results will be used in the dynamical analyses of Chapter V.

The variability of the baroclinic mesoscale eddy field in the upper level of the ocean may be best represented by the geopotential anomaly (i.e. the D spectra). The dominant length scales were taken as the peak wavelengths of the D spectra (Table IV-12) divided by 2π. The velocity scales were taken as the square-root of the values of the variance-conserving geostrophic velocity spectra at the corresponding wavelengths. The velocity scales correspond to the baroclinic signal in the upper 400 m of the water column. An important portion of the barotropic signal has most certainly been missed, therefore, these velocity scales are underestimates of the true velocity perturbations. The true velocity scales may be approximated by considering the fact that the EKEs reported by Wyrtki et al. (1976) are a factor of five greater than the

Table IV-14 Contribution of each bandwidth of the geopotential anomaly spectra to the two-dimensional isotropic eddy kinetic energy.

Region	Peak Wavelength (km)	Confidence Level	Wavelength Band (km)	Percent of Eddy Kinetic Energy	Eddy Kinetic Energy (cm^2/s^2)
NWA	285	95%	600 - 220	20	52
	155	--	220 - 120	55	142
NWP	395	95%	600 - 240	29	68
	195	80%	240 - 155	31	73
	145	95%	155 - 130	34	80
NEA	205	95%	340 - 190	29	5
	160	--	190 - 130	40	7
	115	--	130 - 100	23	4
SA	510	95%	680 - 320	47	9
	245	--	320 - 220	47	9
NEP	320	95%	620 - 190	45	18
	170	--	190 - 120	48	19
SP	300	--	500 - 220	91	22
HIGH	300	95%	620 - 220	26	65
	155	--	220 - 120	74	185
LOW	300	95%	690 - 190	40	14
	170	--	190 - 120	48	17

EKEs estimated in this chapter. The estimates of Wyrtki et al. are considered high, therefore, an upper bound to the true velocity perturbations of the observed baroclinic length scales may be estimated by simply multiplying the baroclinic velocity scale, U, by $(5)^{1/2}$ to obtain U*.

The dominant length and velocity scales are summarized in Table IV-15. These length scales exhibit a geographic variability which is, of course similar to that of the decorrelation scales of the geopotential anomaly in Table IV-1. The decorrelation scales were said to reflect the size of the largest dominant perturbations. The decorrelation scales of Table IV-1 may be compared with the length scales of Table IV-15 after multiplying them by 0.64 (i.e. decorrelation scale x $(4/2\pi)$ = length scale). The D decorrelation scales are the same size or slightly smaller than the largest dominant scales of Table IV-15. Comparable decorrelation scales between the HIGH and LOW regions would be expected from an examination of the dominant length scales of the two regions. The decorrelation scale of the HIGH region is significantly larger, however, as a result of the HIGH region having a larger percentage of its variance in the shorter length scales (Table IV-12).

Table IV-15 **Length scales (L) and velocity scales (U) of the baroclinic mesoscale eddy variability. The length scales were obtained from the peak wavelengths of D spectra ($L=\lambda/2\pi$). The bold length scales are distinct to the 95% confidence limits of the D spectra, and the underlined lengthscale is distinct to the 80% confidence limits. The other length scales are not distinct to the 80% confidence limits. The velocity scales (U) were obtained from the geostrophic velocity spectra. The upper bound of the true velocity perturbations (U*) were obtained by multiplying U by $(5)^{1/2}$, since Wyrtki et al.'s (1976) EKEs are a factor of five greater than the EKEs reported in this chapter, and are considered an overestimate of the true EKEs.**

Region	L (km)	U (cm/s)	U* (cm/s)
NWA	**45**	10.2	22.8
	25	18.1	40.5
NWP	**63**	8.9	19.9
	31	14.5	32.4
	23	18.6	41.6
NEA	**33**	3.8	8.5
	26	4.6	10.2
	25	4.8	10.7
SA	**81**	4.0	8.9
	39	5.6	12.5
NEP	**51**	4.6	10.3
	27	5.5	12.3
SP	48	6.3	14.1
HIGH	**48**	9.6	21.5
	25	17.5	39.1
LOW	**48**	4.5	10.1
	27	5.5	12.3

V. DYNAMICAL INFERENCES

The purpose of this chapter is to examine the geographic variability of the mesoscale dynamics using the preceding statistical results. Quasigeostrophy is a type of dynamical balance with certain characteristic length, velocity and time scales, which includes linear Rossby waves, nonlinear Rossby waves and quasigeostrophic turbulence. The results of MODE-I (Richman et al., 1977; MODE Group, 1978) have shown that linear dynamics do not appear to be applicable in the vicinity of the Gulf Stream, but have led investigators to suggest that the somewhat weaker motions to the east may be linear. This hypothesized inhomogeneity of the dynamics is consistent with the demonstrated spatial inhomogeneity of the eddy kinetic energy and dominant horizontal length and velocity scales. Rhines (1977) suggested that there is never likely to be enough data to make the stability of statistical estimates of mesoscale properties really satisfactory and that,

> "it seems to be more useful to invent crude dynamical tests which withstand the paucity of data, rather than make a monolithic drive to determine the full frequency-wavenumber spectrum of the eddies".

The relevant quasigeostrophic dynamics will be inferred with the statistical results of Chapter IV, and the geographic variability of the dynamics will be discussed. The nondimensional quasigeostrophic scaling parameters will be evaluated using the dominant horizontal length and velocity scales. The properties of free linear baroclinic Rossby waves will be examined for each geographic region and the wavenumber spectra will be compared with several models of nonlinear geophysical turbulence.

A. Quasigeostrophic Scaling Parameters

The quasigeostrophic equations for stratified fluids may be derived using systematic scaling arguments. The scaling analysis is a consequence of an explicit choice to describe a particular class of motions. The nonlinear potential vorticity equation for a stratified fluid on a β-plane of constant depth, in nondimensional form, is (LeBlond and Mysak, 1978),

$$\frac{D_h}{Dt}\left(\nabla_h^2 \psi + (B^{-1}\psi_z)_z + \frac{\beta^*}{Ro} y\right) = 0$$

where

$$\frac{D_h}{Dt} = \frac{\partial}{\partial t} + \frac{\partial \psi}{\partial x}\frac{\partial}{\partial y} - \frac{\partial \psi}{\partial y}\frac{\partial}{\partial x}, \quad \nabla_h^2 = \frac{\partial^2}{\partial x^2} + \frac{\partial^2}{\partial y^2} \tag{5.1}$$

ψ is the streamfunction, Ro is the Rossby number, B is the Burger number and β^* is the sphericity parameter. In order to obtain this quasigeostrophic potential vorticity equation from the scaled inviscid hydrostatic equations for a rotating stratified fluid, it is required that Ro<<1, B = O(1) and β^*<<1.

These three nondimensional quasigeostrophic scaling parameters are: $Ro = U/(f_o L)$, $B = (NH)^2/(f_o L)^2 = (r_i/L)^2$ and $\beta^* = \beta_o L/f_o$, where U is the velocity scale, L is the horizontal length scale, f_o is the Coriolis parameter at a given latitude, β_o is the meridional gradient of f_o at a given latitude, N is the Brunt-Vaisala frequency, H is the water depth and r_i is the internal Rossby deformation radius. The Rossby number is the ratio of the inertial to the Coriolis forces. When Ro<<1, the Coriolis forces dominate over the inertial forces. The Burger number is a measure of the stratification. As stratification increases, motion parallel to the local direction of gravity is inhibited and the motions become nearly horizontal. The Burger number can also be written as the square of the ratio of the internal deformation radius and the horizontal length scale. The condition B = O(1) implies that the motions under consideration are on the order of r_i (Pedlosky, 1979). The sphericity parameter is a measure of the change of the Coriolis parameter over the meridional scale of the motion (Charney and Flierl, 1981). The condition β^*<<1 is a requirement for the use of the β-plane. An examination of these parameters, as evaluated with the horizontal length and velocity scales from Chapter IV, will reveal the applicability of the quasigeostrophic equations to the observed mesoscale variability.

Equation (5.1) is a conservation statement for the quasigeostrophic approximation to the potential vorticity which is a linear combination of three terms. The first two terms are due to the relative motion. The first is the relative vorticity and the second is the contribution to the potential vorticity due to the sloping isopycnals in the water column.

The Burger number, $B = (r_i/L)^2$, is a measure of the relative importance of the first term to the second term. The Rossby deformation radius is the scale for which the sloping isopycnals (vortex-tube stretching) and the relative vorticity make equal contributions to the potential vorticity (Pedlosky, 1979). When L is less than r_i, there is a negligible contribution to the potential vorticity by the vortex-tube stretching.

The third term in (5.1) is the ambient potential vorticity. The Rossby wave steepness parameter, $M = Ro/\beta^*$, is a measure of the relative importance of the first term (the inertial term) to the third term (the wave phase dispersion). Quasigeostrophic motions may be wavelike or turbulent. More specifically, they may be governed by linear Rossby wave (LRW) theory, nonlinear Rossby wave (NRW) theory or quasigeostrophic turbulence (QGT) theory. The critical parameter for distinguishing these regimes is the Rossby wave steepness parameter. Wavelike (linear) regimes occur where $M<1$ and turbulent (nonlinear) regimes occur where $M>1$. LRW theory is valid where $M<1$, that is, the wave phase dispersion of the β-effect is greater than the inertial effects (wave steepening). NRW theory is valid where $M = 0(1)$, and the phase dispersion balances the wave steepening effects. Rhines (1977) demonstrated that the strong nonlinear interactions involved in QGT occur only when the inertial effects are much stronger than the wave phase dispersion, that is, $M>>1$.

Charney and Flierl (1981) suggested that in the oceans $M = 0(1)$, but that it varies from one oceanic region to another. In this investigation, the Rossby wave steepness parameter has been evaluated and the geographic variability of the character of the quasigeostrophic motions will be discussed. Kang and Magaard (1980) have shown that the linearized wave equations can still be used where $M = 0(1)$ for single plane waves. The LRW and NRW regimes, therefore, cannot be distinguished with the Rossby wave steepness parameter. The following regimes can be identified:

(1) where $M < 0(10)$, LRW and NRW theories are applicable, and
(2) where $M > 0(100)$, QGT theory is applicable.

The intermediate region, where $M = 0(10)$, is a turbulent regime that does not have the strong nonlinear interactions required for QGT, but does have inertial terms large enough to preclude LRW and NRW theories.

The evaluation of the quasigeostrophic scaling parameters is summarized in Table V-1. The horizontal length and velocity scales were obtained from the wavenumber spectra as summarized in Table IV-15. The average median latitude of each geographic region was calculated from the sections. The Coriolis parameter was calculated as $f_o = 2\Omega \sin \Theta$, where $\Omega = 7.29 \times 10^{-5}$ rad/s (i.e. the angular rate of rotation of the earth) and Θ is the average median latitude, and $\beta_o = 2\Omega \cos \Theta/R$, where R = 6371 km (i.e. radius of the earth). The internal Rossby deformation radii, r_i, for the regions in the northern hemisphere were obtained from the results of Emery et al. (1984). Spatial averages of r_i were calculated with the appropriate 5° square values. In the SA and SP, the r_i were determined from the quasi-synoptic sections, assuming a two-layer fluid, by the relation (LeBlond and Mysak, 1978)

$$r_i^2 = \frac{g(\rho_2-\rho_1)\, H_1 H_2}{f_o^2 \rho_2 (H_1 + H_2)} \tag{5.2}$$

where H_1 and ρ_1 are the thickness and density of the upper layer, H_2 and ρ_2 are the same quantities in the lower layer and g is gravity.

The values of Ro, B and β^* in Table V-1 are everywhere consistent with quasigeostrophic theory. The Rossby number does not exceed a value of 8.3×10^{-2}. It is everywhere much less than one, indicating the dominance of the Coriolis forces over the inertial forces required for quasigeostrophy. If the upper bound of the velocity scale, U*, is used, Ro is still much less than one. The Burger number is everywhere on the order of one indicating that the observed baroclinic length scales are on the order of the average regional internal Rossby radii. The values of B in Table V-1 vary from 3.0×10^{-1} to 3.8. The HIGH region and the LOW region both have one length scale that is greater than r_i and one length scale that is smaller. The sphericity parameter is everywhere much less than one. Its value varies from 4.5×10^{-3} to 4.0×10^{-2}. The changes in the Coriolis parameter over the dominant scales of variability are small, and thus the β-plane is a valid approximation.

The values of the Rossby wave steepness parameter calculated from the dominant length and velocity scales (Table IV-15) are listed in Table V-2. M was calculated using the baroclinic velocity scale, U, and is considered to be

Table V-1 Summary of the Rossby number (Ro), the Burger number (B) and the sphericity parameter (β^*) for the geographic regions. The input parameters consist of the length scale ($L=\lambda/2\pi$), the velocity scale (U), the average median latitude, the Coriolis parameter (f_o), the meridional gradient of f_o (β_o) and the internal Rossby radius (r_1).

Region	L (m)	U (m/s)	Average Median Latitude	f_o (rad/s)	β_o (rad/(ms)	r_1 (m)	$R_o=U/(f_oL)$	$B=(r_1/L)^2$	$\beta^*=\beta_oL/f_o$
NWA	4.54×10^4	1.02×10^{-1}	37.3°	8.84×10^{-5}	1.82×10^{-11}	2.49×10^4	2.5×10^{-2}	3.0×10^{-1}	9.3×10^{-3}
	2.47×10^4	1.81×10^{-1}					8.3×10^{-2}	1.0	5.1×10^{-3}
NWP	6.29×10^4	8.9×10^{-2}	33.3°	8.00×10^{-5}	1.91×10^{-11}	3.67×10^4	1.7×10^{-2}	3.4×10^{-1}	1.5×10^{-2}
	3.10×10^4	1.45×10^{-1}					5.8×10^{-2}	1.4	7.4×10^{-3}
	2.31×10^4	1.86×10^{-1}					1.0×10^{-1}	2.5	5.5×10^{-3}
NEA	3.26×10^4	3.8×10^{-2}	41.6°	9.68×10^{-5}	1.71×10^{-11}	2.40×10^4	1.2×10^{-2}	5.4×10^{-1}	5.7×10^{-3}
	2.55×10^4	4.6×10^{-2}					1.9×10^{-2}	8.9×10^{-1}	4.5×10^{-3}
	2.47×10^4	4.8×10^{-2}					2.0×10^{-2}	9.4×10^{-1}	4.4×10^{-3}
SA	8.12×10^4	4.0×10^{-2}	17.8°	4.38×10^{-5}	2.18×10^{-11}	4.90×10^4	1.1×10^{-2}	3.6×10^{-1}	4.0×10^{-2}
	3.90×10^4	5.6×10^{-2}					3.3×10^{-2}	1.6	1.9×10^{-2}
NEP	5.09×10^4	4.6×10^{-2}	33.7°	8.08×10^{-5}	1.90×10^{-11}	5.27×10^4	1.1×10^{-2}	1.1	1.2×10^{-2}
	2.71×10^4	5.5×10^{-2}					2.5×10^{-2}	3.8	6.4×10^{-3}
SP	4.77×10^4	6.3×10^{-2}	27.7°	6.78×10^{-5}	2.03×10^{-11}	3.31×10^4	1.9×10^{-2}	4.8×10^{-1}	1.4×10^{-2}
HIGH	4.77×10^4	9.6×10^{-2}	36.3°	8.63×10^{-5}	1.84×10^{-11}	3.08×10^4	2.3×10^{-2}	4.2×10^{-1}	1.0×10^{-2}
	2.47×10^4	1.75×10^{-1}					8.2×10^{-2}	1.6	5.3×10^{-3}
LOW	4.77×10^4	4.5×10^{-2}	34.3°	8.21×10^{-5}	1.89×10^{-11}	3.97×10^4	1.1×10^{-2}	6.9×10^{-1}	1.1×10^{-2}
	2.71×10^4	5.5×10^{-2}					2.5×10^{-2}	2.1	6.2×10^{-3}

Table V-2 Summary of the Rossby wave steepness parameter and the inferred dynamics from its value, for each geographic region. M and M* were determined from U and U*, respectively. The true Rossby wave steepness parameter of the observed length scales will be between M and M*. The inferred dynamics include: linear Rossby wave (LRW) theory, nonlinear Rossby wave (NRW) theory and quasigeostrophic turbulence (QGT) theory.

Region	λ (km)	M	M*	Inferred Dynamics
NWA	285	2.7	6.1	LRW/NRW
	155	16.3	36.4	QGT
NWP	395	1.1	2.5	LRW/NRW
	195	7.8	17.4	-
	145	18.2	40.7	QGT
NEA	205	2.1	4.7	LRW/NRW
	160	4.2	9.4	-
	115	4.5	10.0	-
SA	510	0.3	0.7	LRW/NRW
	245	1.7	3.8	LRW/NRW
NEP	320	0.9	2.0	LRW/NRW
	170	3.9	8.7	-
SP	300	1.4	3.1	LRW/NRW
HIGH	300	2.3	5.1	LRW/NRW
	155	15.5	34.7	QGT
LOW	300	1.0	2.2	LRW/NRW
	170	4.0	8.9	-

underestimated. M* is calculated using the estimated upper limit of the velocity scale, U*, and is considered to be overestimated. The true Rossby wave steepness parameter for the observed wavelengths will be between M and M*. The dynamics inferred from these values of M and M* are tabulated for each wavelength. In both the high- and low-energy regions, the longer dominant wavelengths (>200 km) are consistent with linear and nonlinear Rossby wave theories. The shorter wavelengths (<200 km) in the low-energy regions, have scales consistent with governing dynamics intermediate between LRW/NRW and QGT theories. In the high-energy regions, the scales of the shorter wavelengths are consistent with quasigeostrophic turbulence theory, with the exception of the 195 km wavelength in the NWP, which has scales consistent with dynamics intermediate between LRW/NRW and QGT theories.

The magnitudes of the Rossby wave steepness parameter, M, from Table V-2 have been illustrated in Figure V-1 as functions of the length (L) and velocity (U) scales. The x-axis is the length scale in kilometers on a logarithmic scale and the y-axis is the velocity scale in cm/s on a logarithmic scale. Isopleths of the steepness parameter are shown for values of 0.1, 1.0, 10 and 100, assuming a latitude of 35°. Due to the relation, $U = M\beta_o L^2$, these isopleths have a slope of two. The magnitude of M, obviously, increases as a logarithmic scale from the bottom right to the top left corner, perpendicular to the isopleths. Each pair of length and velocity scales has been plotted and labelled with the appropriate geographic region. The solid circles indicate length scales that are distinct to the 95% confidence level, the asterisk indicates a length scale distinct to the 80% confidence level and the empty circles represent length scales that could not be defined to the 80% confidence level. Lines have been drawn to join the length scales within the same region. The upper limit of the velocity scales, U*, has not been plotted, to avoid confusion.

This graph provides an illuminating picture of many of the mesoscale eddy properties discussed earlier. The EKEs, of course, are greater for higher velocity scales. Thus, the points with the largest kinetic energies are higher up on the graph. It is clearly seen from the negative slope of the lines of each geographic region that the shortest scales contain the most kinetic energy. An inference may be made about the distribution of the variance of the geopotential anomaly in each geographic region from the slope of the regional lines. The velocity scales were determined from the geostrophic relation and

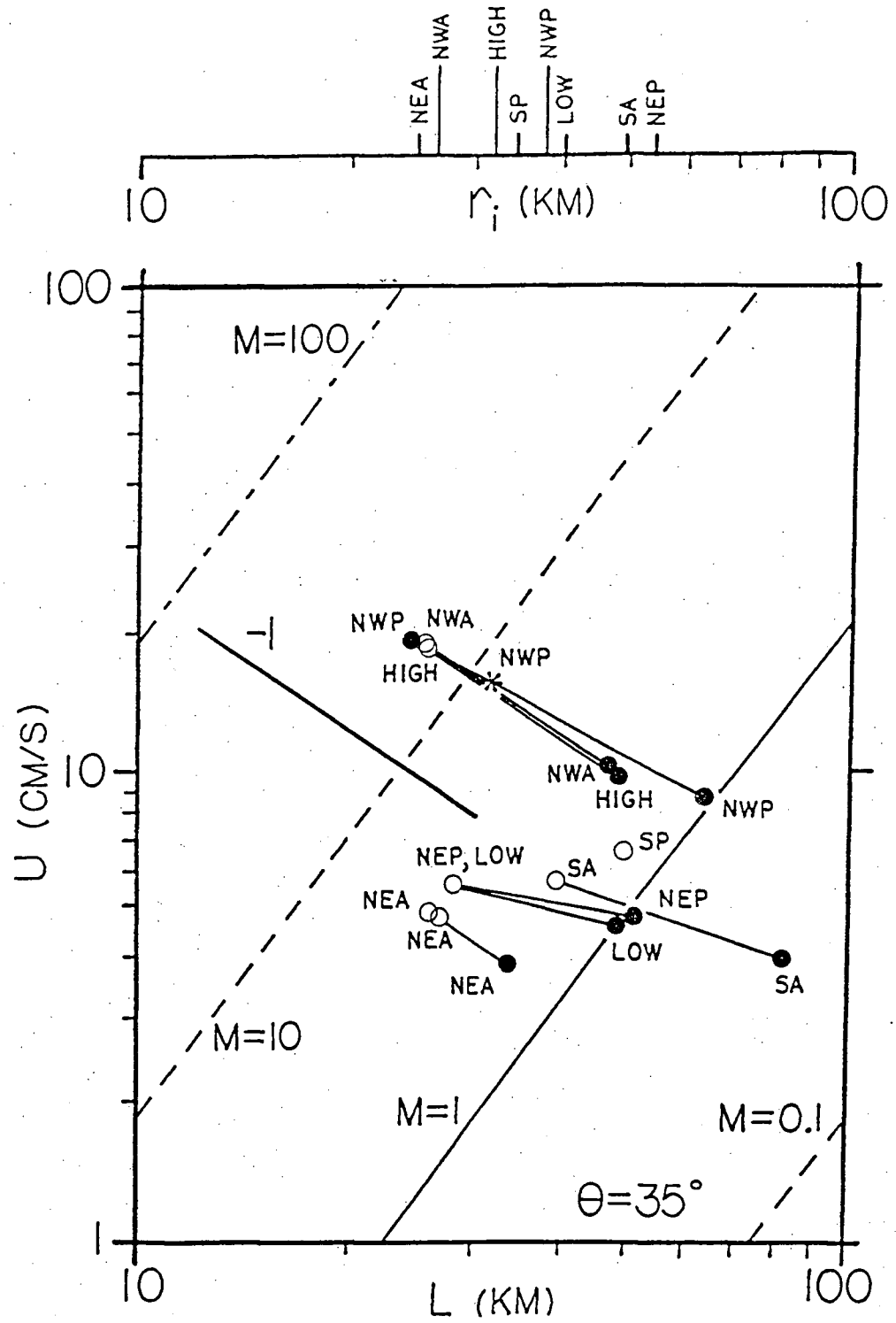

Figure V-1 The dominant length (L) and velocity (U) scales plotted in relation to the isopleths of the Rossby wave steepness parameter (M). M<1 suggests a wavelike (linear) regime and M>1 suggests a more turbulent (nonlinear) regime. The solid circles indicate dominant length scales that are distinct to the 95% confidence level, the asterisk indicates a length scale distinct to the 80% confidence level and the empty circles indicate scales not distinct to the 80% confidence level. The scales within each region are connected by lines. The line with a slope of -1 is the slope of the regional line that would be expected if the variance of D within a region was constant for all wavenumbers.

thus are proportional to $(f_o L)^{-1} S_D$. The Coriolis parameter is assumed to be constant for each region. For a constant variance, (S_D^2), at all wavelengths within a region, the regional line plotted in Figure V-1 would have a -1 slope. All of the regional lines have negative slopes with magnitudes less than one, reflecting the fact that the spectral peaks on the D variance-conserving plots are smaller for the shorter length scales in each region. The regional lines of the high-energy regions have negative slopes with greater magnitudes than the low-energy regions. This illustrates the fact that the differences between the magnitudes of the D spectral peaks in each high-energy region are smaller than the differences in each low-energy region. Thus, for similar wavenumber bandwidths, each high-energy region has D variances at the dominant length scales that are more comparable in magnitude than the D variances of the dominant length scales in each low-energy region. The exception to this generalization is the NEA region which has a regional line with a slope similar to the high-energy regions.

It can also be clearly seen, that the high-energy regions are more nonlinear than the low-energy regions. That is, they have larger values of M. This comparison, however, must be made between corresponding length scales. In order of increasing nonlinearity, the scales may be generally listed as:

1) long wavelengths (>280 km) in the low-energy regions,
2) long wavelengths in the high-energy regions,
3) short wavelengths (<280 km) in the low-energy regions and
4) short wavelengths in the high-energy regions.

B. Linear Rossby Waves

It is of interest to examine the properties of the free linear baroclinic Rossby waves with wavelengths as discerned from the wavenumber spectra. In a manner similar to that of Roden (1977), the corresponding frequencies, group velocities and phase velocities of the dominant length scales in each geographic region were determined. The geographic variability of these properties will be discussed and compared to the results of other investigators.

The dispersion relation for free linear first-mode baroclinic Rossby waves is (LeBlond and Mysak, 1978),

$$\omega = - \beta_o k/(k^2 + l^2 + r_i^{-2}) \tag{5.3}$$

where ω is the frequency, k and l are the zonal and meridional wavenumbers such that the horizontal wavenumber is $k_H = (k^2 + l^2)^{1/2}$ and β_o is the meridional gradient of the Coriolis parameter at a given latitude. The eastward and northward components of the group velocity are,

$$\begin{aligned} C_{gx} &= \beta_o(k^2-l^2-r_i^{-2})/(k^2+l^2+r_i^{-2})^2 \\ C_{gy} &= 2\beta_o kl/(k^2+l^2+r_i^{-2})^2 \end{aligned} \tag{5.4}$$

The eastward and northward components of the phase velocity are,

$$\begin{aligned} C_{px} &= -\beta_o k^2/((k^2+l^2)(k^2+l^2+r_i^{-2})) \\ C_{py} &= -\beta_o kl/((k^2+l^2)(k^2+l^2+r_i^{-2})) \end{aligned} \tag{5.5}$$

For a given latitude the first baroclinic mode will have an upper cut-off frequency of $\omega_c = \beta_o r_i/2$.

The frequencies, group velocities, phase velocities and cut-off frequencies were determined for the dominant wavelengths of the geographic regions at different latitudes. For each wavelength, the properties of the meridional waves ($k = 0$, $l = 2\pi/\lambda$, where λ is the wavelength), the oblique waves ($-k = l$, $k_H = 2\pi/\lambda$) and the zonal waves ($k = -2\pi/\lambda$, $l = 0$) were calculated with the above relations. By convention, $k<0$ to obtain $\omega>0$. Zonal bands with 5° meridional widths were examined in each geographic region. Zonal averages of the internal Rossby deformation radius (r_i) were obtained from Emery et al. (1984).

Investigations into the existence of linear Rossby waves, their propagation characteristics and generation mechanisms have been predominantly in the Northeast Pacific Ocean (Bernstein and White, 1974; Emery and Magaard, 1976; White, 1977; Kang and Magaard, 1980; Price and Magaard, 1980; White and Saur, 1981; White, 1982; Price and Magaard, 1983; Mysak, 1983; White, 1985; Cummins

et. al., 1986). Kang and Magaard (1980) demonstrated, in a region north of Hawaii, that the Rossby waves have negligible energy except at annual frequencies. For the most part, investigators have concentrated on the characteristics of the annual Rossby wave. Kang and Magaard (1980), in the region 30°-40°N, 130°W-160°E, observed annual Rossby waves of random phase. These waves had northwestward phase velocities, 300 km wavelengths, phase speeds of 2 cm/s and RMS particle velocities of 2 to 7 cm/s. This investigation was based on a 40-month XBT data set. Generation mechanisms were only proposed. Mysak (1983) suggested that the intense and localized eastern boundary current fluctuations, west of Vancouver Island, could provide the main source of vorticity of these waves. The theory predicted wavelengths of 300 km, and phase and group speeds on the order of 1 cm/s in the NEP due to this generation mechanism. Cummins et al. (1986) examined the generation of annual Rossby waves in the North Pacific by the wind stress over the whole region. This model predicts similar wavelengths and directional properties as Kang and Magaard (1980) and Mysak (1983), and RMS current speeds of 3 to 6 cm/s.

The wavelengths observed in the quasi-synoptic XBT data set, in the NEP, are 320 and 170 km with velocity perturbation scales of 4.6 and 5.5 cm/s, respectively. The properties of the dispersive baroclinic Rossby waves with the above wavelengths are shown in Table V-3. The 320 km wavelength with its 4.6 cm/s velocity scale is in very good agreement with the observations of Kang and Magaard (1980), the theory of Mysak (1983) and the model of Cummins et al. (1986). The 170 km wavelength, however, has a shorter wavelength and smaller phase velocities than those predicted in the above models. These wavelengths are not comparable to those obtained by White and his co-investigators using nondispersive models. Their predicted wavelengths were generally about 1000 km.

There are no observations or models of LRWs, of the quality of those in the NEP, that may be compared with the observed length and velocity scales in the other geographic regions. Table V-4 summarizes the properties of linear baroclinic Rossby waves obtained from 5.3 to 5.5 for the six geographic regions. It will be assumed that the LRW theory is consistent with the observed scales of motion if all of three criteria are met. First, a near-annual period is required. Kang and Magaard (1980) found that there was negligible energy at other than the annual periods. It is reasonable to expect the annual period to be dominant in the other geographic regions on the basis

BAROCLINIC ROSSBY WAVES - NEP

Wavelength = 320 km

	Latitude										
	7.5	12.5	17.5	22.5	27.5	32.5	37.5	42.5	47.5	52.5	57.5
r_1	139.2	86.6	66.9	53	44.4	36.2	31.2	25.2	20	17.1	-
$\omega_c \times 10^6$	1.58	.97	.73	.56	.45	.35	.28	.21	.15	.12	-
Meridional Waves, k=0											
$\omega \times 10^6$	0	0	0	0	0	0	0	0	0	0	-
$C_g \times 10^2$	5.19	4.31	3.58	2.85	2.27	1.68	1.29	.86	.54	.37	-
direction	270	270	270	270	270	270	270	270	270	270	-
Oblique Waves, k=1											
$\omega \times 10^6$	.72	.6	.5	.4	.32	.23	.18	.12	.07	.05	-
T	.3	.3	.4	.5	.6	.9	1.1	1.7	2.7	3.9	-
$C_p \times 10^2$	3.67	3.04	2.53	2.02	1.61	1.19	.91	.61	.38	.26	-
direction	315	315	315	315	315	315	315	315	315	315	-
$C_g \times 10^2$	4.62	3.39	2.62	2.02	1.62	1.25	1	.71	.47	.33	-
direction	188	199	210	223	233	243	249	256	261	264	-
Zonal Waves, l=0											
$\omega \times 10^6$	1.02	.85	.7	.56	.45	.33	.25	.17	.11	.07	-
T	.2	.2	.3	.4	.4	.6	.8	1.2	1.9	2.8	-
$C_p \times 10^2$	5.19	4.31	3.58	2.85	2.27	1.68	1.29	.86	.54	.37	-
direction	270	270	270	270	270	270	270	270	270	270	-
$C_g \times 10^2$	3.96	2.09	.95	.11	.31	.55	.58	.52	.39	.29	-
direction	90	90	90	90	270	270	270	270	270	270	-

Wavelength = 170 km

	Latitude										
	7.5	12.5	17.5	22.5	27.5	32.5	37.5	42.5	47.5	52.5	57.5
r_1	139.2	86.6	66.9	53	44.4	36.2	31.2	25.2	20	17.1	-
$\omega_c \times 10^6$	1.58	.97	.73	.56	.45	.35	.28	.21	.15	.12	-
Meridional Waves, k=0											
$\omega \times 10^6$	0	0	0	0	0	0	0	0	0	0	-
$C_g \times 10^2$	1.6	1.49	1.37	1.23	1.08	.91	.76	.57	.4	.29	-
direction	270	270	270	270	270	270	270	270	270	270	-
Oblique Waves, k=1											
$\omega \times 10^6$	.42	.39	.36	.32	.28	.24	.2	.15	.1	.08	-
T	.5	.5	.6	.6	.7	.8	1	1.3	1.9	2.6	-
$C_p \times 10^2$	1.13	1.05	.97	.86	.76	.64	.54	.41	.28	.21	-
direction	315	315	315	315	315	315	315	315	315	315	-
$C_g \times 10^2$	1.54	1.36	1.2	1.01	.84	.67	.54	.41	.29	.22	-
direction	182	186	189	195	200	209	217	229	241	248	-
Zonal Waves, l=0											
$\omega \times 10^6$	.59	.55	.51	.45	.4	.34	.28	.21	.15	.11	-
T	.3	.4	.4	.4	.5	.6	.7	.9	1.3	1.9	-
$C_p \times 10^2$	1.6	1.49	1.37	1.23	1.08	.91	.76	.57	.4	.29	-
direction	270	270	270	270	270	270	270	270	270	270	-
$C_g \times 10^2$	1.48	1.23	.99	.72	.5	.26	.11	.04	.12	.12	-
direction	90	90	90	90	90	90	90	270	270	270	-

Table V-3 **Frequencies (ω, 1/s), periods (T, yr), phase velocities (C_p, m/s), and group velocities (C_g, m/s) of the free baroclinic Rossby waves of the observed quasi-synoptic length scales at the appropriate latitudes in the NEP. The directions are in degrees clockwise from north. The internal Rossby radius (r_1, km) and the upper cut-off frequency (ω_c, 1/s) of the first-mode baroclinic Rossby wave is also given for each latitude.**

Table V-4 Summary of the properties of the linear first-mode baroclinic Rossby waves. λ is the wavelength. U is the baroclinic velocity scale obtained from the data set. U* is the estimated upper limit of the true velocity perturbations obtained using Wyrtki et al.'s (1976) EKEs. C_p is the phase speed. The only dynamics which may be inferred from these properties is the linear Rossby wave (LRW) theory.

Region	λ (km)	Period (yr)	C_p (cm/s)	U/C_p	U^*/C_p	Inferred Dynamics
NWA	285	0.5 - 6.4	0.14 - 1.97	9.7	21.7	-
	155	0.5 - 4.0	0.12 - 0.93	34.5	77.1	-
NWP	395	0.5 - 1.8	0.70 - 2.77	5.1	11.4	-
	195	0.5 - 1.3	0.48 - 1.34	15.9	35.6	-
	145	0.5 - 1.3	0.36 - 0.86	30.5	68.2	-
NEA	205	0.5 - 13.0	0.05 - 1.28	5.7	12.7	-
	160	0.5 - 10.5	0.05 - 0.93	9.4	21.0	-
	115	0.7 - 8.1	0.04 - 0.56	16.0	35.8	-
SA	510	0.3 - 1.0	1.64 - 5.68	1.1	2.5	LRW
	245	0.3 - 0.7	1.06 - 2.48	3.2	7.2	LRW
NEP	320	0.2 - 3.9	0.26 - 5.19	1.7	3.8	LRW
	170	0.3 - 2.6	0.21 - 1.60	6.1	13.6	-
SP	300	0.3 - 2.8	0.34 - 3.28	3.5	7.9	-

of their results. Also, the proposed generation mechanisms of the LRW field in the NEP, for the most part, have annual periods. Similar mechanisms are likely to be vorticity sources for the LRW field in the other regions, and thus create a resonance at the annual period. Second, it is required that the phase speed of the LRWs be on the order of one. This will be consistent with the investigations in the NEP. Third, it is required that the velocity perturbations, U and U*, not be much greater than the phase speeds. Where this occurs, the inertial effects will be more important than the wave phase dispersion. Kang and Magaard (1980), as previously discussed, demonstrated that the particle velocities may be on the order of the phase speed for single plane waves and the nonlinear terms will cancel. Thus, the terms, U/C_p and U^*/C_p, may be used as analogs to the Rossby wave steepness parameter. It is required that either of these terms be on the order of one for LRW theory to be valid.

An examination of the LRW properties, in Table V-4, shows that the observed length scales have, for the most part, near-annual periods and phase speeds on the order of one. Only a few wavelengths, however, have U/C_p or U^*/C_p on the order of, or less than, one. The regions which can be said to have length and velocity scales consistent with LRW theory (according to the above criteria) are the SA and the NEP. That is, LRW theory is consistent with the observed length and velocity scales only for wavelengths longer than 200 km in the low-energy regions.

C. Nonlinear Geophysical Turbulence

A number of models of nonlinear turbulence exist that use dimensionality to determine the theoretical decay coefficients of the temperature and velocity spectra in an inertial wavenumber range. That is, the theory predicts a spectral shape of the form k^{-p} in the wavenumber ranges between the sources and sinks of energy, where k is the wavenumber and p is the power-law exponent. The consistency of the temperature spectra, of the quasi-synoptic XBT data set, with the existing models of nonlinear turbulence will be examined using the slopes of the spectra between the longest dominant wavelengths and the Nyquist wavenumbers. Since the D and geostrophic velocity spectra are dependent on the temperature spectra, they will provide no new information for this analysis.

Ozmidov (1965) depicted the energy distribution over the full wavenumber spectrum of motions (i.e. wavelengths of 10,000 km to 1 cm) in the ocean in accordance with the 5/3 "Kolmogorov Spectrum Law". The basic features of this idealized model are the influx of external energy over localized wavenumber bands, separated by inertial subranges of cascading energy from low to high wavenumbers. Wyrtki (1967) examined the spectrum of ocean turbulence between 40 and 1000 km wavelengths using the MBT data from the sixteen "Townsend Cromwell" cruises of 1964-66. The results were consistent with Ozmidov's model, with a peak in the spectrum near 200 km likely representative of an energy influx from large eddies. This three-dimensional isotropic model, developed by Kolmogorov, predicts power-law exponents of 5/3 for both the temperature and velocity spectra in the inertial subranges. Temperature is assumed to be a passive tracer.

Several other models of turbulence have been developed, although none are sufficiently realistic to be directly applicable to the observed mesoscale variability. In the geophysical context, it may be expected that any theory will be applicable only to a certain range of scales. The Kolmogorov-type turbulence has only been verified for small-scale processes. At somewhat larger scales, the stratification must exercise an important role and Phillips' (1966) theory may be appropriate. Phillips' theory predicts a Kolmogorov-type turbulence at wavenumbers higher than a critical buoyancy wavenumber where the turbulence is three-dimensional. At lower wavenumbers, the turbulence is anisotropic when comparing the horizontal scales to the vertical scale, due to the stratification. The power-law exponents are three and one for the velocity and temperature spectra, respectively. At scales where the earth's rotation is a dominant factor, Kraichnan (1967) and Charney (1971) proposed two-dimensional and three-dimensional models of quasigeostophic turbulence, respectively. Kraichnan postulated two inertial subranges for the two-dimensional turbulence. Energy is injected at a given wavenumber and is transferred uniformly to lower wavenumbers, while enstrophy (i.e. mean-squared vorticity) is transferred uniformly to higher wavenumbers. The transfers of energy, in the second range, and enstrophy in the first range, are zero. By similarity arguments, the velocity and temperature spectra have power-law exponents of 5/3 in the energy-cascade range, while in the enstrophy cascade range the velocity and temperature spectra have power-laws of three and one, respectively. Charney developed a three-dimensional model that accounts for the baroclinic nature of the atmosphere (and ocean) with the conservation of a pseudo-potential

vorticity. This is a combination of the conservation of potential vorticity and potential temperature. This theory predicts a k^{-3} law at wavenumbers higher than the excitation wavenumber for both the horizontal velocity and temperature spectra. Temperature is a passive tracer in both of these theories.

Examples of the log-log representations of the spectra in Chapter IV are shown in Figure V-2, with the temperature spectra shown for the HIGH and LOW regions. The power-law exponents where determined in the wavenumber range from the peaks of the log-log spectra to the regional Nyquist wavenumbers. For spectra with dominant wavelengths at scales smaller than the peak wavenumber, this wavenumber range cannot be considered a true inertial subrange, however, the slopes obtained may still be of use. The slopes were determined with a least-squares linear regression of the average smoothed spectral estimates (Zar, 1974). The 95% confidence intervals of the slopes were calculated using the upper and lower 95% confidence limits of the spectral estimates.

The spectral power-law exponents of the temperatures are summarized in Table V-5. The high- and low-energy regions have power-law exponents that are generally between two and three. The exponents of the SA and the SP regions have large error bars as a result of the short wavenumber range (due to the low Nyquist wavenumbers) used in the regression and must be considered next to useless. For the most part, the power-law exponents of each variable are not significantly different between regions.

The power-law exponents of the HIGH and LOW regions provide a greater contrast than the individual geographic regions. The temperature variance associated with the baroclinic eddy field in the HIGH region has a characteristic power-law exponent of 3.01 with 95% confidence limits of 2.85 to 3.17 (i.e. about 3.0) between wavelengths of 300 to 54 km. In the LOW region, the temperature variance has a characteristic power-law exponent of 2.47 with 95% confidence limits of 2.29 and 2.65 (i.e. about 2.5) between wavelengths of 300 to 91 km. The characteristic power-law exponent of the LOW region is significantly less than that of the HIGH region.

These results show that, in the HIGH region, the temperature spectrum is proportional to the -3.0 power. This is consistent with Charney's (1971) three-dimensional geophysical turbulence model. This implies that the energy

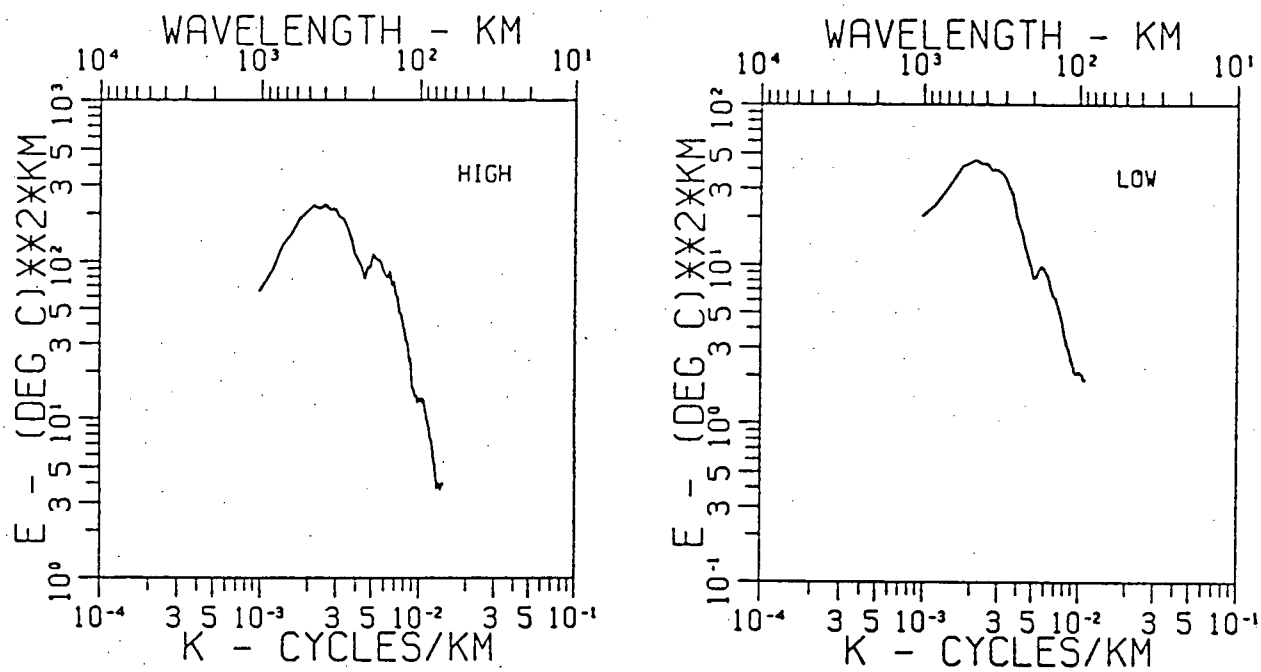

Figure V-2 **Sample plots of the log-log spectral representations. These spectra depict the mid-thermocline temperature variability in the HIGH and LOW regions.**

Table V-5 Summary of the spectral power-law exponents of the mid-thermocline temperature. The slopes of the log-log spectra (-p) were obtained over the wavelength bands as shown. The relation $E(k) = k^{-p}$ describes the slopes of the spectra in the applicable wavenumber range where E is the temperature spectrum, k is the wavenumber and p is the power-law exponent.

Region	p	95% Confidence Interval	Wavelength Band (km)
NWA	**2.85**	2.62 - 3.08	285 - 70
NWP	**3.07**	2.84 - 3.30	395 - 54
NEA	**2.61**	2.16 - 3.06	205 - 91
SA	**2.70**	1.10 - 4.33	510 - 210
NEP	**2.40**	2.19 - 2.61	320 - 88
SP	**2.37**	-2.50 - 7.24	300 - 220
HIGH	**3.01**	2.85 - 3.17	300 - 54
LOW	**2.47**	2.29 - 2.65	300 - 91

of the mesoscale perturbations is input into the high-energy regions at wavelengths of about 300 km, cascades to slightly lower wavenumbers and propagates away as linear/nonlinear Rossby waves. Enstrophy, however, cascades to higher wavenumbers over a wavelength band of 300 to 54 km with no energy transfer. The enthusiasm with which one accepts these results and their physical interpretation must be tempered by the fact that Charney's model assumes that temperature is a passive tracer, and this is clearly not the case for oceanic mesoscale motions. In the LOW region, the temperature spectrum has a slope of -2.5. This is not consistent with any of the models of nonlinear geophysical turbulence. The low-energy region of the NEA has a power-law exponent of three, similar to that of the high-energy regions, however, the regional Rossby wave steepness parameter (Table V-2) is not large enough to permit quasigeostrophic turbulence.

A distinct geographic variability of the consistency of the nonlinear geophysical turbulence models has been identified. Charney's three-dimensional model of quasigeostrophic turbulence is consistent with the spectral slopes of the temperature spectra in the high-energy regions (i.e. the western boundary current regions), but not in the low-energy regions (i.e. the ocean interior and eastern boundary current regions). There are no existing models of geophysical turbulence that are consistent with the reported power-law exponents between 2.0 and 3.0 in the low-energy regions. The spectra do not provide evidence for a -5/3 power-law characteristic of the three-dimensional Kolmogorov-type turbulence. Neither do they suggest that Kraichnan's model of two-dimensional quasigeostrophic turbulence is appropriate.

D. Summary of the Inferred Dynamics

The dynamics inferred from the Rossby wave steepness parameter, the LRW theory and the geophysical turbulence models are summarized in Table V-6. The results are identical to those inferred from the Rossby wave steepness parameter (Table V-2). The linear Rossby wave analysis provided more confidence in the applicability of LRW theory to wavelengths less than 200 km in the low-energy regions, while the analysis of the spectral power-laws provided additional evidence for the validity of QGT theory in the high-energy regions. The latter, also, identified the specific geophysical turbulence model that is consistent with the spectral slopes of the temperature in the

Table V-6 Summary of the inferred dynamics of the dominant wavelengths (λ). The inferred dynamics are: linear Rossby wave (LRW) theory, nonlinear Rossby wave (NRW) theory and quasigeostropic turbulence (QGT) theory. The bold wavelengths are distinct to the 95% confidence level, the underlined wavelength is distinct to the 80% confidence level and the other wavelengths are not distinct to the 80% confidence level.

Region	λ (km)	Inferred Dynamics
NWA	**285**	**LRW/NRW**
	155	QGT
NWP	**395**	**LRW/NRW**
	195	-
	145	**QGT**
NEA	**205**	**LRW/NRW**
	160	-
	115	-
SA	**510**	**LRW/NRW**
	245	LRW/NRW
NEP	**320**	**LRW/NRW**
	170	-
SP	300	LRW/NRW
HIGH	**300**	**LRW/NRW**
	155	QGT
LOW	**300**	**LRW/NRW**
	170	-

high-energy regions - Charney's (1971) three-dimensional quasigeostrophic turbulence model.

The dominant wavelengths of the baroclinic eddy field that are distinct to the 95% confidence level and their respective inferred dynamics, in Table V-6, are in bold script. These are the most significant results. These dominant wavelengths are all greater than 200 km and are consistent with LRW and NRW theories. The one exception to this statement is the 145 km wavelength in the NWP, which is consistent with QGT theory. The HIGH and LOW regions have dominant wavelengths of 300 km that are consistent with the dynamics of LRWs and NRWs. The HIGH energy region is, of course, more nonlinear, but one must examine the shorter and lesser significant wavelengths in order to find the strong nonlinear interactions required for QGT.

VI. CONCLUSIONS

The geographic variability of the mesoscale statistics and the inferred dynamics has been examined with a quasi-synoptic expendable bathythermograph (XBT) data set. Over 10,000 XBT profiles were obtained from the Canadian Armed Forces, the United States Navy and the National Oceanographic Data Center in 95 single-ship trans-oceanic sections and 29 multiship/AXBT surveys. Mean temperature-salinity and salinity-depth curves were used to infer the geopotential anomaly from the temperature profiles for use in the statistical and dynamical analyses.

The descriptive analyses qualitatively discussed the geographic variability of the observed quasi-synoptic temperature structure. Geographic regions with different horizontal length scales and amplitudes of eddy variability were defined with the aid of previous work using climatological data sets. Six geographic regions were delineated and classified as high- or low-energy areas. The high-energy regions are the Northwest Atlantic (NWA) and the Northwest Pacific (NWP). The low-energy regions are the Northeast Atlantic (NEA), the South Atlantic (SA), the Northeast Pacific (NEP) and the South Pacific (SP). Two composite regions were also defined. The HIGH region comprised the high-energy regions, and the LOW region comprised the low-energy regions. Typical temperature sections from each geographic region were examined and compared to observations of the mesoscale variability from other sources. This investigation found the quasi-synoptic data set to exhibit mesoscale properties very similar to those reported in the literature, and thus the data set was confidently accepted as being representative of the eddy variability in the regions under examination.

Several statistical analyses were used to quantify the quasi-synoptic mesoscale structure in the upper 400 m of the ocean. The mid-thermocline temperature and the geopotential anomaly (0-4000 kPa) were used to represent the mesoscale variability. Perturbation variables were obtained by removing the low-wavenumber signal from the sections with a 1000 km running mean, and from the surveys with zonal and meridional linear trends.

The geographic variability of the standard deviations, skewness, kurtosis and intermittencies of the temperature and the geopotential anaomaly for the

sections and the surveys were discussed. The statistics of the sections and the surveys are comparable. The HIGH region has geopotential anomaly perturbations with average amplitudes of 0.67 m^2/s^2, and the LOW region has average amplitudes of 0.26 m^2/s^2. The ratio of these amplitudes is 2.58. The positive skewness of the LOW region suggests that the baroclinic eddy field consists of predominantly warm eddies. The skewness of the HIGH region is not significantly different from zero. The intermittencies are the same and indicate that the mesoscale perturbations occur over about 45% of the two regions. The standard deviation of the temperature is 1.40°C in the HIGH region and 0.54°C in the LOW region. The positive skewness of temperature in the LOW region is consistent with the field of warm eddies suggested above. The negative skewness of the temperature in the HIGH region suggests that the baroclinic eddy field consists predominantly of cold eddies, as opposed to the field of warm eddies in the LOW region.

The North Pacific Subtropical Front (NPSF) and the North Pacific Equatorial Current (NPEC) are subregions of the NEP. The standard deviations of these two regions are higher than the corresponding statistics of the NEP, since the sampling subregions are in relatively high eddy activity areas of the NEP. The NPEC has the largest mid-thermocline temperature and geopotential anomaly perturbations. The positive skewness of the baroclinic eddy field in the NPSF is consistent with the NEP statistics. The NPEC has a negative skewness. This is not consistent with the NEP, however, it is consistent with the field of cold eddies discussed in the descriptive analysis of the four surveys of the area.

The seasonal variability of the NEP region and the isotropy of the mesoscale eddy field were investigated in some detail. The standard deviations, skewness, kurtosis and intermittencies were calculated for quarterly subsets of sections. Significant seasonal signals were apparent. There may be a seasonal variability in the mesoscale eddy fields similar to that discussed by Gould (1983) in the NEA, and the regions that are unevenly sampled over the seasons (i.e. all but the NEP and LOW regions) may have seasonal biases. Quantifying the seasonal variability is beyond the ability of this data set. The assumption of horizontal isotropy was evaluated with an anisotropy factor determined from the surveys. The anisotropy factor, A_S, was determined by the relation, $A_S = L_M/L_Z$. L_M and L_Z are the meridional and zonal decorrelation scales, respectively, obtained from the

meridionally and zonally averaged autocorrelation functions of the surveys. The regional anisotropy factors are not significantly different from one. With no evidence to the contrary, the assumption of isotropy was considered reasonable for the spatial scales of motion being examined.

Wavenumber spectra were used to examine the distribution of variance in wavenumber space between wavelengths of 1000 to 100 km. The dominant wavelengths of the mid-thermocline temperature and geopotential anomaly spectra are between 100 and 400 km. There is no significant scale separation between the dominant length scales of the high- and low-energy regions. In the HIGH region, the geopotential anomaly spectrum has peak wavelengths of 300 and 155 km, with the respective wavenumber bands containing 60 and 30% of the variance. The LOW region has spectral peaks at 300 and 170 km containing 73 and 15% of the variance, respectively. The low-energy regions have a greater portion of their total variance in the longer wavelengths.

The two-dimensional isotropic eddy kinetic energies (EKEs) were estimated for each geographic region and wavenumber band. The eddy kinetic energies per unit mass for the HIGH and LOW regions are 250 and 36 cm^2/s^2, respectively. The HIGH region has about seven times the baroclinic eddy kinetic energy of the LOW region in wavelengths between 1000 and 100 km. These EKEs are similar to those reported by Fu (1983) with SEASAT altimetry data, but are less than those of Wyrtki et al. (1976) by a factor of five. This is consistent with the understanding that: the baroclinic (0-400 m) EKEs of the quasi-synoptic XBT data set are underestimates, since they will miss a significant portion of the barotropic signal; that the EKEs of the SEASAT altimetry (Fu, 1983) are underestimates, since they will miss a significant portion of the mesoscale signal due to the 24-day sampling window; and that the EKEs of the ship drift data (Wyrtki et al., 1976) are overestimates due to the winds acting on the vessels.

The relevance of quasigeostrophic dynamics was inferred using several dynamical tests with the wavenumber statistics. The quasigeostrophic scaling parameters (i.e. the Rossby number (Ro), the Burger number (B) and the sphericity parameter (β^*)) were evaluated using the dominant length and velocity scales of each geographic region. For all regions and length scales, it was found that $R_o << 1$, $B = 0(1)$ and $\beta^* << 1$, consistent with the quasigeostrophic scaling. The Rossby wave steepness parameter,

$M = U/(\beta_o L^2)$, was calculated to investigate whether the baroclinic eddy fields are wavelike (linear) or turbulent (nonlinear). The frequencies, phase velocities and group velocities were calculated using free linear dispersive baroclinic Rossby wave theory and the observed wavelengths. These results were compared with the extensive work, by other investigators, in the NEP. The consistency of the temperature spectra with the existing models of geophysical turbulence was examined with the slopes of the near-inertial spectral subranges.

The results of these dynamical tests imply a geographic variability of the dynamics governing the observed baroclinic eddy fields. For all the geographic regions, the wavelengths greater than 200 km are consistent with linear Rossby wave theory or nonlinear Rossby wave theory. The applicability of these two theories cannot be distinguished with these simple dynamical tests. The motions in the high-energy regions are, of course, more nonlinear than the motions in the low-energy regions with corresponding scales. In the high-energy regions, the perturbations with wavelengths less than 200 km are consistent with quasigeostrophic turbulence theory, in particular, Charney's (1971) model of three-dimensional quasigeostrophic turbulence. The motions with wavelengths less than 200 km in the low-energy regions have scales that are intermediate between those expected of linear/nonlinear Rossby wave theories, and quasigeostrophic turbulence theories.

This investigation has examined the geographic variability of the properties of the mesoscale motions in the ocean with a quasi-synoptic XBT data set. An inhomogeneity of the mesoscale statistics is demonstrated that is comparable to the results of previous investigators. The wavenumber statistics of the quasi-synoptic data provided estimates of the dominant length and velocity scales. From these scales of motion, an inhomogeneity in the governing dynamics of the mesoscale perturbations in the ocean has been inferred. The strength of the quasi-synoptic data lies in the ability to determine the length and velocity scales of variability from which simple dynamical models may be discussed.

Recommendations For Future Work

The results of this work have emphasized the value of quasi-synoptic data sets for resolving the length and velocity scales in the ocean. The data set

employed here is by no means the complete collection of the quasi-synoptic data that may be used for the examination of the mesoscale variability. There is a potential to examine the characteristics of the mesoscale in a similar manner, but in more detail, in several regions of the ocean with available data sets (most notably the Northwest Atlantic and the Northeast Pacific). This investigation highlights the requirement for further work in four areas. First, the seasonal signal of the synoptic mesoscale variability must be examined. The possibility of significant seasonal signals of the mesoscale variability was identified in this study, but could not be quantified. Two, the horizontal anisotropy of these scales of motions has not been adequately resolved. Investigators have identified individual features in most regions of the ocean with anisotropic characteristics, but there is no statistically significant evidence that mesoscale motions are, on average, anisotropic over large regions of the ocean. Three, the detrending scheme used here to remove the low-wavenumber signal of the large-scale mean flow cannot be considered ideal. It would be much preferable to use a time series of quasi-synoptic sections along a repeated transect. In this manner the mean flow may be removed by averaging. Fourth, it would be valuable to obtain the wavenumber spectra of the measured velocities in conjunction with the measured temperatures. At this date, however, there are no quasi-synoptic velocity and temperature data sets available for examining the mesoscale. The instruments required are very new and expensive. An acoustic doppler current profiler (ADCP) with XBTs, or expendable current profilers (XCPs) would be capable of obtaining the required data sets.

REFERENCES

Anderson, E.R., 1979. Expendable Bathythermograph (XBT) Accuracy Studies. Naval Ocean Systems Center, San Diego, p. 143.

Andrews, J.C. and P. Scully-Powers, 1976. The Structure of an East Australian Current Anticyclonic Eddy. J. Phys. Oceanogr., Vol. 6(9), 756-765.

Bennett, A.F., 1983. The South Pacific Including the East Australian Current. In Eddies in Marine Science, Robinson, A.R. (ed.), Springer-Verlag, New York, 219-244.

Bernstein, R.L., 1983. Eddy Structures of the North Pacific Ocean. In Eddies in Marine Science, Robinson, A.R. (ed.), Springer-Verlag, New York, 158-166.

Bernstein, R.L. and W.B. White, 1974. Time and Length Scales of Baroclinic Eddies in the Central North Pacific. J. Phys. Oceanogr., Vol. 4(10), 613-624.

Bernstein, R.L. and W.B. White, 1977. Zonal Variability in the Distribution of Eddy Energy in the Mid-Latitude North Pacific Ocean. J. Phys. Oceanogr., Vol. 7(1), 123-126.

Bernstein, R.L. and W.B. White, 1981. Stationary and Travelling Mesoscale Perturbations in the Kuroshio Extension Current. J. Phys. Oceanogr., Vol. 11(5), 692-703.

Bernstein, R.L. and W.B. White, 1982. Meridional Eddy Heat Flux in the Kuroshio Extension Current. J. Phys. Oceanogr., Vol. 12(1), 154-159.

Brooks, L.E.P. and N. Carruthers, 1953. Handbook of Statistical Methods in Meteorology. Her Majesty's Stationary Office, London, p. 412.

Charney, J.G., 1971. Geostrophic Turbulence. J. Atmos. Sc., Vol. 28, 1087-1095.

Charney, J.G. and G. R. Flierl, 1981. Oceanic Analogues of Large Scale Atmospheric Motions. In Evolution of Physical Oceanography, Warren, B.A. and C. Wunsch (eds.), MIT Press, Cambridge, Mass., 504-549.

Cheney, R.E., 1977. Synoptic Observations of the Oceanic Frontal System East of Japan. J. Geophys. Res., Vol. 82(34), 5459-5468.

Cheney, R.E., J.G. Marsh and B.D. Beckley, 1983. Global Mesoscale Variability from Repeat Tracks of Seasat Alimeter Data. J. Geophys. Res., 4343-4359.

Cummins, P.F., L. A. Mysak and K. Hamilton, 1986. Generation of Annual Rossby Waves in the North Pacific by the Wind Stress Curl. J. Phys. Oceanogr. (In press).

Dantzler, H.L., 1976. Geographical Variations in Intensity of the North Atlantic and the North Pacific Oceanic Eddy Fields. Deep-Sea Res., Vol. 23, 783-794.

Defant, A., 1981. The Troposphere. English trans ed. by W.J. Emery, Amerind Publishing Co., New Delhi, p. 113.

Denham, R.N., R. W. Bannister, K.M. Guthrie, D.G. Browning and F.G. Crook, 1981. Some Hydrological Features of the South Fiji Basin. New Zealand Marine and Freshwater Res., Vol. 15, 299-306.

Department of the Navy, 1978. Guide to Common Shipboard Expendable Bathythermograph (XBT) Recording Malfunctions, NSTL Station, St. Louis, p. 46.

Dickson, R.R., W.J. Gould, P. A. Gurbutt and P.D. Killworth, 1982. A Seasonal Signal in Ocean Currents to Abyssal Depths. Nature, Vol. 295, 193-198.

Douglas, B.C. and R.W. Agreen, 1983. The Sea State Correction for GOES-3 and SEASAT Satellite Altimetry Data. J. Geophys. Res., Vol. 86(10), 931-10937.

Ebbesmeyer, C. Curtis and B.A. Taft, 1979. Variability of Potential Energy, Dynamic Height, and Salinity in the Main Pycnocline of the Western North Atlantic, J. Phys. Oceanogr., Vol. 9(11), 1073-1089.

Emery, W.J., 1983a. On the Geographical Variability of the Upper Level Mean and Eddy Fields in the North Atlantic and North Pacific, J. Phys. Oceanogr., Vol. 13(2), 269-291.

Emery, W.J., 1983b. Global Summary: Review of Eddy Phenomena as Expressed in Temperature Measurements. In Eddies in Marine Science, Robinson, A.R. (ed.), Springer-Verlag, Berlin, 354-375.

Emery, W.J. and L. Magaard, 1976. Baroclinic Rossby Waves as Inferred from Temperature Fluctuations in the Eastern Pacific, J. Mar. Res., Vol. 34(3), 365-385.

Emery, W.J. C.C. Ebbesmeyer and J.P. Dugan, 1980. The Fraction of the Vertical Isotherm Deflections Associated with Eddies: An Estimate from Multiship XBT Surveys. J. Phys. Oceanogr., Vol. 10(6), 885-899.

Emery, W.J. and Dewar, J.S., 1982. Mean Temperature-Salinity, Salinity-Depth and Temperature-Depth Curves of the North Atlantic and the North Pacific. Prog. in Oceanography, Vol. 11, 219-305.

Emery, W.J., W.G. Lee and L. Magaard, 1984. Geographic and Seasonal Distributions of Density, Brunt-Vaisala Frequency and Rossby Radii in the North Atlantic and North Pacific. J. Phys. Oceanogr., Vol. 14(2), 294-317.

Fofonoff, N.P., 1981. The Gulf Stream System. In Evolution of Physical Oceanography, Warner, B.A. and C. Wunsch (eds.), MIT Press, Cambridge, Mass., 112-139.

Fu, L.-L., 1983. On the Wavenumber Spectrum of Oceanic Mesoscale Variability Observed by Seasat Altimetry. J. Geophys. Res., 4331-4341.

Gill, A.E., 1982. Atmosphere-Ocean Dynamics. Academic Press, New York, p. 662.

Gould, W.J., 1983. The Northeast Atlantic Ocean. In Eddies in Marine Science, Robinson, A.R. (ed.), Springer-Verlag, New York, 145-157.

Harrison, W.J. Emery, J.P. Dugan and Bo-Cheng Li, 1983. Mid-Latitude Mesoscale Temperature Variability in Six Multiship XBT Surveys. J. Phys. Oceanogr., Vol. 13(4), 648-662.

Hinze, J., 1975. Turbulence, 2nd Edition. McGraw-Hill, New York, p. 790.

Holloday, C.G. and J.J. O'Brien, 1975. Mesoscale Variability of Sea Surface Temperature. J. Phys. Oceanogr., Vol. 5(6), 864-870.

Howe, M.R. and R.J. Tait, 1967. A Subsurface Cold-Core Cyclonic Eddy. Deep Sea Res., Vol. 14, 373-378.

Hoyoshi, Y., 1981. Space-Time Cross Spectral Analysis Using the Maximum Entrophy Method. J. Met. Soc. Japan, Vol. 59(5), 620-624.

Jenkins, G.W. and D.G. Watts, 1968. Spectral Analysis and its Applications. Holden-Day, New York, p. 460.

Joyce, T.M., W. Zenk and J.M. Toole, 1981. Anatomy of a Cyclonic Ring in the Drake Passage. Deep-Sea Res., Vol. 28A(11), 1265-1287.

Kanasewich, E.R., 1981. Time Sequence Analysis in Geophysics. University of Alberta, Edmonton, p. 480.

Kang, Y.Q. and L. Magaard, 1980. Annual Baroclinic Rossby Waves in the Central North Pacific. J. Phys. Oceanogr., Vol. 10(9), 1159-1167.

Kitano, K., 1975. Some Properties of the Warm Eddies Generated in the Confluence Zone of the Kuroshio and Oyashio Currents. J. Phys. Oceanogr., Vol. 5, 245-252.

Koshlyakov, M.N. and Y.M. Grachev, 1973. Mesoscale Currents at a Hydrophysical Polygon in the Tropical Atlantic. Deep-Sea Res., Vol. 20, 507-521.

Kraichnan, R.H., 1967. Inertial Ranges in Two-dimensional Turbulence, Phy. of Flds., Vol. 12(7), 1427-1433.

Lai, D.Y. and P.L. Richardson, 1977. Distribution and Movement of Gulf Stream Rings. J. Phys. Oceanogr., Vol. 7(9), 670-683.

LeBlond, P.H. and L.A. Mysak, 1978. Waves in the Ocean. Elsevier North-Holland, New York, p. 602.

Leetma, A., 1977. A Study of MODE Dynamics. Deep-Sea Res., Vol. 24, 733-742.

Legeckis, R., 1977. Long Waves in the Eastern Equatorial Pacific Ocean: A View from a Geostationary Satellite. Science, 1179-1181.

Lutjeharms, J.R., 1981. Spatial Scales and Intensities of Circulation in the Ocean Areas Adjacent to South Africa. Deep-Sea Res., Vol. 28A, 1289-1302.

Lutjeharms, J.R. and D.J. Baker, 1980. A Statistical Analysis of the Mesoscale Dynamics of the Southern Ocean. Deep-Sea Res., Vol. 27A, 145-159.

Malanotte Rizzoli, P., 1982. Planetary Solitary Waves and their Existing Solutions in the Context of a Unified Approach. In Topics in Ocean Physics, Osborne, A.R., P. Malanotte P. Rizzoli (eds.), North-Holland Publishing, New York, 126-147.

Millero, F.J. and A. Poisson, 1981. International One-atmosphere Equation of State for Sea-water. Deep-Sea Res., Vol. 28A, 625-629.

Miyaki, M., 1981. AXBT Observations. In Fronts 80: Preliminary Results, Paulson, C.A. and P.P. Niiler (eds.), School of Oceanography, Oregon State University, Ref. 81-2, 11-19.

MODE Group, 1975. Dynamics and the Analysis of MODE-I. MIT Press, p. 250.

MODE Group, 1978. The Mid-Ocean Dynamics Experiment. Deep-Sea Res., Vol. 25, 859-910.

Moore, C., 1981. UBC Curve. Computing Centre, University of British Columbia, Vancouver, B.C., p. 164.

Mysak, L.A., 1983. Generation of Annual Rossby Waves in the North Pacific. J. Phys. Oceanogr., Vol. 13(10), 1908-1923.

Mysak, L.A., 1986. El Nino, Interannual Varability and Fisheries in the Northeast Pacific Ocean. Can. J. Fish. and Aquatic Res., Vol. 43(2), 464-487.

National Oceanographic Data Center, 1984. NODC Users Guide, National Oceanographer Data Center, Monteray, p. 503.

Nishida, H. and W.B. White, 1982. Horizontal Eddy Fluxes of Momentum and Kinetic Energy in the Near-Surface of the Kuroshio Extension. J.Phys. Oceanogr., Vol. 12(1), 160-170.

Ozmidov, R.V., 1965. Energy Distribution Between Oceanic Motions of Different Scales. Izv. Atm. and Ocean Physcis Series, Vol. 1(4), 439-448.

Parker, G.E., 1971. Gulf Stream Rings in the Sargasso Sea. Deep-Sea Res., Vol. 18, 981-993.

Patzert, W.C., 1969. Eddies in Hawaiian Waters. HIG-G9-8, University of Hawaii, p 50.

Patzert, W.C. and R.L. Bernstein, 1976. Eddy Structure in the Central South Pacific Ocean. J. Phys. Oceanogr., Vol. 6, 392-394.

Pedlosky, J., 1979. Geophysical Fluid Dynamics. Springer-Verlag, New York, p. 624.

Phillips, O.M., 1966. Dynamics of the Upper Ocean. Cambridge University Press, London, p. 261.

Pickard, G.L. and W.J. Emery, 1982. Descriptive Physical Oceanography, 4th Edition. Pergamon Press, Toronto, p. 249.

Pond, S. and G.L. Pickard, 1983. Introductory Dynamical Oceanography, 2nd Edition. Pergamon Press, Toronto, p. 329.

Price, J.M. and L. Magaard, 1983. Rossby Wave Analysis of Subsurface Temperature Fluctuations along the Honolulu-San Franciscan Great Circle. J. Phys. Oceanogr., Vol. 13(1), 258-268.

Rasmusson, E.M., P.A. Arkin, A.F. Krueger, R.S. Quiroz and R.W. Reynolds, 1981. The Equatorial Pacific Atmospheric Climate during 1982-83. Tropical Ocean-Atmosphere Newsletter, No. 21, 2-3.

Rhines, P.B., 1977. The Dynamics of Unsteady Currents. In The Sea, Goldberg, E.D., I.N. McCave, J.J. O'Brien, J.H. Steele (eds)., John Wiley, New York, 189-318.

Richman, J.G., C. Wunsch, and N.G. Hogg, 1977. Space and Time Scales of Mescoscale Motion in the Western North Atlantic. Reviews of Geophysics and Space Physics, Vol. C15(4), 385-419.

Richardson, P.C., 1979. Gulf Stream Rings. J. Phys. Oceanogr., Vol. 10(1), 90-101.

Richardson, P.L., 1983. Gulf Stream Rings. In Eddies in Marine Science, Robinson, A.R. (ed.), Springer-Verlag, New York, 19-45.

Robinson, A.R., 1982. Dynamics of Ocean Currents and Circulation: Results of POLYMODE and Related Investigations. In Topics of Ocean Physics, Osborne, A.R. and P. Malanotti Rizzoli (eds.), North-Holland Publishing, Amsterdam, 3-29.

Robinson, A.R. (ed.), 1983. Eddies in Marine Science. Springer-Verlag, New York, p. 609.

Roden, G.I. 1977. On Long-Wave Disturbances of Dynamic Height in the North Pacific. J. Phys. Oceanogr., Vol. 7(1), 41-49.

Roden, G.I., 1979. The Depth Variability of Meridional Gradients of Temperature, Salinity and Sound Velocity in the Western North Pacific. J. Phys. Oceanogr., Vol. 9(4), 756-767.

Roden, G.J., 1980. Mesothermohaline, Sound Velocity and Baroclinic Flow Structure of the Pacific Subtropical Front during the Winter of 1980. J. Phys. Oceanogr., Vol. 9, 756-767.

Royer, T.C., 1978. Ocean Eddies Generated by Seamounts in the North Pacific. Science, Vol. 199, 1063-1064.

Saunders, P.M., 1971. Anticyclonic Eddies formed from Shoreward Meanders of the Gulf Stream. Deep-Sea Res., Vol. 18, 1207-1219.

Saunders, P.M., 1972a. Comments on Wavenumber Frequency Spectra of Temperature in the Free Atmosphere. J. Atmos. Sci., Vol. 29, 197-199.

Saunders, P.M., 1972b. Space and Time Variability of Temperature in the Upper Ocean. Deep-Sea Res., Vol. 19, 467-480.

Saunders, P.M., 1982. Circulation in the Eastern North Atlantic. J. Mar. Res., Vol. 40 (suppl).

Schmitz, W.J., 1981. Observations of Eddies in the Newfoundland Basin. Deep-Sea Res., Vol. 28A(11), 1417-1421.

Selby, S.M. (ed.), 1965. Standard Mathematical Tables. The Chemical Rubber Co., Ohio, p. 407.

Sippican, 1970. Ocean Engineering Bulletin No. 1, XBT System Linearity Equations. The Sippican Corp., Mass., p. 12.

Sippican, 1975. XBT System Manual. The Sippican Corp., Mass., p. 207.

Stommel, H., 1960. The Gulf Stream. Cambridge University Press, London, p. 202.

Stommel, H., E.D. Stroup, J.L. Reid and B.A. Warren, 1973. Transpacific Hydrographic Sections at Lats. 43°S and 28°S: The Scorpio Expedition - I Preface. Deep Sea Res., Vol. 20, 1-8.

Stroup, E.D., B.J. Kilansky and K. Wyrtki, 1981. AXBT Observations during the Hawaii/Tahiti Shuttle Experiments. HIG-81-1, University of Hawaii, p. 98.

Swaters, G., 1985. On Several Aspects of Modom Theory. Ph.D. Thesis, Department of Oceanography, University of British Columbia, Vancouver, B.C., p. 147.

Tabata, S., 1975. The General Circulation of the Pacific Ocean and a Brief Account of the Oceanographic Structure of the North Pacific Ocean, Part I. Atmosphere, Vol. 13(4), 133-168.

Tennekes, H. and J.L. Lumley, 1972. A First Course in Turbulence. MIT Press, Cambridge, Mass., p. 300.

Thomson, K.A., W.J. Emery and D.P. Krauel, 1984a. A Samoa-Hawaii XBT section in November 1982. Tropical Ocean-atmosphere Newsletter, No. 27, 14-15.

Thomson, K.A., D.P. Krauel and W.J. Emery, 1984b. Synoptic SXBT Observations from Canadian Armed Forces Destroyer Squadrons, February 1980 to June 1983. Report for the Defence Research Establishment-Pacific, p. 146.

Turner, J.S., 1981. Small-Scale Mixing Processes. In Evolution of Physical Oceanography, Warren, B.A. and Wunsch, C. (eds.), MIT Press, Cambridge, Mass., 236 - 263.

Van Woert, M., 1982. The Subtropical Front: Satellite Observations During FRONTS 80. J. Geophys. Res., Vol. 87C(12), 9523-9536.

Voorhis, A.D., 1976. The Influence of Deep Mesoscale Eddies on Sea Surface Temperature in the North Atlantic Subtropical Convergence. J. Phys. Oceanogr., Vol. 6(11), 953-961.

Walpole, R.E. 1974. Introduction to Statistics. MacMillan Publishing Co., New York, p. 340.

White, W.B. 1977. Annual Forcing of Baroclinic Long Waves in the Tropical North Pacific Ocean. J. Phys. Oceanogr., Vol. 7(1), 50-61.

White, W.B., 1982. Travelling Wave-like Mesoscale Perturbations in the North Pacific Current. J. Phys. Oceanogr., Vol. 12(3), 231-245.

White, W.B., 1985. The Resonant Response of Interannual Baroclinic Rossby Waves to Wind Forcing in the Eastern Mid-latitude North Pacific. J. Phys. Oceanogr., Vol. 15, 403-415.

White, W.B. and A.E. Walker, 1974. Time and Depth Scales of Anomalous Subsurface Temperature at Ocean Weather Stations P, N, and V in the North Pacific. J. Geophys. Res., Vol. 79(30), 4517-4522.

White, W.B. and L. Bernstein, 1979. Design of an Oceanographic Network in the Mid-latitude North Pacific. J. Phys. Oceanogr., Vol. 9, 592-606.

White, W.B. and J.F.T. Saur, 1981. A Source of Annual Baroclinic Waves in the Eastern Subtropical North Pacific. J. Phys. Oceanogr. Vol. 11(11), 1452-1462.

Wilson, W.S. and J.P. Dugan, 1978. Mesoscale Thermal Variability in the Vicinity of the Kuroshio Extension. J. Phys. Oceanogr., Vol. 8(5), 537-540.

Wunsch, C., 1981. Low Frequency Variability of the Sea. In Evolution of Physcial Oceanography, Warren, B.A. and C. Wunsch, (eds.), MIT Press, Cambridge, Mass., 341-375.

Wyrtki, K. 1967. The Spectrum of Ocean Turbulence over Distances Between 40 and 1000 Kilometres. Deutsche Hydrographische Zeitschrift, Vol. 20(4), 176-186.

Wyrtki, K. 1975. Fluctuations of the Dynamic Topography in the Pacific. J. Phys. Oceanogr., Vol. 5(7), 450-459.

Wyrkti, K., 1982. Eddies in the Pacific North Equatorial Current. J. Phys. Oceanogr. Vol. 12(2), 746-749.

Wyrtki, K., L. Magaard and J. Hager, 1976. Eddy Energy in the Oceans. J. Geophys. Res., Vol. 81, 2641-2646.

Wyrtki, K., E. Firing, D. Halpern, R. Knox, G.J. McNally, W.C. Patzert and E.D. Stroup, 1981. The Hawaii to Tahiti Shuttle Experiment. Science, 211, 22-28.

Zar, J.H., 1974. Biostatistical Analysis. Prentice-Hall Inc., Toronto, p. 620.